

***EX VIVO* EVALUATION OF INTERVERTEBRAL DISC MECHANICS USING  
DIFFUSION WEIGHTED IMAGING ON THE 7 T MR: EFFECT OF DEGENERATION**

by

Kelsey McGivern

B.Eng., McGill University, 2015

A THESIS SUBMITTED IN PARTIAL FULFILLMENT OF  
THE REQUIREMENTS FOR THE DEGREE OF

MASTER OF APPLIED SCIENCE

in

THE FACULTY OF GRADUATE AND POSTDOCTORAL STUDIES  
(Biomedical Engineering)

THE UNIVERSITY OF BRITISH COLUMBIA  
(Vancouver)

May 2019

© Kelsey McGivern, 2019

The following individuals certify that they have read, and recommend to the Faculty of Graduate and Postdoctoral Studies for acceptance, a thesis/dissertation entitled:

***Ex vivo* evaluation of intervertebral disc mechanics using diffusion-weighted imaging on the 7 T MR: effect of degeneration**

---

submitted by Kelsey McGivern in partial fulfillment of the requirements for

the degree of Master of Applied Science

in Biomedical Engineering

**Examining Committee:**

Dr. Peter Crompton

Co-supervisor

Dr. David Wilson

Co-supervisor

Dr. Tom Oxland

Supervisory Committee Member

Dr. Cornelia Laule

Additional Examiner

## **Abstract**

Structural changes that occur with intervertebral disc (IVD) degeneration have been established. However, there has been a major challenge in differentiating changes that occur solely due to aging from those that might be considered pathological; uncertainty still exists regarding the exact anatomic and physiologic basis for several clinical symptoms. Diffusion-weighted imaging techniques in MRI have emerged as a potential method to further our understanding of the effects of degeneration on the mechanical behaviour of the intervertebral disc.

This thesis describes three stages of work: first, a force measurement system was developed to measure forces acting on the intervertebral disc in the MRI environment using Fibre Bragg Grating sensors. Secondly, a loading rig was designed that applied loading conditions simulating postures of the spine (supine, standing, flexion, and extension) to lumbar cadaveric specimens, and an imaging protocol was developed to obtain ADC measurements within defined regions of the disc. ADC values were then compared in these regions between loading conditions. In the final stage, a device was designed to apply compressive strain to annulus fibrosus tissue samples. In this part of the study, the relationship between ADC values and both compressive strain and degenerative state were evaluated.

We successfully developed a load measurement system, which was then used to record forces acting on the disc during diffusion imaging. We found ADC values to be significantly higher in the NP than the AF; no change in ADC values was observed between different regions of the AF, regardless of applied load. Further, we found no change in ADC between any of the four loading conditions within any region of the disc.

In samples of AF tissue, we found no change to ADC with increasing compressive strain, regardless of degenerative level. A significant decrease in ADC values was found between severely degenerated discs and both mild and moderately degenerated discs.

These results expand our understanding of the limitations of ADC measurements to detect changes to mechanical behaviour of the disc, and may help guide the direction of future studies towards other avenues of investigation of disc mechanics.

## **Lay Summary**

Lower back pain is an increasingly common problem, especially in the aging population. It is the most common reason for missed work which, in conjunction with treatment and care costs, carries an extreme economic burden. A major cause of lower back pain is degeneration of the tissue that sits between the vertebrae that make up the spine, called the intervertebral disc. Current methods for diagnosing disc degeneration typically use MRI. These methods have accurately identified visual changes to the disc caused by degeneration, but are not able to distinguish changes that occur naturally with aging from those that cause pain. The purpose of this thesis is to investigate a new MRI imaging technique to study changes to the mechanical behaviour of the spine caused by degeneration, which has the potential to help bridge that gap between our current diagnostic methods of low back pain and clinical symptoms.

## **Preface**

The thesis represents my own work for the study design, data analysis, and manuscript writing under the guidance of Dr. David Wilson and Dr. Peter Crompton. On the Bruker Biospec 70/30 7.0 Tesla MRI scanner, Andrew Yung was responsible for the development and implementation of the imaging sequence with my input and feedback, and Andrew Bauman assisted in image acquisition for all subsequent testing.

The experimental methods in the second chapter of this thesis were developed with guidance and input from Dr. Chris Dennison, and Dr. Peter Wild, Dr. Vahid Ahsani, and Riccardo Bostock at the University of Victoria.

The degeneration assessment of all cadaveric specimens was conducted by Shun Yamamoto, an orthopaedic surgeon at ICORD.

The experimental methods conducted in third and fourth chapters of this thesis obtained approval from the University of British Columbia's Clinical Research Ethics Board (certificate #H17-00765).

## Table of Contents

<b>Abstract.....</b>	<b>iii</b>
<b>Lay Summary .....</b>	<b>v</b>
<b>Preface.....</b>	<b>vi</b>
<b>Table of Contents .....</b>	<b>vii</b>
<b>List of Tables .....</b>	<b>x</b>
<b>List of Figures.....</b>	<b>xi</b>
<b>List of Abbreviations .....</b>	<b>xiii</b>
<b>Acknowledgements .....</b>	<b>xiv</b>
<b>Chapter 1: Introduction .....</b>	<b>1</b>
1.1    Motivation.....	1
1.2    Relevant anatomy.....	2
1.3    Mechanics of the intervertebral disc .....	5
1.4    Effect of degeneration on mechanical behaviour.....	8
1.5    Clinical motivation.....	10
1.5.1    Current assessment methods for disc degeneration .....	10
1.5.2    Conservative treatment methods for discogenic pain .....	13
1.6    MR imaging of the intervertebral disc .....	14
1.6.1    Principles of MRI and diffusion-weighted imaging .....	15
1.6.2    Diffusion-weighted imaging of the intervertebral disc in the literature .....	20
1.7    Summary and objectives .....	22
<b>Chapter 2: Design and validation of an MRI-compatible load measurement system .....</b>	<b>25</b>

2.1	Motivation.....	25
2.2	Review of current MRI-compatible load measurement systems .....	26
2.3	Principles of Fibre Bragg Grating sensors .....	28
2.4	Design requirements .....	30
2.5	Final design.....	31
2.6	Validation.....	33
2.6.1	Calibration method.....	33
2.6.2	Results.....	36
2.7	Discussion .....	39
2.8	Limitations and conclusion .....	42
 <b>Chapter 3: Analysis of the apparent diffusion coefficient in the intact human lumbar</b>		
<b>intervertebral discs under simulated physiological loading conditions .....</b>		<b>45</b>
3.1	Design and development of the joint loading rig.....	46
3.2	Image acquisition .....	51
3.3	Test protocol .....	55
3.4	Image processing .....	60
3.5	Results.....	65
3.6	Discussion .....	68
 <b>Chapter 4: Analysis of the apparent diffusion coefficient under compressive strain in the</b>		
<b>annulus fibrosus .....</b>		<b>73</b>
4.1	Loading device design .....	74
4.2	Test protocol .....	77
4.3	Results.....	83



4.4	Discussion .....	87
<b>Chapter 5: Integrated discussion.....</b>		<b>92</b>
5.1	Overview .....	92
5.2	Strengths and contributions.....	93
5.3	Limitations .....	97
5.4	Future work and recommendations.....	100
5.5	Conclusion .....	101
<b>Bibliography .....</b>		<b>103</b>
<b>Appendices.....</b>		<b>111</b>
Appendix A Load measurement system specification.....		111
Appendix B Nucleus-Annulus Boundary MATLAB script.....		121
Appendix C Loading Rig Specification .....		125
Appendix D Stress-relaxation plots for loading of the functional spinal units in simulated relevant postures .....		139
Appendix E Additional and alternative data plots for loading simulating relevant postures .		143
E.1	Degree of rotation for postural loading.....	143
E.2	Alternative data representation for ADC measurements of postural loading .....	143
Appendix F Tissue loading device specification .....		147
F.1	Main apparatus specification .....	147
F.2	Allen key specification .....	150
Appendix G Repeatability Data for ADC .....		151

## List of Tables

Table 1.1 Distribution of water, aggrecan, and collagen in the healthy intervertebral disc .....	4
Table 2.1 Bill of Materials for load measurement system .....	33
Table 2.2 Calibrated FBG names and where they were used for this study .....	35
Table 2.3 Force sensitivity and R-squared values for the FBG sensors .....	38
Table 3.1 Summary of MR parameters for the diffusion-weighted scan protocol .....	53
Table 3.2 Specimen and donor information.....	56
Table 3.3 The defined anatomic regions and their corresponding labels and descriptions .....	63
Table 3.4 Bending moments approximated from peak force data .....	67
Table 3.5 ADC values in different anatomic regions of the disc.....	67
Table 3.6 Significance values between different postural loading conditions in the segmented regions of the disc. ....	68
Table 4.1 Diffusion weighted imaging sequence parameters .....	78
Table 4.2 Specimen and donor information.....	79
Table 4.3 Coefficient of Variance for the different levels of degeneration and loading state .....	85

## List of Figures

Figure 1.1 Relevant anatomy of the lumbar intervertebral disc.....	4
Figure 1.2 Effect of compressive force on the NP and AF tissue.....	6
Figure 1.3 Typical diffusion-weighted pulse sequence .....	17
Figure 1.4 (A) typical T2-weighted scan and (B) same image slice collected using a DWI sequence.....	17
Figure 2.1 Schematic of FBG sensor .....	30
Figure 2.2 Schematic showing placement of FBG sensor mounted to inner wall of hollow acrylic tubing within the loading rig.....	32
Figure 2.3 Schematic (left) and actual (right) setup during calibration testing. ....	34
Figure 2.4 The Bragg Wavelength of FBG-1 as a function of applied force.....	36
Figure 2.5 The Bragg Wavelength of FBG-2 as a function of applied force.....	37
Figure 2.6 The Bragg Wavelength of FBG-3 as a function of applied force.....	37
Figure 2.7 The Bragg Wavelength of FBG-4 as a function of applied force.....	38
Figure 2.8 Plot of residuals as a function of predicted value for FBG-1 .....	39
Figure 3.1 Rendering in SolidWorks of the joint loading rig with major components labeled ....	50
Figure 3.2 Demonstration of the differential screws generating three different loading conditions: a) Standing (axial compression) b) flexion and c) extension.....	51
Figure 3.3 The Bruker Biospec 70/30 7.0 Tesla MRI scanner .....	52
Figure 3.4 Slice orientation relative to the vertebral bodies for the axial diffusion-weighted scan .....	55
Figure 3.5 Top view (left) and sagittal view (right) of lumbar FSU with caudal side potted.....	57
Figure 3.6 Test setup in the MR scan room .....	59

Figure 3.7 Relevant parameters for bending moment approximation .....	60
Figure 3.8 Demonstration of line drawn through disc centre (top) and corresponding signal intensity profile, highlighting transition regions (bottom).....	61
Figure 3.9 MATLAB generated boundary points (left) and corresponding transformed fiducial markers in 3D slicer (right) defining boundary between nucleus and annulus.....	62
Figure 3.10 Segmentation in Slicer of specimen H1338 showing the defined anatomic regions	64
Figure 3.11 Stress relaxation plot for specimen H1144 during flexion loading .....	66
Figure 3.12 Stress relaxation plot for specimen H1338 during flexion loading .....	66
Figure 4.1 Rendering of the tissue mounting assembly .....	75
Figure 4.2 Rendering of loading device: Isometric view (left) and side view (right) labeling dimensions required for centering of the device within the isocentre of the MRI bore .....	76
Figure 4.3 Rendering of the custom Allen key used with the loading apparatus .....	77
Figure 4.4 Drawing of regions harvested for annulus fibrosus tissue samples (left) and photo of tissue sample harvested from the anterior-lateral side of the disc (right) .....	80
Figure 4.5 Segmentation of annulus tissue sample in 3D Slicer.....	82
Figure 4.6 ADC values in unloaded and loaded states across different degenerative grades.....	84
Figure 4.7 Change in average ADC as a function of compressive strain for annulus fibrosus tissue samples.....	85
Figure 4.8 COV of the ADC value in the annulus fibrosus tissue as a function of compressive strain.....	86
Figure 4.9 Mean ADC measurements for different levels of degeneration .....	87
Figure 4.10 Bending moment resulting in extension of the spine (top) and resultant strain profile through the disc (bottom).....	88

## List of Abbreviations

3D	Three-dimensional
ADC	Apparent diffusion coefficient
AF	Annulus fibrosus
DOF	Degrees of freedom
DWI	Diffusion weighted imaging
FOV	Field of view
FSU	Functional spinal unit
FWHM	Full width half maximum
GAG	Glycosaminoglycan
IVD	Intervertebral Disc
LBP	Low back pain
LR	Likelihood ratio
MRI	Magnetic resonance imaging
NP	Nucleus pulposus
RF	Radiofrequency
TE	Echo time
TR	Repetition time
T1	Spin lattice relaxation time
T1rho	“Spin lock” relaxation time
T2	Spin-spin relaxation time

## **Acknowledgements**

My sincere thanks to my supervisors, Dr. David Wilson and Dr. Peter Crompton, for your support and guidance throughout my studies. Your mentorship has been invaluable and has provided me with opportunities that I am incredibly grateful for.

Thank you to the Andrews, both Yung and Bauman, for all of your help with diffusion sequences and scan protocols. This project wouldn't have happened without your expertise and hard work.

Thank you to members of CHHM and the OIBG lab for creating a wonderful work environment that was equal parts enjoyable and educational.

Thank you to Dr. Chris Dennison, Dr. Peter Wild, Dr. Vahid Ahsani and Riccardo Bostock from IESVic for showing me the magic of FBGs and how to utilize them.

Thank you Shun Yamamoto, for giving me your time and expertise for all the specimen degeneration assessments.

Thank you to my family and friends for your endless support, and for listening to me complain about my troubles and helping me through them.

Thank you to Will for the encouragement, the distractions, the advice, and the comfort, and for knowing when which was necessary.

Finally, thank you to Franklin (and Neville), for being a constant source of hugs and happiness.

# Chapter 1: Introduction

## 1.1 Motivation

Degeneration of the intervertebral disc is a prevalent problem, especially for the aging population. Using medical imaging techniques, degenerative discs are found in 10% of people aged 20-29. This increases with age to 96% in those over 60 years old [1], [2]. Common clinical symptoms of disc degeneration include chronic lower back pain, weakness and numbness in the legs, and exacerbated pain with bending movements, all of which can be profoundly debilitating [1], [3]. Lower back pain is one of the most common reasons for missed work, and up to \$120 billion dollars is spent annually to treat back pain in the US alone [4], [5].

Morphologic and anatomic changes that are associated with disc degeneration are well understood. What is still unclear is the relationship between degenerative changes seen on medical images and clinical symptoms [6]–[8]. Existing methods for assessing disc degeneration correlate weakly to clinical findings, especially in early stages of degeneration [9]. Currently, there is little evidence to show that the use of MR imaging in conservative management of LBP is beneficial, yet it is currently the staple diagnostic method for degenerative disorders of the spine [10]–[12]. There is a need to understand the effect of degeneration on the mechanical behaviour of the disc, which may be a better indicator of clinical symptoms than simply anatomic changes.

T2-weighted imaging in MRI is used extensively for grading degeneration of the intervertebral disc (IVD) for both clinical and research purposes. The Pfirrmann grading scheme is one of the most widely-used tools for assessing disc degeneration on T2-weighted scans, and relies on morphologic changes to the disc to qualitatively describe the degenerative process on a scale of I-V [13]. Generally, the Pfirrmann grade can effectively describe anatomic variations

and morphologic changes. However, Pfirrmann grade is unable to distinguish painful discs from asymptomatic ones [6], [7], [14]. Diffusion imaging, an MR technique that highlights diffusion properties of biological tissues, has strong potential for assessing the mechanics of the IVD and disruption of these mechanics due to pathology. This potential is demonstrated in a recent study that showed that MR diffusion measurements are sensitive to different loading conditions [15], a property not evident on a conventional T2-weighted MRI scan. However, the loading conditions in this previous study only considered two neutral postures of the spine: supine and standing. It is still unknown how bending moments caused by flexion and extension affect MR diffusion measurements in both healthy and degenerated discs.

The goal of this study was to investigate the feasibility of using MR diffusion measurements to non-invasively investigate the mechanics of the intervertebral disc and how those mechanics are altered as a result of degeneration, with the aim to bridge the gap between our current understanding of disc degeneration assessed on MRI scans and clinical symptoms.

## **1.2 Relevant anatomy**

The intervertebral disc is a heterogeneous structure, made up of the nucleus pulposus (NP) and the annulus fibrosus (AF), and lies between adjacent vertebrae of the spine (Figure 1.1). Between the disc and the vertebral bodies are endplates, comprised of a thickened layer of cancellous bone and a thin layer of cartilage. The lumbar intervertebral discs are the largest discs in the spine, typically 7 to 10 mm in height and 4 cm in diameter [16] [17].

The nucleus pulposus is the central portion of the disc and is comprised of collagen fibres (type II) arranged randomly [18] and elastin fibres arranged radially [19] that are all contained



within a highly hydrated gel. This disc plays an important role in absorbing and transferring loads through the spine, which is largely attributed to the NP and its high water content [20].

The structure of the AF is different than that of the NP, mainly comprised of layers of concentric rings called lamellae (Figure 1.1). Between the lamellar layers are elastin fibres, which help to bind the lamellae together. It has also been postulated that these elastin fibres help to restore the disc to a neutral position after bending movements such as flexion and extension [21]. Moving radially outwards from the inner AF, the cells of the outer region of the annulus become more fibroblast-like, shifting from oval cell shapes to elongated, thin ones and lie parallel to the network of collagen fibres.

The third morphologically distinct region of the IVD is the cartilaginous endplate. It is a thin layer, typically less than 1 mm in height, and lies parallel to the surface of the IVD. It is made up of collagen fibres that run parallel to the vertebral bodies, with some fibres continuing into the disc [19]. The endplate is a semi-permeable barrier that interfaces with both the disc and the vertebral body and regulates the transport of nutrients into and out of the IVD [20]. The disc is the largest avascular structure in the body, and so nutrient transport through the endplates to the disc centre as well as removal of metabolic waste is crucial for maintaining adequate health and function of the disc. In the adult lumbar IVD, cells at the centre of the NP are up to 8 mm away from the nearest blood vessel [22].

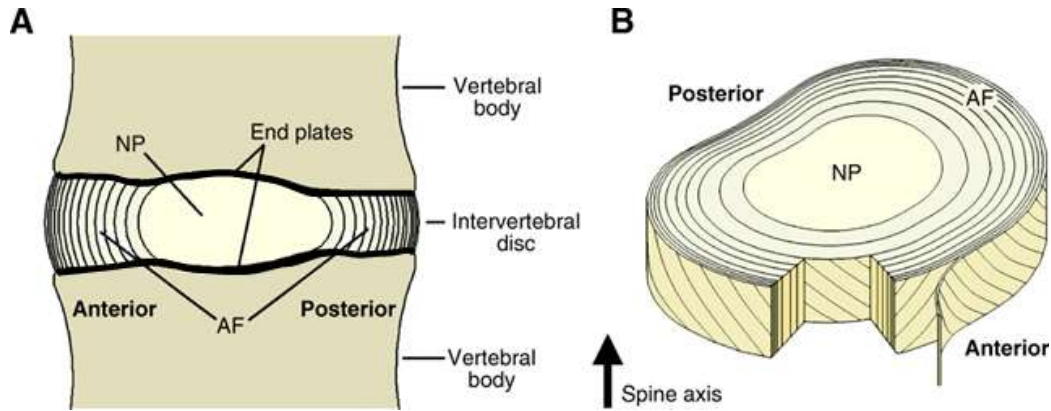


**Figure 1.1 Relevant anatomy of the lumbar intervertebral disc**

*a) sagittal cross-section showing the anatomic regions of the disc and b) isometric view highlighting the structure of the lamellar layers of the annulus fibrosus. © Modified from [23], with permission*

The collagen fibre network of the disc is mainly comprised of type I fibres in the AF and type II fibres in the NP [24]. These networks provide the tensile strength of the IVD and assist in anchoring the disc tissue to the bone. Aggrecan, the major proteoglycan of the disc, helps to maintain tissue hydration [25]. The concentration of aggrecan is much higher in the NP than in the AF and the endplates (Table 1.1).

**Table 1.1 Distribution of water, aggrecan, and collagen in the healthy intervertebral disc**

Region	% Water	% Aggrecan	% Collagen
Annulus Fibrosus	70	5	15
Nucleus Pulposus	77	14	4
Cartilage Endplate	55	8	25

The IVD does have some nerves, however, they are restricted to the outer lamellae [26]. While vascular and neural networks exist in the cartilaginous endplate in young adults, it becomes avascular and aneural in the healthy adult. Blood vessels remain present in longitudinal ligaments adjacent to the vertebral body and IVD and are the main blood source for the disc tissue.

### **1.3 Mechanics of the intervertebral disc**

The intervertebral disc comprises the main joints of the spinal column and make up one-third of the height of the spinal column [27]. Their role is mainly mechanical and the overall behaviour of the disc is reflected in the material and functional properties of the three main regions – nucleus pulposus, annulus fibrosus, and cartilaginous endplate. The manner in which they interact is integral to the mechanical function of the disc; together, they act as a joint with three rotational and three translational degrees of freedom.

Since the NP comprises 40-50 % of the volume in the intervertebral disc [28], it plays a significant role in the load-bearing capabilities of the spinal column. Under compressive load, a hydrostatic pressure is generated in the NP due to its high water content, which increases in magnitude as the force on the disc increases. Previous measurements of the disc pressure as a result of applied load fall within the range of 1 MPa per 1000 N of applied force [29]–[31]. As pressure in the NP increases, stress is transferred from the NP to the AF, generating tension in the surrounding AF tissue [32]. Pressure in the NP is supported on the superior and inferior sides by the endplates and radially by tensile stresses in the AF tissue (Figure 1.2). The reported pressure ranges within the NP during postural loading are 500-900 kPa standing, and 460-1330 kPa seated [33]. The maximum recorded pressure in disc reported by Wilke et al. was 1.80 MPa in a subject standing flexed forwards while holding a 20 kg weight [34].

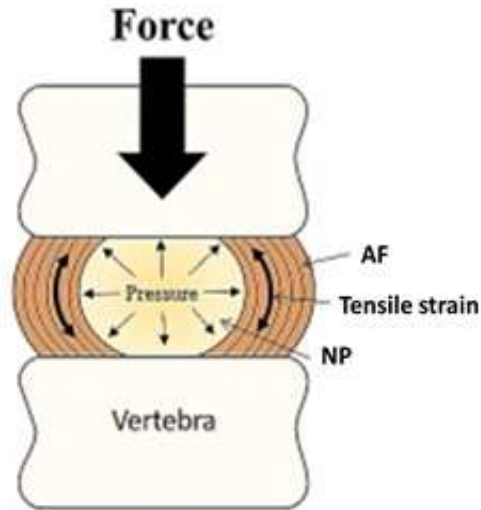


**Figure 1.2 Effect of compressive force on the NP and AF tissue**

*An applied compressive force from muscle contraction and general bodyweight causes the pressure in the NP to increase. Resultantly, tension in the annulus fibrosus tissue (curved arrows) increases as well. Modified from [35], with permission*

Due to compressive load transferred through the cartilaginous endplates and tensile stress transferred from the NP, the AF tissue experiences a combination of tensile and compressive strains resulting from loading conditions associated with different postures. Large tensile strains have been measured around the circumference of the outer AF (hoop stress) as a result of bulging of the disc (Figure 1.2) [36], while the radial expansion of the NP as a result of compressive force has been found to result in compressive strain of the inner AF [37]. An important characteristic of the annulus fibrosus is its nonlinearity under axial tension; the toe region has low stiffness for small deformations, followed by a heel region where stiffness begins to increase, then a linear region with much greater stiffness [38]. Collagen fibres are mainly responsible for bearing tensile loads; in a neutral state, the organization of these fibres is a wavy pattern that has been referred to as crimp [39]. When these fibres are stretched, they initially

straighten with minimal resistance, explaining the toe region. Once more tensile load is applied, the fibre completely straightens out, allowing it to bear more load with less deflection [39]. As the applied force increases, all fibres within the tissue contribute to bearing load and so stiffness continues to increase. Once all fibres are stretched and load bearing, the stiffness of the AF tissue can be characterized as linear. The area around these fibres is the extrafibrillar matrix, which is the main contributor to bearing compressive loads within the AF. Permeability and diffusivity are also closely attributed to properties of the extrafibrillar matrix [39]. Elastin fibres lie both within the lamellar layers as well as between them, and support the disc when returning to a neutral position following deformations caused by bending or twisting of the spine. As a result, they play a significant biomechanical role during daily loading [40] [41]. The Young's modulus and Poisson's ratio describing the elastic properties of the AF tissue have generally been characterized as isotropic [42], demonstrating little directional dependence. However, from the perspective of nutrient transport, there are much more dramatic directional dependencies [43].

There have been significantly fewer studies conducted regarding the biomechanics of the cartilaginous endplates compared to the NP and AF. The endplates support the disc and adjacent vertebral bodies on both superior and inferior sides of the disc. The thickness of the endplate has been shown to decrease with age and degeneration [39]. When a compressive load is applied to the disc, the endplate prohibits expansion of the NP and helps to contain the water within the NP. This is important for the NP's ability to generate and maintain hydrostatic pressure under load [44]. In addition to its structural importance, another significant role of the endplate is to act as a permeable structure to facilitate and maintain the proper diffusion of nutrients and waste products into and out of the avascular disc tissue, respectively.

Understanding the mechanical behaviour of the healthy disc is essential for understanding degenerative changes, and ultimately for making informed clinical decisions regarding treatment options to best maintain or restore disc health and function.

#### **1.4 Effect of degeneration on mechanical behaviour**

Degeneration is unavoidable and inevitable as an individual ages. These degenerative changes affect the composition and structure of the intervertebral disc tissue. These changes at the microscopic level ultimately influence the material properties, mechanical behaviour, and failure properties of the disc at the macroscopic level, and are outlined in this section.

One of the first and most significant changes to the biochemistry of the disc from degeneration occurs in the NP as a loss of aggrecan [45], which can affect the behaviour of the spine. As these proteins degrade, the resulting smaller fragments leach from the tissue more easily than healthy ones. This leads to a loss of glycosaminoglycans (GAGs), causing a drop in the osmotic pressure and ultimately a loss of hydration of the disc matrix. Due to the loss of hydrostatic pressure in the NP during the initial phase of degeneration, the disc becomes less stable and prone to hyperflexion [46]. As degeneration progresses, the NP becomes less gel-like and more fibrotic via a gradual change in collagen type [47]. The decay of the NP is thought to be one of the largest enablers of the degenerative cascade in the disc [46].

Changes to the collagen fibre network of the AF are not as obvious as changes to those of the NP. Unlike the loss of aggrecan from the NP, the overall quantity of collagen fibre stays very similar throughout the degenerative process. Rather, there is often a change in the types and distribution of collagen fibres. Degeneration in the AF is most often identified by a loss of organization within the structure of the tissue: The type II collagen often becomes denatured, and

this increases as degeneration progresses [48]. This leads to the lamellae becoming irregular and bifurcating, with a noticeable decrease in the number of lamellar layers in the AF and an increase in thickness and spacing of the lamellae [49]. The elastin networks also become disorganized with increased degeneration.

The relationship between degeneration and IVD mechanical properties has also been investigated on several occasions. A study of the of the NP's material and mechanical properties in 19 lumbar specimens showed an increase in shear modulus by a factor of eight between healthy and severely degenerated discs, with a general transition from fluid-like to solid-like behaviour throughout the degenerative process [50]. Additionally, there is an increase in the shear modulus of the AF, although not as significant as in the NP. There is, however, a significant increase in the compressive modulus of the AF [51].

Changes to the mechanical properties of the individual disc tissues due to degeneration strongly influence the disc's response to loading conditions. Studies have shown that the degenerative cascade initially starts with increased flexibility and hypermobility of the spine, which suggests that this contributes to painful limitation of motion [52], [53]. As degeneration advances, however, it eventually leads to hypomobility caused by stiffening of the tissue and other compositional changes noted earlier in this section. Moreover, the ability of the disc to dissipate energy is significantly reduced [54]. Multiple studies have reported an increased creep rate as a result of degeneration [55] [56]. The loss of aggrecan means that the disc is less capable of maintaining proper water content under load. Therefore, they lose fluid more rapidly when loaded, causing a loss of height of the disc with increasing degeneration. As a result, discs are more prone to bulging and herniation [57]. The loss of disc height can also lead to increased contact, and resultantly higher load transfer, at the facet joints [58]. Furthermore, the disc no

longer behaves hydrostatically under load due to the loss of hydration [59], which may result in higher stresses in the AF and/or the endplate.

Increased disc degeneration (assessed using both MRI and radiograph) is associated with reduced ROM in both flexion-extension and lateral bending [60]–[62]. Furthermore, hysteresis area has been found to be higher in degenerated discs as compared to healthy ones, likely due to the loss of water content and change in disc structure that is associated with the progression of degeneration [60], [63]. Additionally, degenerative discs have shown increased stiffness in the high flexibility zone for three main types of rotation: flexion-extension, lateral bending, and axial rotation [61], [64]. An important thing to note is that the biomechanics of healthy versus degenerated discs have been indistinguishable for low loads; it is only under high compressive loads and/or applied moments that degenerated discs were able to be kinematically distinguished from healthy ones [60]; this highlights the importance of investigating the effect of degeneration on disc mechanics under physiologically relevant loading conditions.

While all of these changes, both morphologic and mechanical, have been investigated and reported, it has been extremely difficult to establish how they all fit together. Moreover, we are currently unable to distinguish those that occur naturally with age from those that are clinically relevant and that might contribute to or cause lower back pain [57].

## **1.5 Clinical motivation**

### **1.5.1 Current assessment methods for disc degeneration**

Discography is one technique that is currently used for clinical assessment of disc degeneration, despite the fact that the specificity of discography tests for symptomatic disc



degeneration has not been clearly demonstrated [65]. It is most commonly used to provide evidence that a patient's symptoms are a result of discogenic pain. Discography allows the anatomic structure of the IVD to be studied using both static and dynamic imaging, and is done during and after an injection of a contrast agent. The injection can often provoke a pain response, and a patient's response to the injection is noted. The patient is also asked if the pain experienced during the injection is similar to the pain they usually experience in their lower back. However, diagnosis by means of discography holds a rather controversial position within the medical community and the scientific basis for the test has not been validated [65]. Several studies have found other factors, such as a patient's emotional state and psychological influences, to result in high rates of false-positives in diagnosis of discogenic pain [66]–[68]. Furthermore, this technique is highly invasive, and so alternative means of diagnosing pathological discs using solely non-invasive techniques, such as grading systems used with medical imaging, have been explored.

While a large variety of grading systems for disc degeneration have been developed and used for both research and clinical assessment of disc degeneration, none have accurately linked degenerative changes to clinical symptoms. These grading systems are based on a number of factors, including macroscopic anatomy, histology, plain radiography, magnetic resonance imaging, and discography. In an extensive review of existing grading systems, 42 systems were identified [69]. Of these, only five had been used in conjunction with inter-observer reliability tests for the developed method, and only four fulfilled the author's criteria for recommendation: Thompson et al [70], Boos et al. [71], Lane et al [72] and Pfirrmann et al. [13]. The methods established by Thompson et al. and Boos et al. are generally used for research assessment, as the assessments are based on histologic variables and can only be performed on cadaveric

specimens. The methods of Lane et al. are the most clinically feasible as they rely solely on radiographs, which are readily obtained in a clinical environment. Pfirrmann et al. also established a clinically feasible method that assesses disc health based on MRI scans. Although not as readily obtained as radiographs, Pfirrmann et al.'s method provides more clinical information than that of Lane et al. since the disc tissue can be directly assessed by MRI, whereas methods relying on radiograph can only assess bony structures surrounding the disc. A diagnostic evaluation of LBP based on MRI disc morphology reported ranges of 60 to 100 % sensitivity and 43 to 97 % specificity [73].

Currently, Pfirrmann et al.'s classification method is often used for grading of lumbar disc degeneration in a clinical setting for T2-weighted MRI scans. The grading system identifies changes such as a loss of signal intensity, loss of distinction between the nucleus and the annulus, and decreased height of the disc space. The Pfirrmann grade has been shown to effectively describe gross anatomic variations and morphologic changes [13].

Despite the proven sensitivity of MRI to changes in the intervertebral disc, there is still uncertainty as to the clinical relevance of MRI findings; current methods cannot distinguish between degenerative changes occurring naturally due to aging, and those that may be considered pathological. A study on a group of entirely asymptomatic patients who received MRI scans of the lumbar intervertebral disc reported that in individuals under the age of 60, 54% showed evidence of a bulging disc, which increased to 79% in individuals over the age of 60 [74]. Furthermore, degenerated discs (defined as a loss of signal on a T2-weighted scan and a loss of disc height) were noted in 34% of individuals under 60 years of age, and in all but one of patients over 60. Studies such as these suggest that, to a certain degree, bulging and degeneration

of the disc are a common aspect of the aging process. The difference between degeneration in asymptomatic and symptomatic individuals is currently not understood.

The established anatomic and morphologic changes associated with degeneration, derived from medical imaging, are simply not enough to properly understand degenerative changes leading to painful discs. Since the role of the disc is mainly mechanical, incorporating information regarding the mechanics of the disc in addition to anatomic and morphologic changes could help bridge that gap between known degenerative changes and clinical symptoms. While there is currently no method to directly assess disc mechanics *in vivo*, recent research has shown that MR parameters are linked to mechanical properties of the disc [15]. If we can better establish the relationship between mechanics of the disc and these MR properties, then this can be utilized to provide more clinically relevant information regarding disc degeneration.

### **1.5.2 Conservative treatment methods for discogenic pain**

Lower back pain is a leading cause of disability, and the economic burden is estimated to be in the range of 20 to 120 billion dollars in the US alone [4]. Therefore, an objective and accurate assessment method for detecting and diagnosing LBP is vital. Currently, no such tool exists. A systematic review of LBP studies showed that, for MRI studies of LBP, seven of 10 had positive likelihood ratios (+LRs), while few had negative LR [75]. These ratios are defined as:

$$+LR = \frac{sensitivity}{1 - specificity}$$
$$+LR = \frac{1 - sensitivity}{specificity}$$

These results indicate that a positive result (such as a high intensity zone, described as a considerably bright and concentrated region of signal intensity, on a T2-weighted MRI scan) has an increased probability of the disc being a source of LBP. The results, however, were

heterogeneous across the 10 studies, and so an accurate prediction of the diagnostic strength of such tests is difficult to establish. Furthermore, a lack of negative LR indicates that a negative test result (indicating a normal, healthy disc) does not eliminate or reduce the likelihood of the disc being the source of pain. There is currently no test available clinically to fully assess the likelihood of the IVD as a source of LBP [75].

Few nonsurgical interventional therapies for low back pain have been shown to be effective in randomized, placebo-controlled trials. These interventions include injections of medications or enzymes into surrounding tissue of the spine, applying thermal or radiofrequency energy into the spine, and spinal cord stimulation. In recent decades, there has been a drastic increase in the utilization of non-surgical interventions for LBP. From 1994 to 2001, there was a 271% increase in epidural steroid injections for discogenic pain in the American Medicare population, despite little evidence that such practices are effective. Despite this drastic increase of such therapies, there was no evidence of associated improvements to LBP patient's health status [76]. The utilization of interventional therapies has not been clinically motivated by evidence. Rather, a promising case study or series, or other observational studies, has motivated adoption of specific interventions. Given the continuous rise in utilization rates, high costs, and potential harms that coincide with nonsurgical interventional therapies, a clinical tool to effectively and accurately measure outcomes for different treatment methods is highly desired in order to guide their appropriate use.

## **1.6 MR imaging of the intervertebral disc**

MRI is most commonly used to assess soft tissue within the body and to detect the presence of abnormalities within those tissues such as lesions, tumours, and herniation. A major

advantage of MRI scans as an assessment tool is that unlike x-ray and CT, MRI requires no ionizing radiation, and therefore is a much safer than these other imaging methods [77].

Images are produced using a set of pulsed radiofrequency (RF) gradients, called a sequence. By changing the applied and collected RF pulses, different types of images can be created. The most common are T2-weighted, T1-weighted, proton density, and diffusion-weighted sequences. Each of these sequences can highlight unique properties of the tissue that may not be apparent on another sequence type. For the remainder of this thesis, we focus solely on diffusion-weighted sequences, which highlight the diffusion properties of water within biological tissues.

### **1.6.1 Principles of MRI and diffusion-weighted imaging**

Every tissue in the human body has a different amount of water, and a different structure through which that water can move, or diffuse. Some conditions—such as acute stroke or disc degeneration—disturb these established patterns. Detection of these abnormalities can provide physicians with important information for both diagnosis and treatment of various medical conditions [78].

Diffusion weighted imaging (DWI) detects the random movements of water molecules within biological tissues. Generally, water can diffuse freely within the extracellular space, while it is much more heavily restricted movement in the intracellular space. When something disrupts the ability for water to flow freely (such as the uptake of water from the extracellular to the intracellular space in ischemic brain tissue), this information is captured on a DWI scan. DWI has proven to be very useful for the characterization of tissue properties [78].

DWI scans can also be used to create apparent diffusion coefficient (ADC) maps, which display the properties of diffusion alone, with all T1 and T2 effects removed [79], [80]. Further details of this effect and the calculation of the ADC values are outlined further in this section. The generation of the ADC map allows for quantification of diffusion properties, which has proven to be a very useful clinical tool in other applications [81], [82]. Currently, the most common applications of diffusion imaging and ADC maps are detection of tumours and lesions, especially in the brain, where ADC maps are used for detection and of ischemic stroke [83], [84]. Furthermore, recent studies have shown that DWI has a promising future applied to imaging the intervertebral disc [15], [85], which has great significance as it could establish the first method to non-invasively investigate the mechanics of the disc in a clinical environment.

A diffusion imaging sequence can be added to almost any conventional MRI sequence, however it is common practice to use echo planar imaging (EPI) for diffusion-weighted imaging. The difference between classic EPI and diffusion-weighted EPI is the addition of two gradient pulses applied along the phase encoding direction (Figure 1.3). The first pulse dephases the magnetization of the spins, both moving and stationary. The second pulse rephases the magnetization of the spins, but only the stationary spins can re-phase completely; protons undergoing diffusion will have shifted position, and therefore acquire a non-zero phase dispersion. There will be stronger signal dampening for tissues that have relatively fast diffusion compared to tissue with slow diffusion (Figure 1.4). Free water will experience the most attenuation of signal, and is often used as a reference.

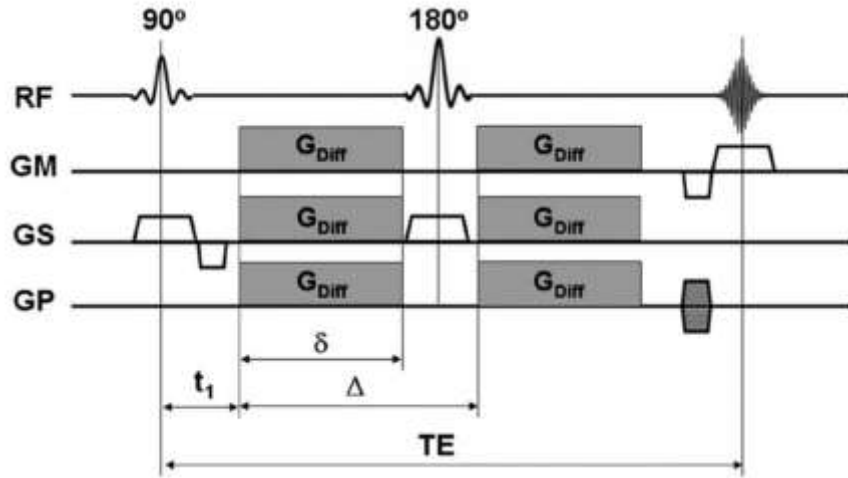


**Figure 1.3 Typical diffusion-weighted pulse sequence**

© Reproduced from [86], with permission



**Figure 1.4 (A) typical T2-weighted scan and (B) same image slice collected using a DWI sequence**

*The diffusion-weighted scan highlights the diffusion of free water, evident to be much higher in the disc and spinal cord than any of the surrounding tissue, a property not discernable on the T2-weighted scan. © Reproduced from*

*[8] with permission*

In DWI, the sensitivity to diffusion is determined by the b-value. The b-value is related to the strength and duration of the diffusion gradients, and is given by the following relationship

$$b = \gamma^2 G^2 \delta^2 (\Delta - \frac{\delta}{3})$$

Where:

- $\gamma$  is the gyromagnetic ratio;
- $G$  is the amplitude of the diffusion gradient;
- $\delta$  is the duration of each diffusion pulse;
- $\Delta$  is the time between the two diffusion pulses; and

The collected signal is then related to the b-value by the relationship.

$$\frac{S}{S_0} = e^{-bD}$$

Where:

- $S$  is the diffusion-weighted signal;
- $S_0$  is the signal intensity without diffusion weighting;
- $b$  is the diffusion weighting, defined above; and
- $D$  is the diffusion constant.

It is important to note that a b-value of 0 results in a traditional T2-weighted image. This is often performed first to get an anatomical reference image to which the DWI scan can be compared. Clinically, the b-value typically falls in the range of 0 to 1000 s/mm<sup>2</sup>, where the higher b-values (i.e. higher diffusion weighting) often corresponds with better contrast of pathogenic regions, especially for detection of ischemic stroke [78].



Multiple directions must be measured for each b-value. Clinically, a minimum of three is often required, however this number can increase to much higher values. This is due to the anisotropy of human tissue. By applying diffusion gradients in all three dimensions, the information can be collected and averaged to produce an image that measures diffusion strength independent of anisotropy.

The signal intensity of the diffusion-weighted image is given by the following relationship

$$S_{DWI} = S_{b=0} * e^{-b*ADC}$$

Where

- $S_{DWI}$  is the signal intensity of the diffusion weighted image
- $S_{b=0}$  is the signal intensity of the image when diffusion weighting is zero
- $b$  is the b-value of diffusion weighting

This can be re-arranged to show how the ADC value is calculated

$$ADC = -\frac{1}{b} \ln\left(\frac{S_{DWI}}{S_{b=0}}\right)$$

One major disadvantage of DWI on its own is what is known as “T2 shine-through.” This phenomenon is a result of all diffusion images having T1 and T2 contrast in addition to the desired diffusion contrast. Therefore, a hyper-intense region on a diffusion image may be a result of strong T2 signal, rather than an indication of an area with restricted diffusion. A solution to getting around this effect is using ADC maps, which highlights diffusion properties only while eliminating these undesirable contributing factors from T1 and T2 relaxation.

ADC maps are calculated from several diffusion-weighted scans, each having a different amount of diffusion weighting. However, this change in diffusion weighting (i.e., the b-value) does not affect the T1 and T2 relaxation. Therefore, when the ADC is calculated as the change

between these diffusion scans, the T1 and T2 properties, which remain consistent throughout each diffusion scan, can be removed from the displayed image.

### **1.6.2 Diffusion-weighted imaging of the intervertebral disc in the literature**

Within advances in MR technology and sequencing within the last two decades, DWI and ADC mapping are emerging as a critical tool for investigating degeneration of the IVD.

Historically, MRI was considered unsuitable for measuring biochemical alterations linked to lumbar disc pathology; the position deep within the body and large amount of tissue-bone interface was found to cause significant signal attenuation and artifacts on DWI scans, leading to the conclusion that DWI was not sufficiently reliable to monitor lumbar disc pathology *in vivo* [87].

One of the first studies on the IVD using DWI and ADC maps aimed to compare ADC values in the disc for people with degenerated discs, or potentially degenerated discs, as a result of vertebral trauma to the ADC values of a healthy control group [88]. They reported lower ADC values in discs adjacent to a vertebral fracture than those of the control group, including discs that had normal signal intensity in T2-weighted scans. This suggested that DWI might be sensitive to disc structure abnormalities, as these were areas where degeneration would likely occur as a result of the neighbouring vertebral fracture.

Since then, several studies have been done to categorize the relationship between ADC and age, disc region, and degenerative grade and have reported a wide variety of significance and sensitivity levels. ADC was negatively correlated with age within the NP tissue, but had no correlation in the AF tissue in an *ex vivo* study of 14 lumbar specimens [85]. Another study of 44 men, between 29 to 86 years of age, found no correlation at all between ADC and age [89]. More recently, mean diffusivity calculated from DWI scans was found to decrease with age in a study

of 30 asymptomatic volunteers, with ages ranging from 25 to 67 [90]. In a later study of 109 patients and 545 lumbar discs, the same group reported a strong negative correlation between ADC and age, with a stronger correlation at the L3/4 and L4/5 levels [91]. Other studies have also reported stronger correlations between ADC and age at the lower lumbar levels [89], [91]. There was a statistically significant decrease in ADC in the NP with a loss of disc height in a study that looked at diurnal variation in the disc throughout the course of a day [92]. There is generally agreement in the literature regarding mean ADC values in the main regions of the disc: the NP has consistently been reported to have larger mean ADC values than the AF [15], [85], [93], [94].

While studies have consistently correlated ADC to the degenerative state of the disc, findings have not all been in agreement. Numerous studies have reported a negative relationship between ADC and severity of degeneration [85], [89], [91], [93]–[95]. However, another study found a decrease in ADC with mild and moderate levels of degeneration, but found an increase in ADC for the most severe level of degeneration [95]. They postulated that the most severe state of degeneration led to a lack of fluid containment, increasing the ability for free water to pool in open cracks and fissures, creating a strong diffusion signal. No other studies replicated such findings. ADC has also shown promise in detecting changes in the intervertebral disc as a result of degeneration through the detection of Modic changes, which are a classification of pathologic changes to the vertebral endplates on MRI scans. ADC was found to increase for Type I Modic changes to vertebral endplates, and a decrease in ADC for Type II Modic changes in a study of 100 patients with lumbar spine degeneration [93].

One of the most promising recent studies suggesting ADC may be a useful tool to detect early changes to disc function was an *ex vivo* investigation assessing the relationship between

ADC and compressive loading of the disc. They found significant changes in diffusion and corresponding ADC values under different two different loading conditions – 200 N and 800 N loads, simulating supine and standing postures of the spine – in a study of 5 lumbar cadaveric specimens spanning several degenerative levels (classified as grades II-IV, using axial T2 mapping as described by Watanabe et al. [96]) [15]. The study assessed how compressive loads affected the ADC and the coefficient of variance (COV), defined as the ratio of standard deviation to the mean, in different regions of the disc. Loading caused significantly lower ADC values (25.3%) and higher coefficient of variance (COV) values (42.5%) in the NP, nearly twice that of the annulus with 12.7 and 18.9% for ADC and COV values respectively. The posterior region of the disc had lower mean ADC and higher COV (14.5 and 21% respectively) as compared to the anterior region.

## **1.7 Summary and objectives**

### **Summary of the literature**

Morphologic and anatomic changes to the intervertebral disc as a result of degeneration are well understood, and have been implemented into current diagnostic methods for assessing disc degeneration. However, these methods do not distinguish changes that occur naturally due to aging from changes that might be considered pathological. Moreover, clinical recommendations for discogenic pain treatment lack an objective and quantitative metric for assessing outcomes.

Changes to the mechanics of the intervertebral disc have been presented in the literature, showing indications of clinically important degenerative changes, since the role of the disc is mainly mechanical. However, we don't currently have a method to assess mechanical function

directly *in vivo*, and so there is no way to directly connect the relationship between mechanics and symptoms. Therefore, establishing a method to understand altered disc mechanics using a surrogate measurement, such as MRI properties of disc tissue, in addition to morphologic changes may help us to better understand the relationship between degeneration and discogenic pain.

Diffusion weighted imaging and apparent diffusion coefficient maps are emerging as useful diagnostic tools, and show great potential for application to the investigation of the intervertebral disc. ADC has been shown to be sensitive to different loading conditions and shows promise to be an effective tool for establishing altered disc mechanics in early stages of degeneration. However, investigation of ADC under load is still preliminary; the effect of different loading conditions (such as flexion and extension of the spine) on the ADC values in the disc has not yet been established.

## **Objectives**

The main goal of this thesis was to build on the recent findings that ADC measurements are sensitive to different loading conditions to further explore the relationship between ADC and loading conditions. Previously, only two loading conditions (supine and standing) were investigated; we aimed to expand on this to incorporate bending of the spine (flexion and extension).

In order to determine this relationship between ADC and loading condition, we required a method to measure ADC values within, and forces acting on, the disc. The latter was necessary in order to verify that forces applied to the disc fell within known ranges for the postures that the loading conditions intended to simulate. The objectives for this thesis were to:

1. Develop a method for measuring forces acting on the intervertebral disc in the MRI environment;
2. Develop a protocol for measuring the Apparent Diffusion Coefficient (ADC) in the intervertebral disc using diffusion imaging on the 7 T MR scanner; and
3. Determine the relationship between ADC values and simulated physiological loading conditions (supine, upright standing, flexion, and extension) in both healthy and degenerated discs.

## **Chapter 2: Design and validation of an MRI-compatible load measurement system**

This chapter addresses the first objective of this study by outlining the process for developing and validating a method to measure physiologically relevant forces applied by the loading apparatus to the lumbar intervertebral disc in an MRI environment through the use of Fibre Bragg Grating (FBG) sensors. The chapter outlines the following key steps in the development of the load measurement system:

1. Reviewing past and current methods for measuring joint loads in the MRI environment;
2. Integrating the FBG sensors into the joint loading rig setup; and
3. Calibrating the system in the biomechanics test lab for use in the MRI environment.

### **2.1 Motivation**

When using sensors in the MRI environment, proper steps must be taken to ensure full safety and electromagnetic compatibility of the entire sensing system. Any electromagnetic signal generated by the sensor can interact with the strong magnetic field (both static and dynamic gradients) generated by the MRI, causing distortions or artifacts on the resulting scans and, in extreme cases, causing injury through movement of the metallic object. For biomechanics studies that use high-field MRIs, such as the Bruker Biospec 70/30 7.0 Tesla MRI scanner, limited space in the decreased bore size of 20 cm must also be taken into consideration when implementing a sensing system. Currently, there is no standard method for measuring biomechanical loads acting on the intervertebral disc in an MRI environment.

Conventional sensors such as strain gauges, force/torque sensors, or camera-based systems that produce a digital signal can be used only if placed sufficiently far away from the imaging region. These conventional systems also require sufficient shielding and filtering to ensure that the electronics for the system are not at risk of electromagnetic interference. However, shielding and filtering can only minimize, rather than eliminate, the effect of electromagnetic interference.

When conducting biomechanical investigations, it is often important to replicate relevant physiological loading conditions, such as that of standing and leaning forwards. As such, it is desirable to apply loads up to 2500 N in an MRI environment. The purpose of this study was to validate the use of fibre optic force sensors in an MRI environment for loads applied to a functional spinal unit in the range of 0 to 2500 N.

## **2.2 Review of current MRI-compatible load measurement systems**

There are several versions of both off-the-shelf and custom designed devices that have utilized fibre optic technology for force measurement in the MRI environment and have demonstrated the potential that this technology has [97]–[102]. However, none of these studies so far have measured forces of magnitudes as large as those experienced by the intervertebral disc *in vivo*.

Off-the-shelf devices that use fibre optic technology, such as a pinch sensor (Model LMD300, Futek, Irvine, CA) and a hand gripper (Model LMD500, Futek, Irvine, CA) have been developed for medical use. A conventional 6-DOF load cell with metallic load sensing elements (Model 45E12A-Z1, JR3 Inc., Woodland, CA) has been used in the MRI environment [97]. In the JR3 sensor, components were manufactured out of non-ferromagnetic materials including



brass, titanium, and aluminum. The use of such a load cell is a very common technique in measuring forces acting on mechanical joints in biomechanics laboratory studies, and the methods were expanded for use in areas significantly influenced by the MRI magnetic field. While using non-ferromagnetic materials make this type of load cell safe to bring into the MRI environment, there are several issues that have been reported with using such metals during an MRI scan. RF heating of conducting materials is a concern, and must be taken into consideration when considering the use of metals in MRI [98]. Furthermore, if the metal-containing force sensor is within or near the field of view during the scan sequence, they can produce artifacts distorting the image, leading to false interpretation. The electrical equipment interfacing with the load cell or sensor can also emit electromagnetic noise that can interfere with the scan sequence. Finally, inadequate shielding and filtering can lead to inaccuracies in the data collected by the force-sensing system caused by RF interference within the scan room. Currently, there are no clear standards for using electronic equipment within the MRI environment.

An alternative solution to conventional force-sensing systems for the MRI environment that has been reported in the literature is the use of fibre optic technology. Because fibre optics use a magnetically inert transmission medium (light), it ensures that there is complete electromagnetic decoupling between the sensor within the MRI room and the electronics it interfaces with, which can then be placed in the control room away from the MRI environment. Because the transmission of light through optical fibres has small losses over long distances, there is minimal effect on the strength of the force-sensing signal when placing the electronic components outside the MR room. Within the realm of fibre optic solutions, a specific type of sensor has emerged as an exceptionally useful tool for medical applications: Fibre Bragg Grating

(FBG) sensors. These sensors are biocompatible, electromagnetically inert, and quite small with typical diameters in the range of 20 to 400  $\mu m$ .

Several studies have explored using Fibre Bragg gratings in the MR environment: a fibre optic grip force sensor has been developed from 3D-printable materials, used to measure forces up to 400 N in the MRI environment [99]. A FBG strain sensor used to monitor patient vital signs during an MRI scan has been used [100], as well as a FBG force sensor for soft tissue mechanical property investigation in the MRI environment, measuring forces up to 15 N [101]. Furthermore, FBG sensors have been used to simultaneously measure contact force and fluid pressure in cadaveric hip joints [102].

These reported studies have shown the advantages and potential that fibre optic technology has in the MRI environment, but have only been used in applications with loads to a maximum of 500 N. This is inadequate for the intervertebral disc, where loads of over 2000 N are routinely experienced during activities such as standing, walking, flexion or extension of the spine while standing, and lifting weights [34], [103], [104].

### **2.3 Principles of Fibre Bragg Grating sensors**

Fibre Bragg grating (FBG) sensors measure strain by a change in distance between the gratings that results from the applied strain, leading to a shift in the reflected wavelength of light. Typically, FBG sensors for measurements of mechanical properties such as strain and temperature are single mode fibres [105]. The mode of the fibre is determined by the mode of light transmission governed by both optical and geometric properties of the fibre. The core diameter of a single-mode fibre is smaller than multi-mode fibres, and has minimal attenuation of light passing through the cable compared to multi-mode fibres. As a result, single mode fibres

are desirable for applications such as force measurement in an MRI environment when signal strength is critical and space can be extremely limited [102].

The lengths of the FBG as well as the refractive index of the core of the fibre determine the optical spectrum that is reflected by the FBG. There is a broad band of wavelengths incorporated in the light transmitted through a typical optic fibre. A spectrum of wavelengths with a single peak is reflected when this light reaches the Bragg grating (Figure 2.1). The centre of this peak is called the Bragg wavelength, denoted as  $\lambda_B$ . The Bragg wavelength can be calculated from the following relationship:

$$\lambda_B = 2\Lambda n_{eff}$$

Where  $n_{eff}$  is the effective refractive index, and  $\Lambda$  is the grating period [106], which is the distance between the gratings of the FBG sensor (Figure 2.1). These properties determine the shape of the reflected spectrum. The magnitude of the Bragg wavelength and the maximum reflectivity are properties of the optical interrogating equipment used in conjunction with these types of sensors [105].

Fibre Bragg Grating sensors have been well established in the literature for measurement of strain. When a force is applied along the axis of the cable, the distance between gratings changes. These changes to the grating period and index ultimately cause a shift in the Bragg wavelength of the fibre, given by

$$\Delta\lambda_{BS} = 2\left(\frac{\Lambda\partial n_{eff}}{\partial l} + n_{eff}\frac{\partial\Lambda}{\partial l}\right) * \Delta l$$

Where  $\Delta l$  is the change in length of the FBG due to strain [10].

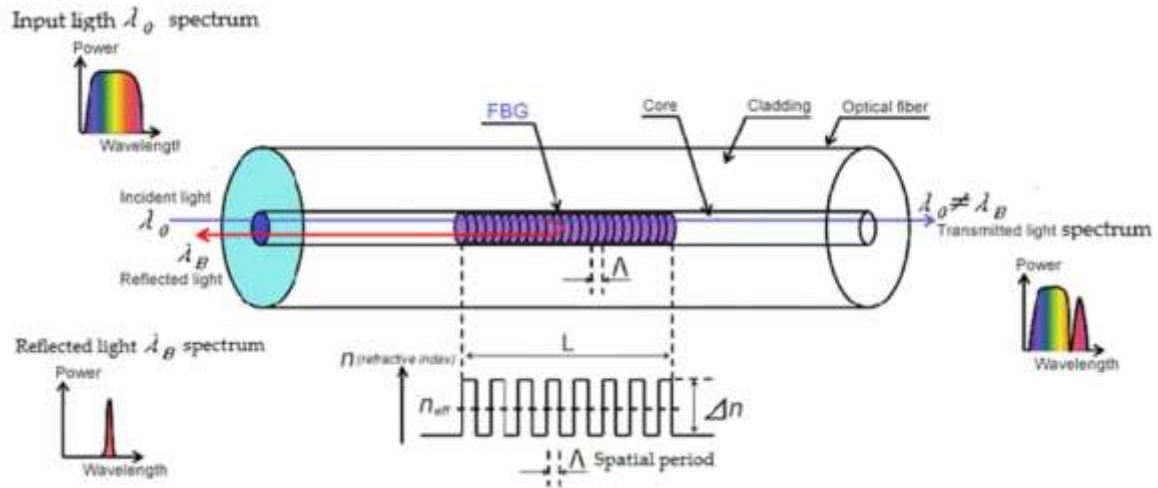


**Figure 2.1 Schematic of FBG sensor**

© Reproduced from [107], with permission

## 2.4 Design requirements

Our overall objective was to develop a system that can interface with a custom designed rig capable of applying compression and bending loads to a functional spinal unit (FSU) in the range of 0 to 2500 N. Details of the rig designed are outlined in the next chapter, and will be referred to as the ‘loading rig’ throughout the remainder of this chapter. The goal was to directly measure the force transferred through the lumbar intervertebral joint by the loading rig within the MRI environment in real time. Additionally, it was desirable to have the FBG sensor setup be transferrable from the lumbar joint loading rig to similar rigs for other projects (e.g., knee and hip joint loading rigs) that were concurrently conducting experiments in the 7 Tesla MRI scanner. This led to the list of design criteria below.

- Safely operate in the MRI environment without interference to or from the magnetic field;
- Measure force generated on a lumbar IVD by the loading rig within the bore of the Bruker Biospec 70/30 7.0 Tesla MRI;

- Transmit the measured force out of the MRI scan room to the control room with minimal loss of signal;
- Measure forces within the range of 0 to 2500 N with accuracy comparable to previous studies; and
- Be transferrable to other joint loading rigs with similar dimensions.

## **2.5 Final design**

### **Sensor Configuration**

Single mode fibre FBG sensors were manufactured (Technica SA, Atlanta, GA) – refer to Appendix A for specifications for the custom FBG sensors. A 0.015 m length of fibre optic cable between the FBG and the tip was added so that the fibre could be pulled in tension and secured to the acrylic tubing. This ensured the fibre lay flush against the surface of the acrylic while the light-curing adhesive was applied, which was crucial for proper transfer of load from the acrylic to the fibre for a linear response.

To ensure the load measurement system could be transferrable to various applications, the FBG sensors were mounted to opposite sides of a piece of hollow acrylic tubing using a light curing acrylic adhesive, dimensioned to slide fit within the outer housing of the compression rig (Figure 2.2). The axes of the fibres were aligned parallel with the axis of the applied force from the differential screws. The two FBGs were aligned with the anterior and posterior sides of the FSU respectively. This allowed measurement of the relative force felt by the opposite sides of the specimen under various physiological loading conditions: unloaded (supine), axial compression (upright standing), flexion, and extension. A light-curing acrylic adhesive was used to secure the FBG sensor and fibre optic cable to the surface of the acrylic tubing (Figure 2.2) (Model AA 3525, Loctite, Dusseldorf, Germany).

The FBG sensors were left for 24 hours following the adhesion to the acrylic tubing near a natural light source to ensure the adhesive had set completely.

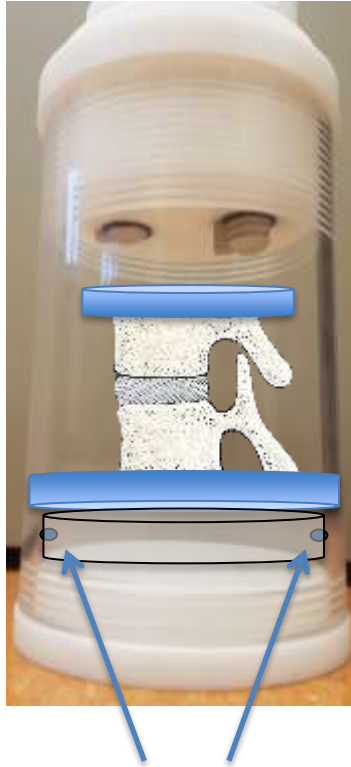


**Figure 2.2 Schematic showing placement of FBG sensor mounted to inner wall of hollow acrylic tubing within the loading rig**

### **DAQ and Interrogator system**

The FBG sensors were used in conjunction with a 16-bit data acquisition card (DAQ) (Model PXIe-56341, National Instruments, Austin, TX) and a 4-channel FBG optical interrogator (Model PXIe-4844, National Instruments, Austin, TX). These cards were used with an embedded controller (Model PXIe-8133, 4 GB RAM, National Instruments, Austin, TX) all mounted in a 9-slot DAQ chassis (PXIe-1078, National Instruments, Austin, TX).

## Component breakdown

Overall, 13 components were used in the assembly of the force measurement system. The DAQ, chassis, and optical interrogator were readily available and there was no need to purchase these for the purposes of this study; the remaining cost of the development of the system is provided (Table 2.1).

**Table 2.1 Bill of Materials for load measurement system**

Item no.	Description	Qty	Cost (\$)	Total
1	DAQ	1	N/A	N/A
2	Optical interrogator	1	N/A	N/A
3	DAQ Chassis	1	N/A	N/A
4	FBG sensor	2	81.25 (USD)	162.50
5	Acrylic tubing	1	53.58 (USD)	53.58
6	Loctite 3525	1	39.47 (USD)	39.47
7	FC/APC to SC/APC Fibre Optic Adapter	2	0.78	1.56
8	10m Single Mode Fibre Patch Cable	2	3.20	6.40
9	LC/APC Female to SC/APC Single mode Fibre Optic Adapter2	15	30	
			<b>Total (CAD)</b>	<b>\$377.84</b>

## 2.6 Validation

### 2.6.1 Calibration method

Calibration was then performed using a materials testing machine (Electropuls E10000 Linear-torsion machine, Instron, Norwood, MA). Calibration data points of the subsequent change in Bragg wavelength to applied load were recorded in a custom LabView VI (Version 10.0.1 SP1, National Instruments Inc., Austin, TX).

A custom jig was designed and manufactured to apply load simulating the force generated by the two differential screws of the loading rig (Figure 2.3). The jig applied two point loads to the loading plate, which distributed the load throughout the hollow acrylic tubing

housing the FBG sensors. The acrylic tubing was mounted to the bottom cap of the loading rig, and the FBG sensor cables fed out through the holes of the bottom cap and were secured to the base of the materials testing machine to minimize risk of the cables ripping or tearing on any edges or loose materials. The body of the jig was filled with fluid and the prongs were able to slide along the body of the jig. This was designed to ensure that equal load was transmitted through each prong of the jig to account for any small deviations in alignment of the setup to the horizontal plane.

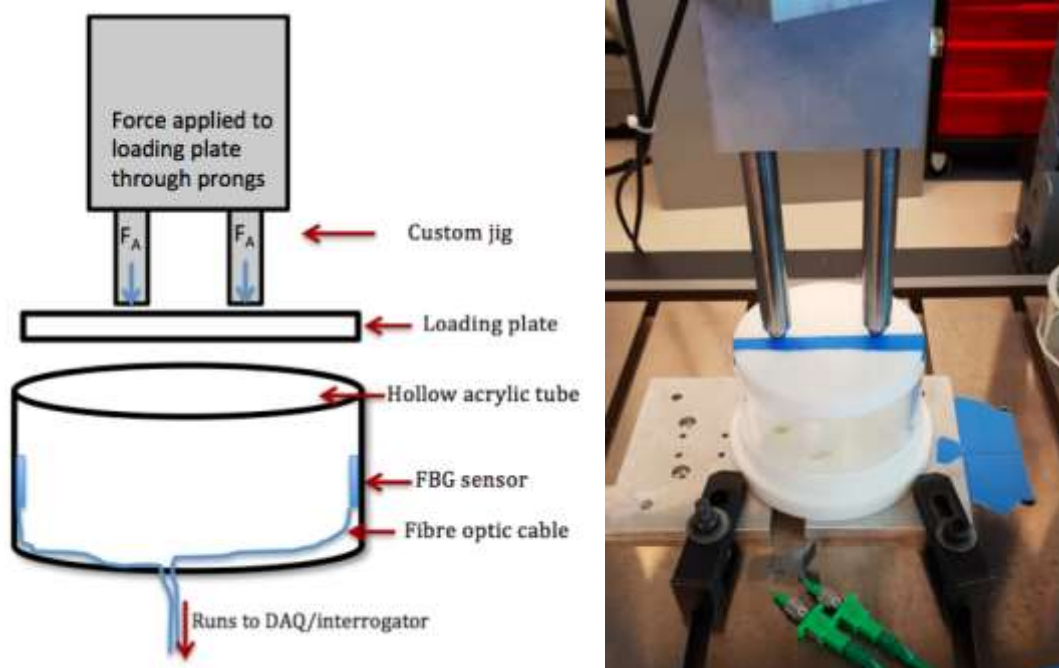


**Figure 2.3 Schematic (left) and actual (right) setup during calibration testing.**

*The custom jig applies a point load ( $F_A$ ) to the loading plate through each prong, which then distributes the load through the acrylic tube. The main body of the jig is filled with fluid so that pressure is evenly distributed and equal force is generated through each prong in case alignment of prongs with plate is not perfectly perpendicular.*

The force applied by the materials testing machine was increased using the manual positioning control thumb wheel on the removable jog handset, and allowed to reach steady-state



for a minimum of five seconds for each load-step in order to account for the viscoelastic effects of the polymer sheath coating the FBGs and cable [108]. The shift in Bragg wavelength as a result of applied load was collected using a custom LabView VI (Version 10.0.1, National Instruments, Austin, TX) that automatically recorded FBG sensor wavelengths. Prior to any load being applied to the FBG sensors (including the loading plate), the centre wavelength of each FBG was recorded and considered the baseline for the sensor; the change in wavelength for each load-step was calculated relative to this baseline.

Four sensors were calibrated and used for the duration of this study (Table 2.2). FBG-1 and FBG-2 were used together in the first configuration of the force measurement system, and FBG-3 and FBG-4 were used together in the second configuration of the force measurement system. The force measurement data collected by these configurations is presented in Chapter 3.

**Table 2.2 Calibrated FBG names and where they were used for this study**

<b>Sensor name</b>	<b>Specimen(s) tested</b>	<b>Forces measured</b>
FBG-1	H1327	Anterior side of specimen
FBG-2	H1327	Posterior side of specimen
FBG-3	H1338 H1144	Anterior side of each specimen
FBG-4	H1338 H1144	Posterior side of each specimen

### **Calculation and statistical analysis**

The sensitivity was calculated as the slope of the linear fit of the FBG centre wavelength as a function of applied load in  $[nm/N]$ . The overall calculated sensitivity for a given sensor was calculated as the average of the sensitivities for all trials.

For each dataset, the assumption of linearity was verified using a linear regression test in statistical software (SPSS Statistics, Version 23, Chicago, IL). Secondly, a plot of residual values

as a function of predicted values of the linear regression model was generated. The plot was visually inspected for heteroscedascity, which would indicate unequal variability in the measured value (Bragg wavelength) for different values of the independent variable (applied force).

## 2.6.2 Results

The shift in the reflected Bragg wavelength decreased linearly with increasing load for each of the two FBG sensors (Figure 2.4 to Figure 2.7).

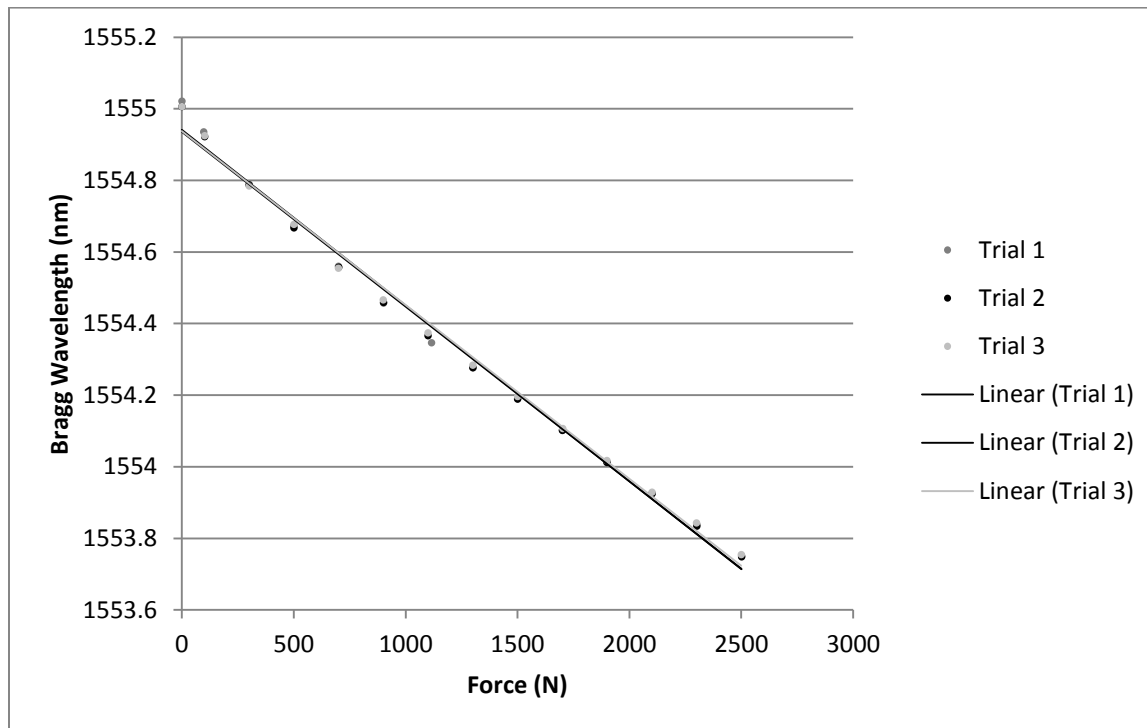


Figure 2.4 The Bragg Wavelength of FBG-1 as a function of applied force

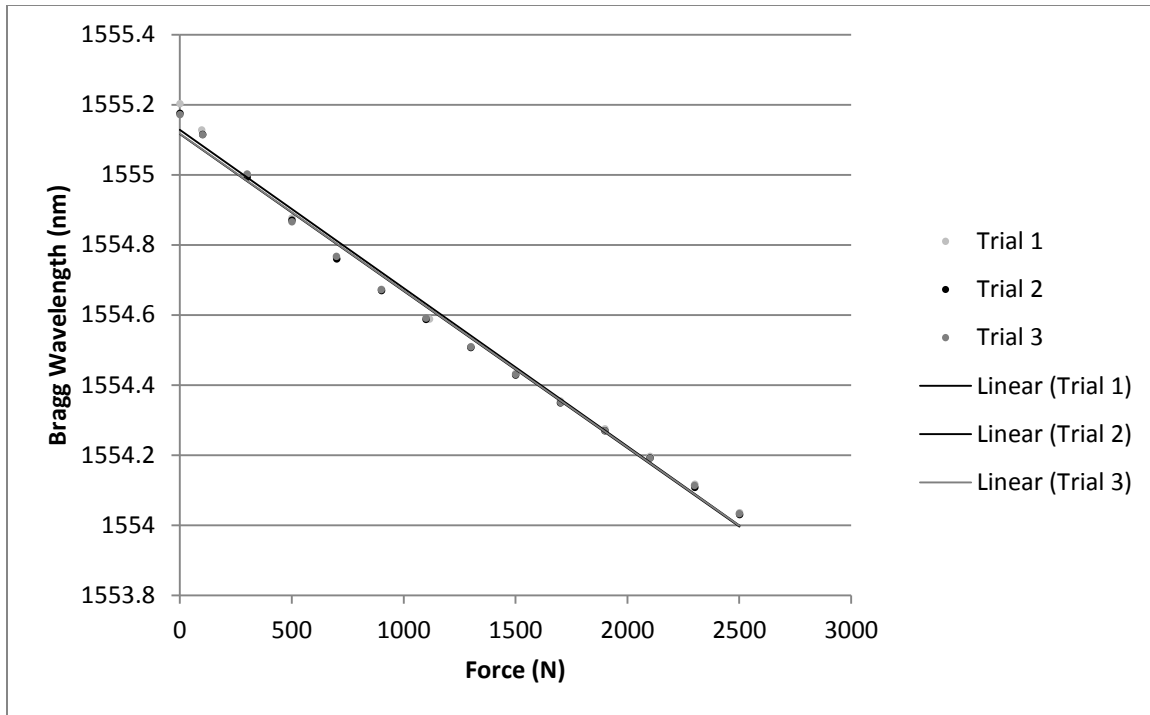


Figure 2.5 The Bragg Wavelength of FBG-2 as a function of applied force

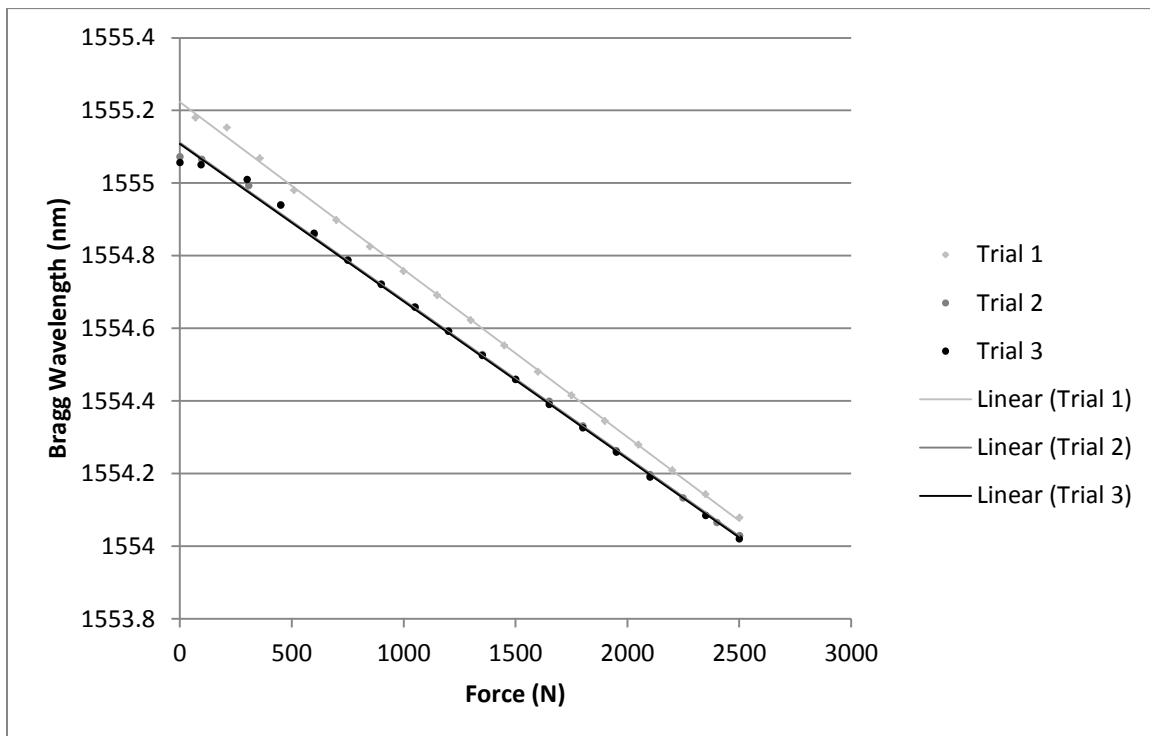
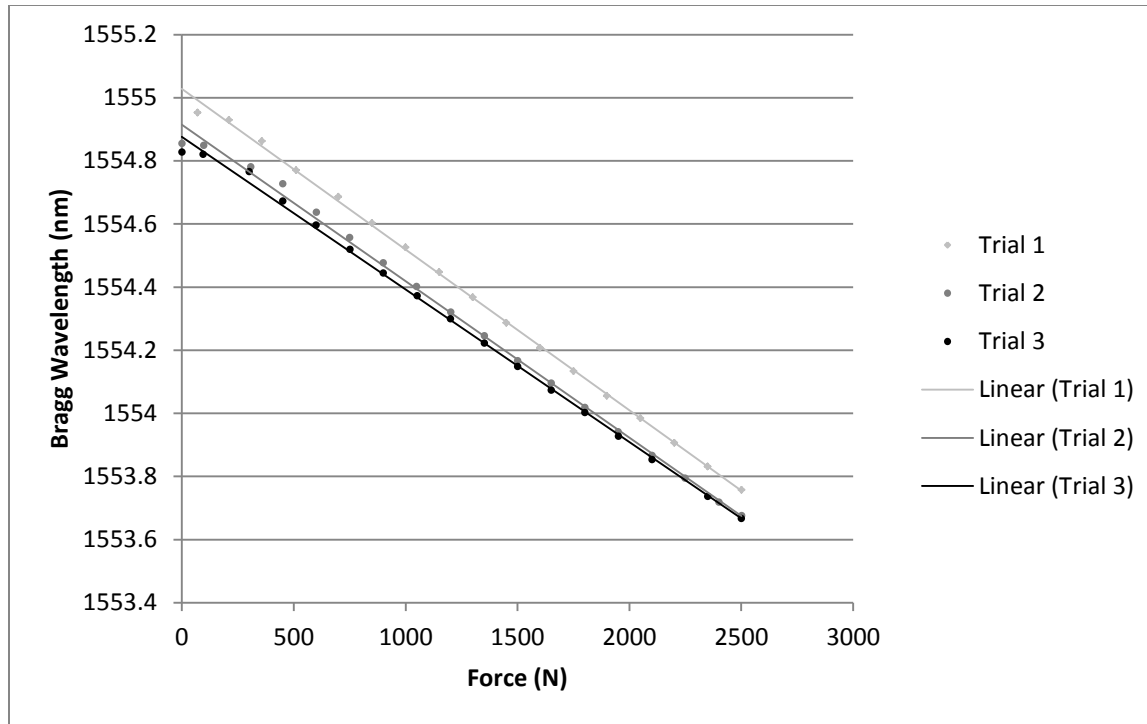


Figure 2.6 The Bragg Wavelength of FBG-3 as a function of applied force



**Figure 2.7 The Bragg Wavelength of FBG-4 as a function of applied force**

The sensitivity of the FBG sensors were calculated from the slope of a linear line fit to the measured data. Data were recorded for three different trials, each performed at different times on different days to verify repeatability and reproducibility. The first force measurement configuration (FBG-1 and FBG-2) was found to have sensitivities of 0.488 nm/N, and 0.449 nm/N, respectively. The second configuration (FBG-3 and FBG-4) had sensitivities of 0.447 nm/N, and 0.502 nm/N, respectively (Table 2.3).

**Table 2.3 Force sensitivity and R-squared values for the FBG sensors**

		Trial 1	Trial 2	Trial 3	Average
<b>FBG-1</b>	Sensitivity (nm/N)	0.491	0.488	0.486	<b>0.488</b>
	R-Squared Value (%)	99.7	99.8	99.8	-
<b>FBG-2</b>	Sensitivity (nm/N)	0.451	0.448	0.447	<b>0.449</b>
	R-Squared Value (%)	99.5	99.6	99.5	-

		<b>Trial 1</b>	<b>Trial 2</b>	<b>Trial 3</b>	<b>Average</b>
<b>FBG-3</b>	Sensitivity (nm/N)	0.451	0.439	0.442	<b>0.447</b>
	R-Squared Value (%)	99.94	99.88	99.72	-
<b>FBG-4</b>	Sensitivity (nm/N)	0.509	0.504	0.491	<b>0.502</b>
	R-Squared Value (%)	99.91	99.76	99.82	-

The significance of the linear regression model was  $p < 0.005$  for each dataset. No heteroscedascity was observed on the plot of residual values as a function of predicted values of the linear regression model for any of the FBGs (sample plot of residual for FBG-1, Figure 2.8) and so the assumption of linearity for the dataset was considered to be valid for the purposes of this study.

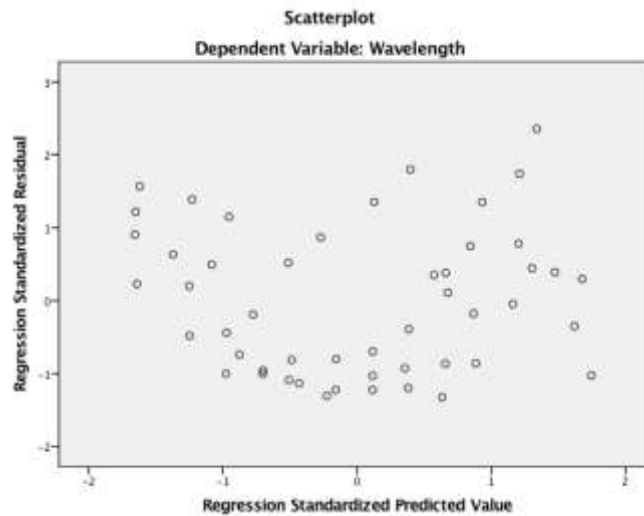


**Figure 2.8 Plot of residuals as a function of predicted value for FBG-1**

*A scatterplot with no distinct pattern or trend is a sign of homoscedascity, indicating that the variability in the measured Bragg wavelength has no significant dependence on the value of the applied force*

## 2.7 Discussion

We developed and validated a method of using FBG sensors to measure high forces (up to 2500 N) in an MRI environment. The proposed advantages of these fibre optic sensors are

their complete compatibility with the magnetic field of the scanner, their small size, and herein recorded accuracy to measure forces up to 2500 N. We analyzed the proposed design and methodology for implementation and its sensitivity to load and repeatability between experiments.

The FBG placement was chosen considering its intended use in conjunction with the loading rig outlined in Chapter 3; allowing for the simultaneous measurement of forces on the anterior and posterior side of the specimen (Figure 2.2). The custom jig for the calibration allows us to directly correlate the forces measured on the opposing sides of the hollow acrylic tubing by the FBGs to the forces applied by the differential screws of the joint loading rig. Therefore, the relative shift in Bragg wavelength corresponds to an application of load through the differential screws onto the loading plate, which can apply loads simulating supine, standing, flexion, and extension postures. This can then be used to estimate the load in the different anatomical regions of the disc under these loading conditions.

The methods developed purposely incorporated the FBG sensors via fixation to hollow acrylic tubing that can be readily added or removed from the loading rig setup. This is advantageous over permanent fixation into the device so that it can be utilized for measurement in many biomechanical joints beyond the lumbar IVD. A significant advantage of this method is the location of the FBGs within the MRI; they can be placed directly in the centre of the bore, called the isocentre of the scanner, without causing any electromagnetic interference or image artifacts. With a diameter of 250  $\mu\text{m}$  and ability to measure forces up to 2500 N, there is great potential to use these FBG sensors for surgical insertion into joints or adhered to bones to measure compressive forces in a variety of biomechanical applications. New FBGs could easily

be customized to such applications and interface with the rest of the developed system (optic cables, DAQ and interrogator, LabView VI, and Excel files) at minimal cost.

From the calculated accuracy of the FBG sensors, we determined the system to be repeatable and reproducible as these values were comparable to similar designs proposed in the literature. For lower force measurement, a 1.57% variation (calculated as the RMS accuracy) was reported for a fibre optic hand grip force sensor operable in the range of 0 to 500 N [99] and 4.1 % variation (calculated as variation from the mean value) was reported for an MR compatible strain gauge based force transducer in the range of 0.67 to 60 N [109]. The advantage of the results proposed here is the expanded operating range of forces up to 2500 N; forces acting on the intervertebral disc while standing and leaning forward at 20° produces forces on the disc have been found to be equivalent to 2x bodyweight, suggesting forces upwards of 2000 N in adults [103]. Furthermore, forces in the range of 700 – 1000 N and 1000 – 1400 N for standing and unsupported upright sitting respectively [34], [103], [110] and so the developed system has been verified to accurately measure forces within several physiologically relevant ranges for the intervertebral disc.

The increase in variation for the second assembly, as well as the shift in y-intercept of the linear fit line is most likely caused by thermal shift; output from Bragg grating sensors are sensitive to temperature: studies of single-mode FBG sensors similar to those used in this study were reported to have a 0.013 nm /°C shift in the centre wavelength [106] with a highly linear relationship. Since these trials were conducted on different days, there were likely minor temperature fluctuations in the lab between test days. Given that the relationship between FBG centre wavelength and applied force is calculated by the slope of the linear fit line and independent of the y-intercept, these small fluctuations due to temperature have minimal effect

on measurements obtained using the FBG sensors, as long as the centre wavelength is recorded and used as the reference for any load applied thereafter.

Shift in wavelength of the FBG sensor due to strain is given by

$$\Delta\lambda_{BS} = 2\left(\frac{\Lambda\partial n_{eff}}{\partial l} + n_{eff}\frac{\partial\Lambda}{\partial l}\right) * \Delta l$$

Where  $\Delta l$  is the change in length of the FBG due to strain,  $n_{eff}$  is the effective refractive index, and  $\Lambda$  is the grating period, all inherent properties of the FBG sensor independent of temperature.

## 2.8 Limitations and conclusion

There are several limitations to the methods outlined in this chapter. First and foremost, the sensors can only measure force in one direction. Using the developed method, we are able to describe the forces acting on the anterior and posterior sides of the disc respectively. However, it should be noted that this does not fully describe the loading state of the disc. Further investigation would be needed to establish the feasibility of accurately calculating bending moments to adequately replicate measurements that can be done with a conventional 6-DOF load cell using FBG sensors in order to fully describe the entire loading state of the disc during postural loading.

FBG sensors can be sensitive to fluctuation in temperature, which was not accounted for in the sensitivity calculations. This was not of major concern for the purposes of this study, as all experiments were performed in an MR scan room with a highly controlled temperature (+/- 0.5 °C). Furthermore, the reference centre wavelength was recorded separately for each loading condition and so possible minor differences in temperature between trials had no effect as all load measurements were taken relative to the starting centre wavelength. However, if



considering extending the protocol to direct measurement of force within human joints, the effects of temperature fluctuation within the joint tissue throughout a given measurement would need to be taken into consideration. FBG sensor arrays have been reported in the literature that make use of the change in spectral bifurcation of a pair of FBGs in order to eliminate influences of temperature [111], however this would require further design and development beyond what was considered for the purposes of this study.

The cost of implementing this load measurement system was minimal beyond the acquisition of an optical interrogator and DAQ system. Generally, these two components are the most expensive components for such a system. By comparison, however, previously reported use of fibre optic technology for measurement in the MRI environment requires the implementation of the same type of optic interrogator and would come at a similar cost. Therefore, the cost of this system is comparable to similar fibre optic force sensing systems, but capable of measurements in a higher range of forces than previously reported studies.

## **Conclusion**

The first purpose of this chapter was to review past and current methods for measuring joint loads in the MRI environment. We found that while fibre optic technology has been proven to have strong potential for force measurement in the MRI environment, we found no previously reported studies where measurement systems were developed that were capable of measuring forces relevant to the intervertebral disc of over 2000 N, which are extremely relevant for biomechanical investigations of the intervertebral disc.

The second purpose of this chapter was to describe the integration of the FBG sensors into the joint loading rig setup. This was performed by using a light-curing adhesive to secure

two FBG sensors to opposite sides of a piece of hollow acrylic tubing, designed to be removable from the joint loading rig. The FBG sensors were aligned with the anterior and posterior side of the disc within the joint loading rig to provide an overall impression of the forces acting on these respective regions of the disc.

The third purpose of this chapter was to present the calibration method and results for the force measurement system. Based on these results and a comparison to accuracy of similar systems in the literature, we conclude that the system is capable of producing repeatable and reproducible results for the purposes of our study within the desired force range of 0 to 2500 N.

### **Chapter 3: Analysis of the apparent diffusion coefficient in the intact human lumbar intervertebral discs under simulated physiological loading conditions**

Morphologic and anatomic changes to the intervertebral disc as a result of degeneration are well understood, however, these methods do not distinguish changes that occur naturally due to aging from changes that might be considered pathological. The role of the disc is mainly mechanical, and so changes to the mechanics of the intervertebral disc have been studied extensively and have shown indication of clinically important degenerative changes [46], [52]–[54], [57]. While studies such as these have contributed important findings, there is currently no established method to assess mechanical function directly *in vivo*, and so a gap still exists in our understanding of the relationship between disc mechanics and symptoms.

A previous study of cadaveric lumbar specimens found ADC to be sensitive to different loading conditions and shows promise to be an effective tool for establishing altered disc mechanics in early stages of degeneration [15]. However, this was a study with a small sample size, and only considered simple axial compression of the spine; the effect of different loading conditions incorporating bending moments resulting in flexion and extension of the spine, have not yet been considered.

This chapter addresses the second and third objectives of the thesis: To develop a protocol to measure the ADC values in the disc and to use this protocol to assess the relationship between ADC and loading conditions. The work here builds on this previous study by investigating the relationship between bending moments superimposed with compressive loads on the spine and the resultant ADC measurements in the disc in addition to axial compressive loads. In order to

achieve this, an apparatus that simulates physiological loading conditions was designed and fabricated.

Outlined in this chapter is the design process for this apparatus, referred to as the ‘joint loading rig’, and the measurements acquired using this rig with cadaveric human specimens and the joint load measurement system outlined in Chapter 2. From the developed methods and obtained results, we address the third objective by presenting and discussing the relationship between ADC and loading condition.

### **3.1 Design and development of the joint loading rig**

#### **Loading conditions simulating postures of the spine**

The joint loading rig was designed to apply simulated physiologic loading conditions on the lumbar intervertebral disc. The rig was designed to apply a controlled displacement for ease of use within the MRI environment and to follow the methods used in the major motivating studies for this experiment [15] to allow for more direct comparison of results. In this study, the loading conditions being investigated were the following:

- Supine (minimal loading);
- Standing (axial compression);
- Flexion superimposed with axial compression; and
- Extension superimposed with axial compression.

The latter two conditions were chosen to best represent *in vivo* loading conditions: the rotation of the spinal column produces a bending moment on the lumbar IVD, while compressive force is generated through a combination of bodyweight and muscle activation. Previous studies have shown the importance of assessing the effect of pure bending moments on the mechanics of

the disc [112], [113]. While this type of study is important to fully understand the behaviour of the disc, the application of a pure moment is not necessarily representative of natural physiological loading conditions. Moreover, such a study requires a more complex test setup, which would be difficult and costly to achieve given the limited space in the bore of the 7 T MRI scanner. For these reasons, the joint loading rig was required to apply a compressive load to the functional spinal unit (FSU) while also creating a bending moment to simulate the flexion and extension of the spine.

### **MR compatibility**

There are several design constraints imposed on such a rig for use in an MRI environment. To ensure MR compatibility, the rig must:

- Have no electromagnetic interaction with the MR system, or vice versa;
- Cause no disruption of the magnetic field or generation of RF interference by external equipment, which can lead to image artifacts [114] [115];
- Mitigate the risk of the ‘missile effect’. *The ‘missile effect’ is the potential danger imposed by bringing ferromagnetic metals into the MR environment that can accelerate towards the magnet, becoming a dangerous projectile. Consequences include severe injuries and expensive equipment repairs [77];* and
- Fit within the dimensions of the receiver coil necessary for the scan protocol (refer to Section 3.2 Image Acquisition).

### **Material selection**

Material selection was limited based on MRI-compatibility: the two most feasible groups of materials were plastics and non-ferromagnetic metals. While non-ferromagnetic metals are often considered safe in the MR environment, their conductivity can result in eddy currents being

generated in the object by the magnetic field gradients of the scanner. In turn, this disrupts the local magnetic field, leading to image distortion [115].

Additionally, MRI-compatible metals are often much more expensive than plastics. While plastics are MRI-compatible, the chosen material must also have the hardness, stiffness, strength and other properties to suitably house the lumbar FSU and apply loads within the relevant physiological range. While many plastics were considered, Delrin® and clear cast acrylic were chosen and pursued for use in the final design. Delrin® has high compressive and tensile strength, creep resistance, and toughness compared to other plastics. Creep resistance was an important consideration, as any compressive load should solely result in the compressive strain of the FSU and not the surrounding components of the rig. Acrylic has a slightly higher but similar Young's Modulus to Delrin®, but a significantly lower cost.

### **Design requirements**

Based on these inputs, a list of need statements was created to outline the scope of the rig design.

The need statements are as follows:

- House a lumbar FSU in a fixed position for the duration of the desired MRI scan;
- Cause no electromagnetic interaction between the rig and the MR scanner, nor the MR scanner with the rig;
- Pose no potential risk to safety in the MR environment via the 'missile effect' or similar hazards;
- Fit within the receiver coil for the Bruker Biospec 70/30 7.0 Tesla MRI scanner;
- Apply compressive and bending loads to a lumbar FSU in the range of 0 to 2000 N and flexion/extension angles in the range of 0 – 15°; and

- Keep the inferior side of the FSU fixed while bending and compressive loads are applied to the superior side

The final design was made from acrylic tubing with a 5.75-inch outer diameter and 0.25-inch wall thickness (Figure 3.1). Threaded Delrin® caps were designed for either end of the acrylic tubing; the top cap housed two differential screw assemblies with a differential of 1.0 mm. allowing for fine control of the displacement applied to the FSU. The differential screws aligned with the anterior and posterior sides of the specimen that could apply an offset point load to simulate the desired loading conditions: For a standing posture, the force applied through both differential screws is equal. For flexion and extension, a greater force is applied on the anterior and posterior sides respectively, such that a bending moment about the disc's centre is created, and the spine flexes as a result.

Other techniques for applying compressive and bending loads reported in the literature were considered, such as hydraulic actuators to simulate forces generated by muscle groups [116] and tensioned cables to simulate muscular forces generating simultaneous compressive forces and bending moments [117]. Due to the size and material constraints imposed by the MRI environment, however, the offset point load was the simplest and most cost-effective method to implement for this study, and has been previously shown to be capable to apply loads that represent forces felt by the disc as a result of bodyweight and muscular forces during bending [104].

All parts were designed in SolidWorks and manufactured using precision machining tools. A rendering of the final design is provided (Figure 3.1) as well as a demonstration of the

generation of the different loading conditions (Figure 3.2); detailed drawings and bill of materials for the final design can be found in Appendix C.

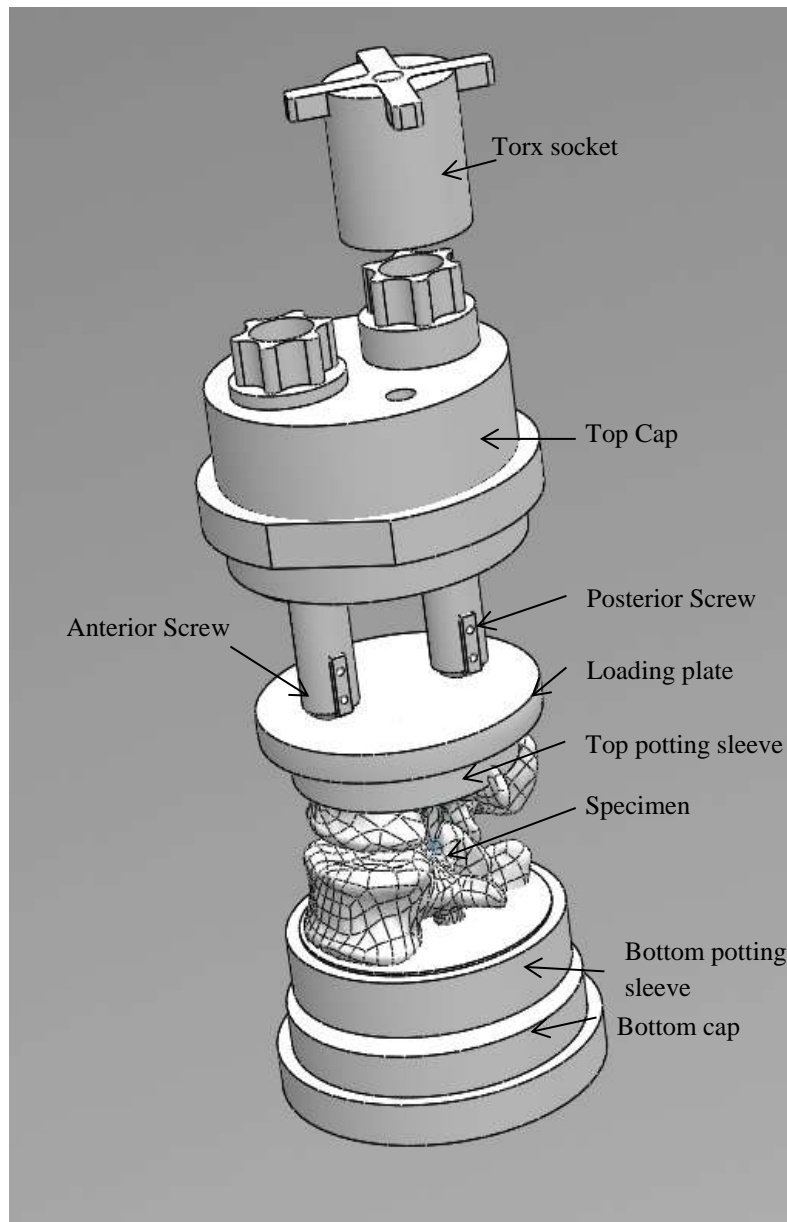


**Figure 3.1** Rendering in SolidWorks of the joint loading rig with major components labeled



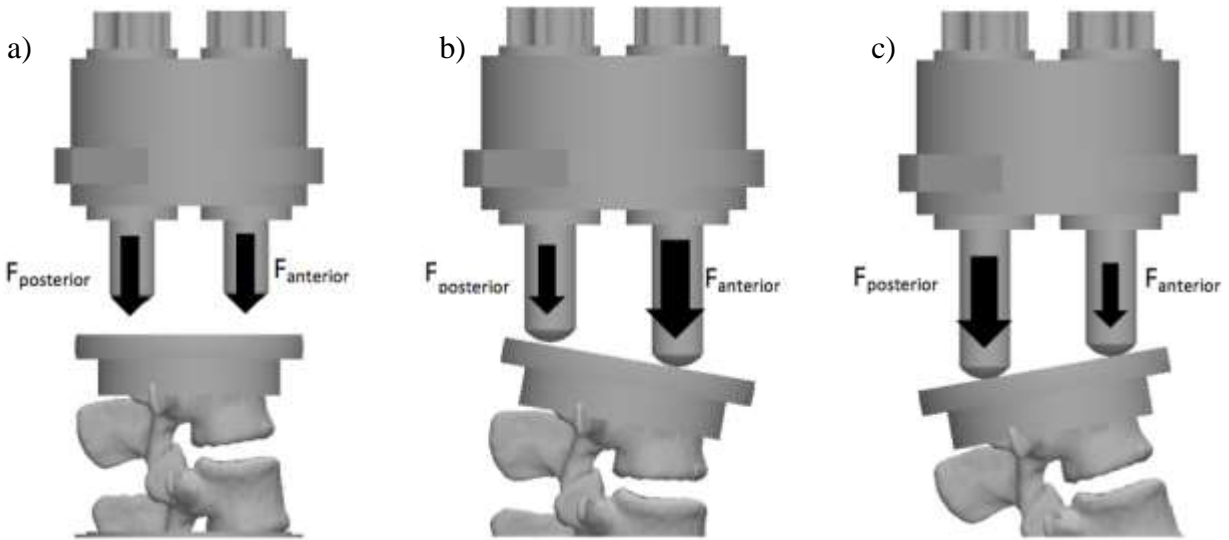


**Figure 3.2 Demonstration of the differential screws generating three different loading conditions: a) Standing (axial compression) b) flexion and c) extension**

### **3.2 Image acquisition**

For this study, all images were acquired using the Bruker Biospec 70/30 7.0 Tesla MRI Scanner at the UBC MRI Research Centre with four receiver channels and a 20 cm-diameter accessible bore. The advantage of using this scanner over typical clinical MRI scanners is the improvement of image quality and resolution that is achievable in the higher magnetic field: signal-to-noise ratio (SNR) increases proportionally to magnetic field strength. The high field strength of the 7 T also allows scan times to be significantly reduced by using a lower repetition time (TR) while still achieving adequate SNR. Soft tissues surrounding the disc can also be dissected away, thereby decreasing signal attenuation from the IVD and resulting a better SNR than would be possible for an equivalent *in vivo* experiment.



**Figure 3.3 The Bruker Biospec 70/30 7.0 Tesla MRI scanner**

Protocol development took place over the course of several sessions in order to optimize the diffusion-weighted scans of the lumbar IVD. The protocol development was conducted with significant help from Andrew Yung, an MR physicist at the UBC MRI Research Centre, with extensive experience with diffusion-weighted and anatomical reference scan sequences. We started with basic parameters for adequate diffusion-weighting signal acquisition in the IVD that are offered in a published study [15], and then went through several iterations modifying certain parameters, such as the diffusion-weighting, the echo time (TE), and repetition time (TR) and the number of directions sampled, and the number of averages.

To establish when an adequate sequence had been developed, a list of criteria was generated to define an acceptable diffusion-weighted scan for use in this study:

- A minimum slice thickness such that three slices could be taken axially through the disc tissue without slicing through the endplates;
- Adequate signal-to-noise ratio such that the boundary between the nucleus and the annulus of the disc could be identified; and

- A maximum scan time of 30 minutes to minimize effects of stress-relaxation of the cadaver specimen under load on the obtained images, as well as to maximize efficiency and minimize cost.

Through an iterative process, a diffusion-weighted scan sequence was determined (Table 3.1), which satisfied the assessment criteria above.

**Table 3.1 Summary of MR parameters for the diffusion-weighted scan protocol**

Parameter	Value
<i>General</i>	
TE	29.4 ms
TR	750 ms
Averages	1
Scan time	26 m 22 s 750 ms
<i>Geometry</i>	
Field of View (FOV)	80 x 80 mm
Matrix Size	128 x 128
In Plane Resolution	0.625 x 0.625 mm
Slice Thickness	1.5 mm
# Slices: 3	3
<i>Diffusion</i>	
Directions	6
B-values	100, 400, 700, 1000 s/mm <sup>2</sup>
Gradient duration	8 ms
Gradient Separation	15 ms

The images obtained during the protocol development were of a bovine IVD that was dissected, potted, and compressed using a compressive joint loading rig from a previous project. Dissection consisted of removing all muscle and fat from the disc being imaged and the adjacent vertebral bodies; potting was done using R1Fast Cast ® #891 casting resin. This procedure was done with a bovine specimen in order to minimize cost and complexity of obtaining and using a

human cadaver specimen, as the bovine IVD has a similar structure and size to that of a human. The specimen preparation procedure for the bovine specimen followed the same protocol used to prepare all human specimens for this study, as described in Section 3.3.

The developed scan sequence was verified by comparing the absolute values of the central slice obtained from the generated ADC map to those reported by Alkalay et al [15]. The scans were segmented in a 3D slicer into the NP and AF respectively, and the ADC value was taken as the average across the entire region. The ADC values in the nucleus were found to be significantly higher than in the annulus, as expected. Furthermore, the absolute value was found to be in the range of  $13.8 - 14.5 [10^{-4} \text{ mm}^2/\text{s}]$  in the NP and  $12.2 - 13.0 [10^{-4} \text{ mm}^2/\text{s}]$  in the AF under various compressive loads. Average ADC measurements in the nucleus were  $13.0 [10^{-4} \text{ mm}^2/\text{s}]$  in the NP and  $10.5 [10^{-4} \text{ mm}^2/\text{s}]$  in the AF in the study by Alkalay et al [15]. These similar results served as evidence that the sequence produced adequate diffusion weighting and resultant ADC maps in the desired regions of the disc, and so testing went ahead using this developed scan sequence.

A volume RF receiver coil with inner diameter of 15 cm was used, which housed the joint loading rig with minimal space between them. This was done in order to minimize the amount of empty space within the coil, as free-air generates noise but no signal, in order to achieve a strong signal-to-noise ratio (SNR).

During each testing session, the acquisition plane was determined by adjusting the axis of the slice until it was parallel with the adjacent vertebral bodies (Figure 3.4). The dashed lines represent the vertebral body reference lines defining the boundary between the vertebrae and the disc, and the solid lines show the corresponding axial slices. The three slices represent the slices acquired during the DWI scan; a high-resolution T2-weighted scan was collected immediately

after the DWI scan, with the same slice axis as the centre DWI scan slice. This was done for each loading condition.

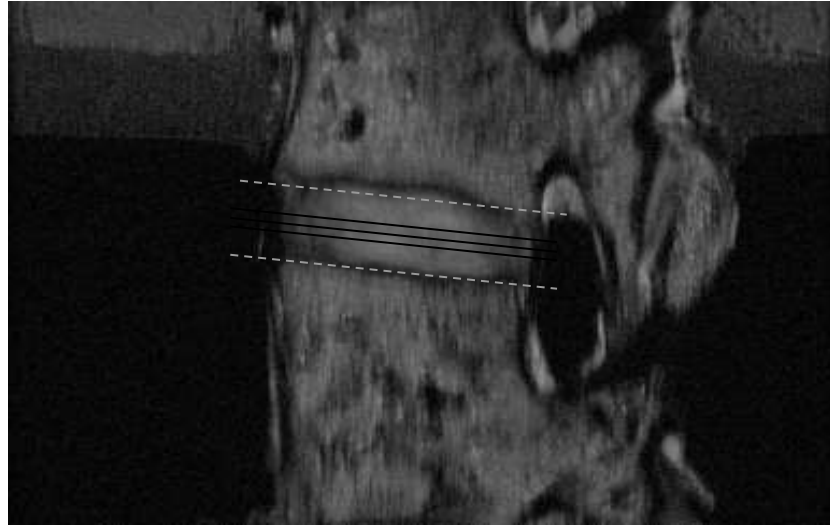


**Figure 3.4 Slice orientation relative to the vertebral bodies for the axial diffusion-weighted scan**

### **3.3 Test protocol**

#### **Specimen preparation**

Three previously frozen human cadaveric lumbar specimens were used for testing in the joint loading rig. Prior to preparation, spines were radiographed and evaluated by Shun Yamamoto, a consulting orthopaedic surgeon at ICORD, to exclude bone pathology and categorize levels of disc degeneration using the methods described by Wilke et al [118]. Specimens were thawed for 36 hours in a refrigeration unit maintained at 4 degrees Celsius in advance of preparation to ensure that they were completely thawed.

One day before testing in the MRI scanner, fat and muscle surrounding the disc and adjacent vertebral bodies were completely resected from the lumbar specimens using a scalpel.

Small amounts of remaining soft tissue along the vertebral bodies were removed with a scraper. The discs adjacent to the lumbar disc that was to be imaged were transversely sectioned in order to isolate the desired functional spinal unit. Precautions were taken during the dissection as to not disrupt the IVD or the surrounding ligaments, excluding the intertransverse ligament, which was difficult to isolate as it often blends with the intertransverse muscles. Further, the role of the intertransverse ligament is mainly in facilitating lateral bending, which was not of importance in this study. Specimens were determined to have only ‘mild’ levels of degeneration at the vertebral level (Table 3.2).

**Table 3.2 Specimen and donor information**

<i>Donor ID</i>	<i>Level</i>	<i>Sex</i>	<i>Age</i>	<i>Degeneration</i>	<i>Notes</i>
H1327	L1-L2	F	58	Mild	-
H1338	L4-L5	Unknown	Unknown	Mild	Data regarding donor information was unavailable
H1144	L3-L4	F	79	Mild	L4-L5 FSU intended but damage to L5 vertebrae was noticed during dissection

FSUs were rigidly fixed in hollow cylindrical acrylic potting sleeves filled with R1Fast Cast ® #891 casting resin. Care was taken to ensure no soft tissue or residue remained around the endplates and vertebral bodies at each end of the FSU, as this was found to hinder the effectiveness of the potting procedure during pilot testing. The caudal end of the FSU was fixed in a potting sleeve with a 5-inch diameter, designed to slide-fit into the outer housing of the joint loading rig. The cranial end of the FSU was fixed in a 4-inch potting sleeve, designed to interface with the loading plate of the joint loading rig (Figure 3.5). The FSU was aligned such that the IVD lay parallel to the flat surface of the potting cups in the transverse plane. Once potted, the FSU was wrapped in saline soaked gauze and stored in a refrigerator at 4 degrees Celsius overnight.

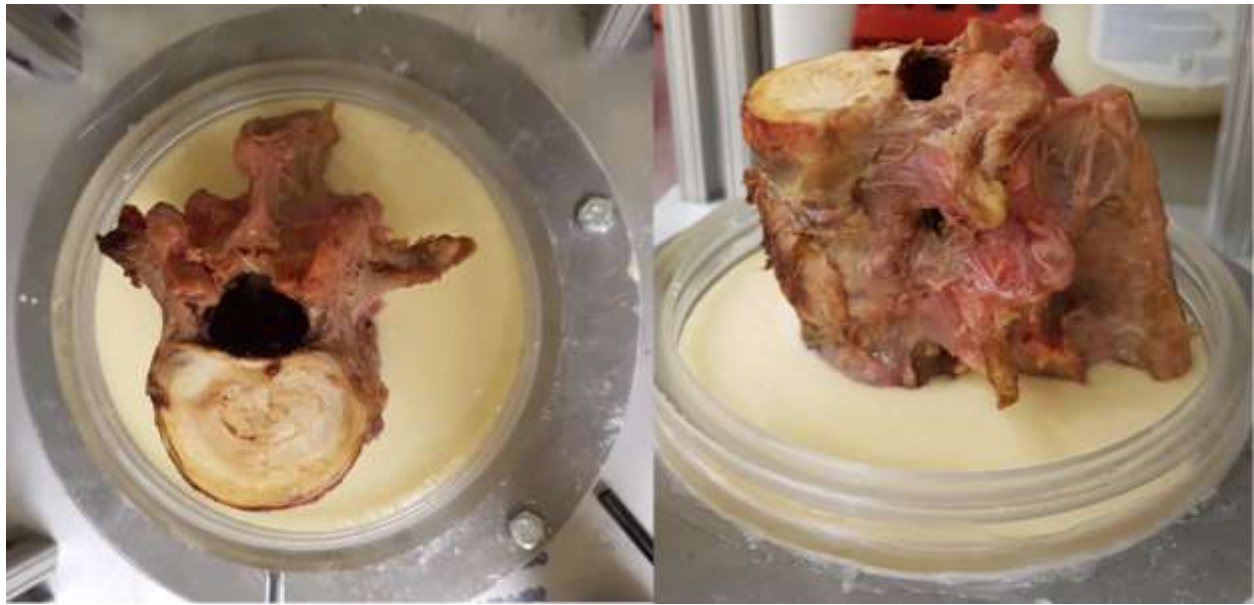


**Figure 3.5 Top view (left) and sagittal view (right) of lumbar FSU with caudal side potted**

### **Experimental procedure**

The specimen was conditioned through a pre-load protocol outside of the MR scan room. For preloading, the specimen underwent 10 cycles of compressive loading; the first five cycles were axial compressive loading, and the next five consisted of a combination of compression with both flexion and extension; equal load was first applied through each differential screw of the rig, and was then offset anteriorly followed by posteriorly, simulating a movement of the disc through its range of motion in the anterior-posterior direction. Load was applied manually for each cycle and fell within the range of 400 – 700 N by checking the readings of the FBG sensors, and was reduced to zero at the end of each cycle. For the latter five cycles, the load was held within a similar range but offset to the anterior side followed by the posterior side. The simulated physiological loading condition was then applied once the joint loading rig housing the specimen was brought into the MRI scan room. Specimens were placed within the large receiver coil using

a small amount of foam placed around the edges of the joint rig ensure a tight fit to prevent movement during the scanning sequence. Each specimen was scanned in the order of the following loading conditions: supine, flexion and extension, and standing. The scan sequence described in Section 3.2 was run for each loading condition, for each specimen.

### **Force measurement**

The force measurement system (outlined in Chapter 2) was set up in the bore of the 7 T MRI scanner in conjunction with the joint loading rig (Figure 3.6). The two FBG sensors were aligned with the anterior and posterior sides of the FSU, respectively. The free end of the fibre optic cables connected to the FBG sensors were fed through the access port to the MR scan room and attached to the DAQ system, which remained in the control room for the duration of the experiments. Force measurements began recording immediately before the loading condition was applied to the FSU, and continued to record at a rate of 1 Hz for the duration of the scan. The force vs. time graph was then plotted for each loading condition in order to verify the peak force acting on the disc and observe the stress-relaxation of the disc tissue over the duration of the scan time.



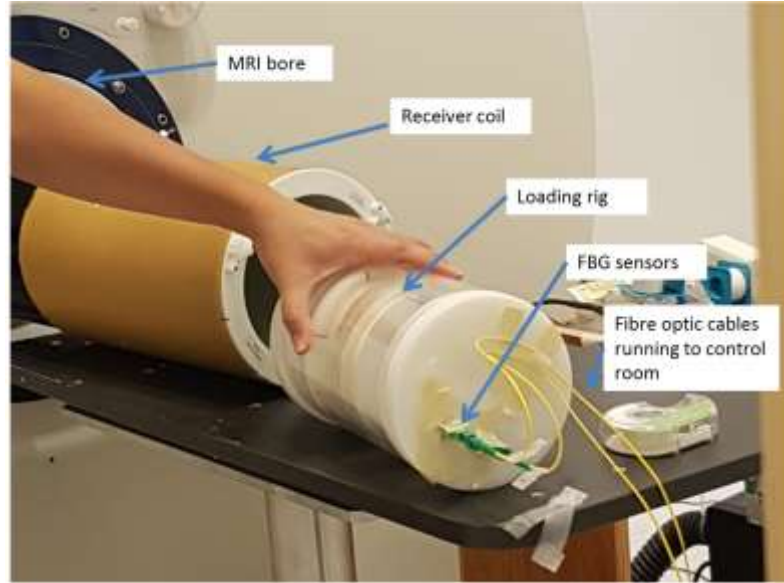


**Figure 3.6 Test setup in the MR scan room**

*The FBG sensors are run through the bottom of the loading rig, which is placed in the receiver coil, which is then placed in the MRI bore*

From the peak force, approximate calculations were done to assess the range of bending moments on the disc. Moments were calculated using the methods derived from a study that quantified the bending moment acting on cadaveric lumbar discs under compressive loads superimposed with bending moments, very similar to the test setup in this study [119]. Bending moment was approximated as

$$M = F_{peak} \sin(\theta) \sqrt{(d^2 + h^2)}$$

where:  $\theta$  is the angle of rotation;  $d$  is the distance from the disc centre (C) to the offset applied force;  $h$  is the vertical distance between the disc centre and the differential screw (Figure 3.7). For each bending calculation,  $\theta$  and  $h$  were calculated from measurements using an open source image processing software (ImageJ, Version 2.0.0) from photos taken during setup of each loading condition;  $d$  given by the offset distance of the differential screw from the centre of the joint loading rig (drawing no. 001, Appendix C).

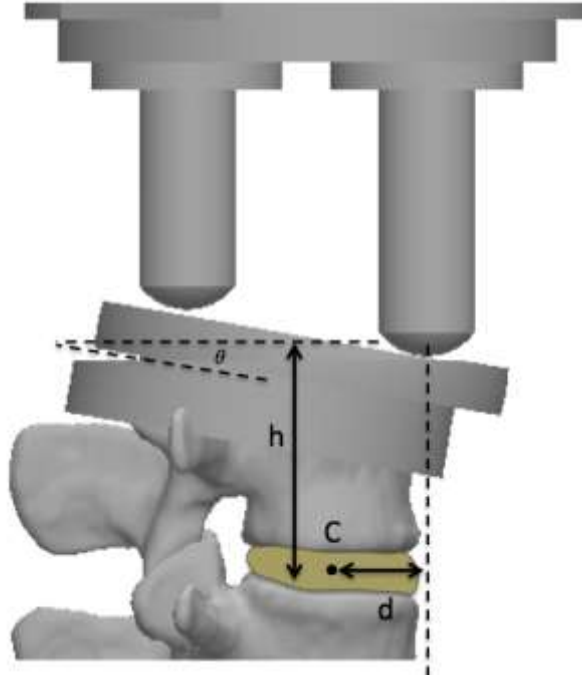


**Figure 3.7 Relevant parameters for bending moment approximation**

### **3.4 Image processing**

#### **Nucleus-annulus boundary definition**

A MATLAB script was developed to define boundary points to aid in the segmentation process. The NP has a structured network of varying lengths of fibres that integrate with fibres of the inner AF. Because of this transition region, visual identification of the boundary is difficult and very susceptible to high variability [120]. Therefore, a quantitative method was implemented to minimize variability in the segmentation process for all images.

The ADC value in the AF is significantly lower than in the NP due to the lower water content and complex collagen fibre network which limits diffusion [85], [121]. The signal is lowest at the outer boundary of the AF, and steadily rises through the inner AF as the region transitions over into the NP. Finally, the signal intensity is highest through the centre of the NP,

creating a relatively Gaussian distribution when looking at a single line passing through the centre of the disc (Figure 3.8).

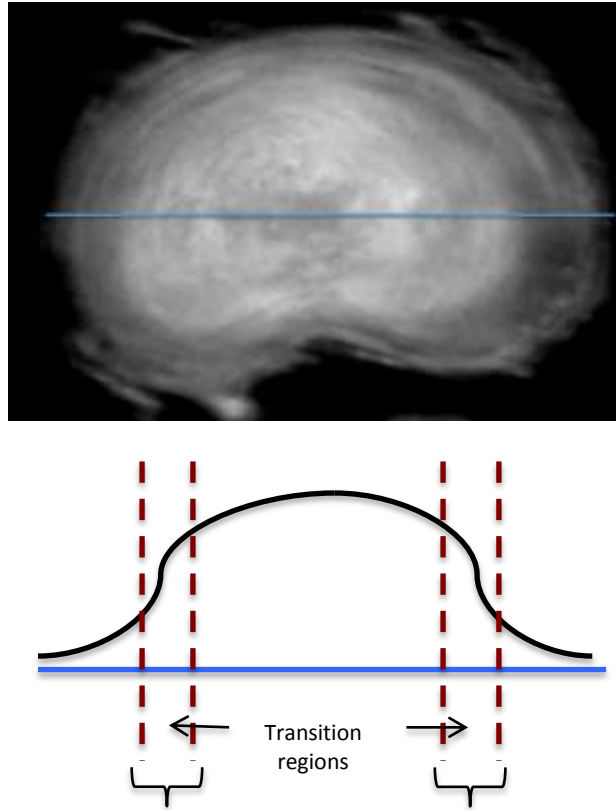


**Figure 3.8 Demonstration of line drawn through disc centre (top) and corresponding signal intensity profile, highlighting transition regions (bottom)**

The MATLAB script defined the NP-AF boundary by drawing several lines through the disc centre, fitting a normal distribution to each line, and calculating the full width at half maximum (FWHM), taken as the relationship

$$FWHM = \frac{1}{\sigma\sqrt{2\pi}} \exp\left[-\frac{(x - x_0)^2}{2\sigma^2}\right]$$

where  $\sigma$  is the standard deviation and  $x_0$  is the expected value

The resulting boundary points were then transformed to the corresponding coordinate system in 3D Slicer (Version 4.6.2, Boston, MA), where the rest of the segmentation process was performed (Figure 3.9).

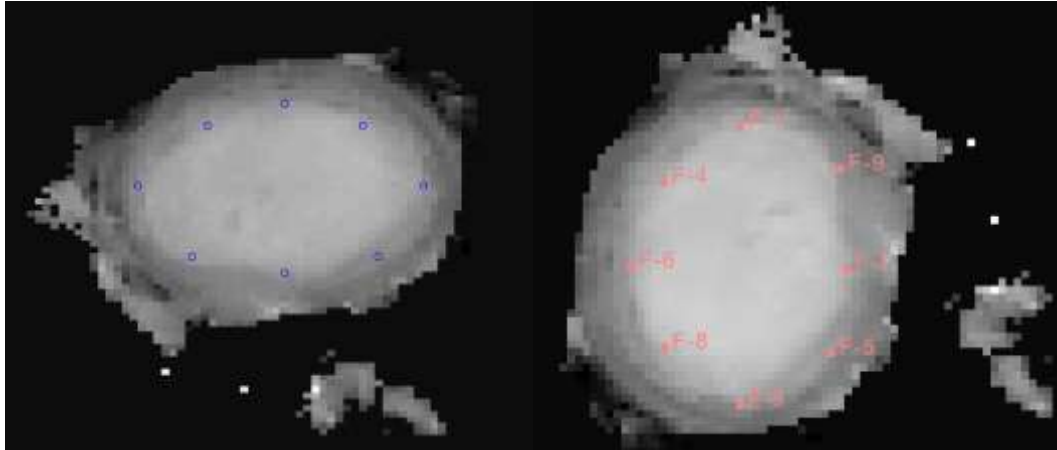


**Figure 3.9 MATLAB generated boundary points (left) and corresponding transformed fiducial markers in 3D slicer (right) defining boundary between nucleus and annulus**

### **Annulus segmentation**

Apparent diffusion coefficient maps were generated using a custom MATLAB script that calculated the ADC value for each voxel from the raw data files from the MR scanner (MATLAB Mathworks, Natick, MA). This was repeated for every loading condition for each specimen. The resultant ADC maps were then imported into image processing software (3D Slicer, version 4.6.2, Boston, MA). Segmentation was performed on the central transverse slice, aligned with the geometric centre of the disc.

The boundary between the nucleus pulposus and annulus fibrosus was defined using the newly developed method. The AF was further segmented by fitting an ellipse to the shape of the disc and then divided into equal segments (Figure 3.10) using lines calculated by the following equations:

$$Y = \frac{b}{a} * \tan(\theta_k) * X$$

Where:  $\theta_k = \frac{k\pi}{2n}, k = 1, \dots, 11;$

$b$  is half the anterior-posterior width of the disc; and

$a$  is half the medial-lateral length of the disc.

Manual adjustments were then made to the lines dividing each segment if areas were not consistent due to the additional constraint imposed by the minimum width from the nucleus-outer annulus boundary. The AF segments were then categorized into anterior, lateral, and posterior regions (Figure 3.10 and Table 3.3).

**Table 3.3 The defined anatomic regions and their corresponding labels and descriptions**

Region	Label	Description
Anterior	A	Anterior-centre AF
Anterior-1	A-1	Anterior-medial, (non-central) AF
Anterior-2	A-2	Anterior-lateral AF
Lateral	L	Lateral AF
Posterior-1	P-2	Posterior-lateral AF
Posterior-2	P-1	Posterior-medial (non-central) AF
Posterior	P	Posterior-centre AF
Nucleus Pulposus	NP	Entire NP

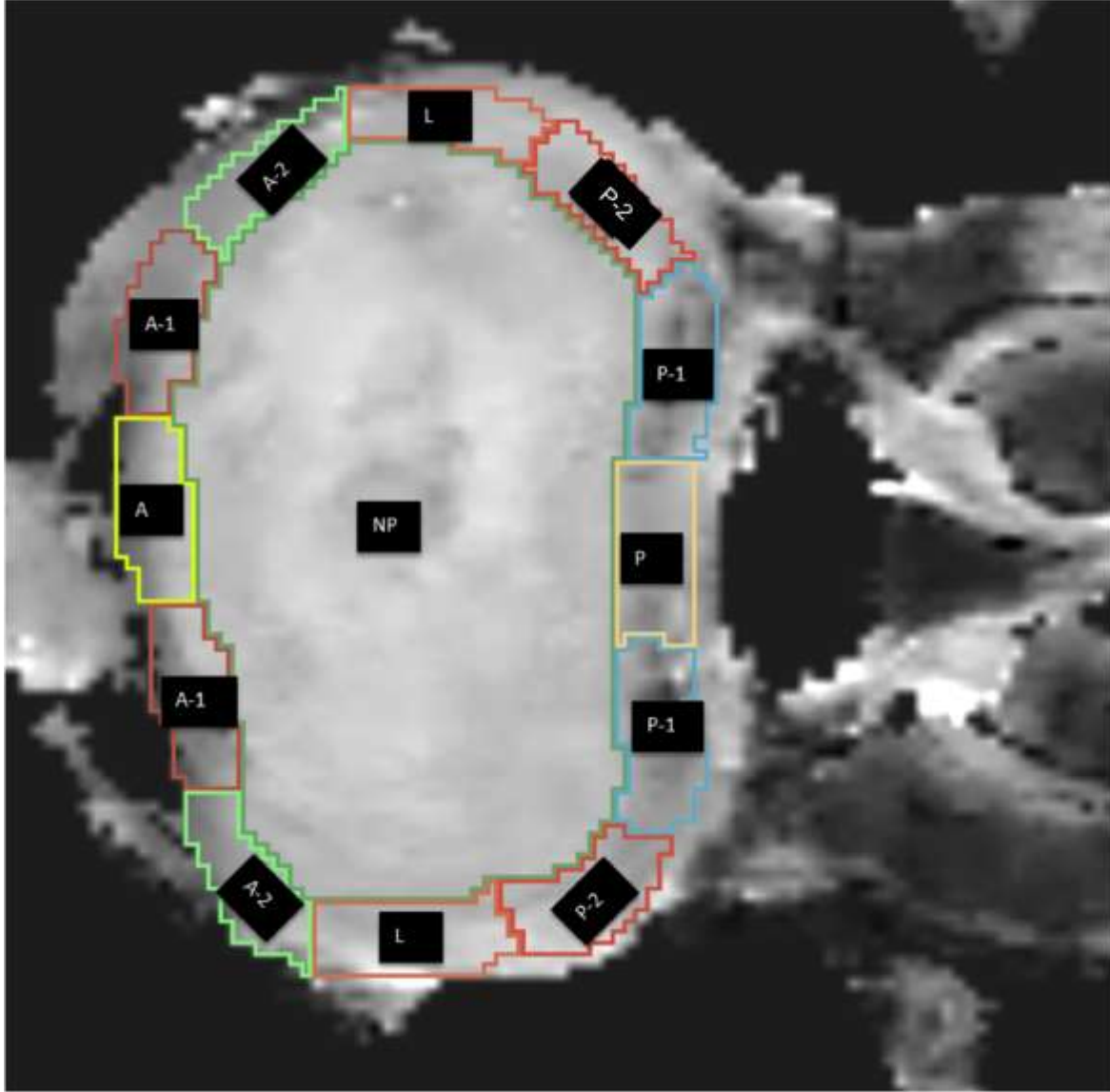


**Figure 3.10 Segmentation in Slicer of specimen H1338 showing the defined anatomic regions**

We found mean values by taking the average ADC from each voxel within each defined anatomic region. Standard deviations were calculated from the distribution of ADC values within a given region using

$$\sigma = \sqrt{\frac{\sum (ADC_i - \overline{ADC})^2}{n}}$$

Where  $ADC_i$  is the ADC value of a given voxel,  $ADC$  is the mean ADC value, and  $n$  is the number of voxels.

### **Statistical analysis**

Nonparametric analysis was performed since normality in the data could not be assumed due to the small sample size ( $n = 3$ ). To test the effect of disc region (NP vs. AF) on the ADC for each loading condition, the Mann Whitney U-test was used as the nonparametric equivalent to the t-test for independent samples. Additionally, Friedman test was used to compare the segmented regions of the AF to determine if ADC changed significantly from the anterior to posterior side in both flexion and extension loading conditions.

The paired samples Sign test was used as the non-parametric equivalent to the dependent t-test to assess the effect of loading condition on the ADC within each defined anatomic region. Repeated measures were used to examine the magnitude of the difference in ADC between each loading condition. For each of these tests, significance was set at  $p \leq 0.05$ .

## **3.5 Results**

### **Force Measurements**

The maximum forces measured in the FBGs aligned with the anterior and posterior sides of the specimen ranged from 1100 – 1950 N (Figure 3.11 and Figure 3.12). Stress-relaxation was observed for all three specimens, with larger initial relaxation for larger applied loads. The stress-relaxation plots for all specimens and loading conditions can be found in Appendix D. From the measured peak forces, approximate bending moments were calculated (Table 3.4). Moments ranged from 10 – 19 Nm for flexion and 8 – 9 Nm for extension .

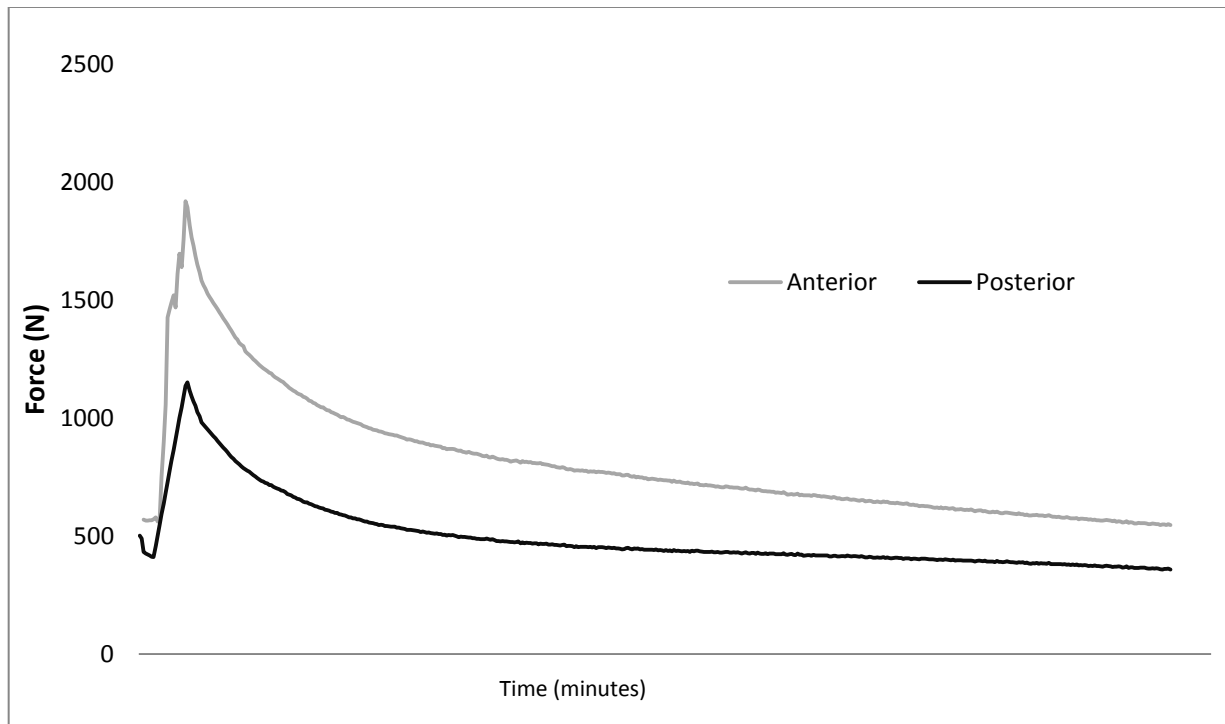


Figure 3.11 Stress relaxation plot for specimen H1144 during flexion loading

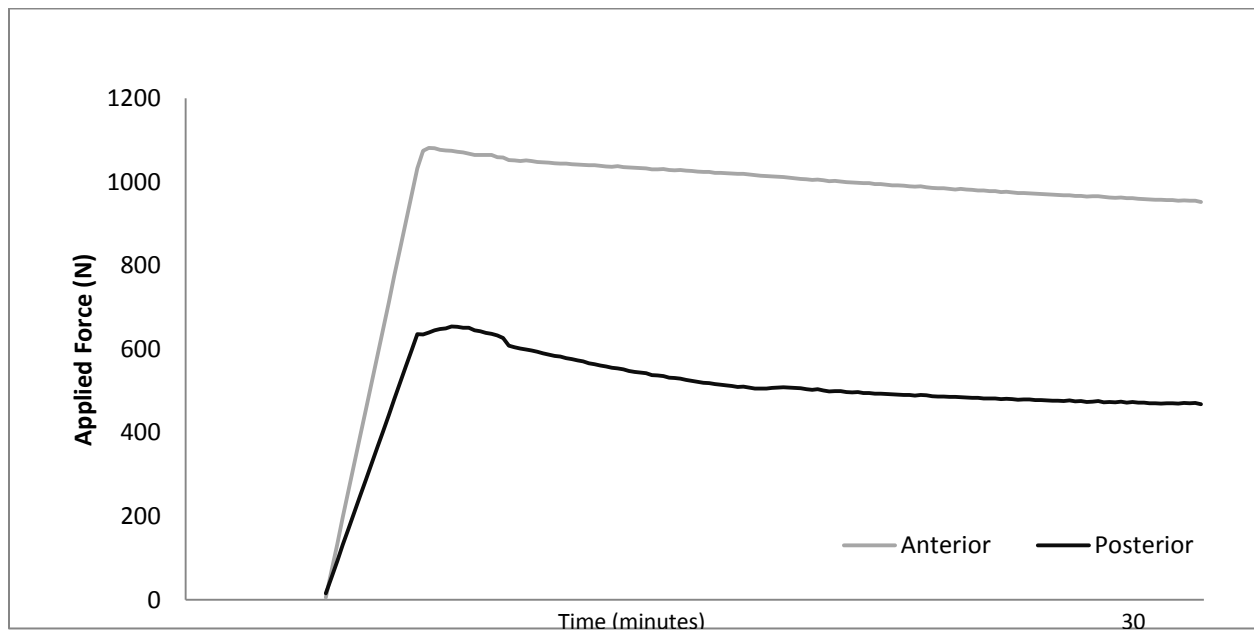


Figure 3.12 Stress relaxation plot for specimen H1338 during flexion loading



**Table 3.4 Bending moments approximated from peak force data**

Specimen	Bending moment [Nm]	
	Flexion	Extension
H1144	13.8	8
H1338	10	9
H1327	19	N/A*

\*Force data could not be collected for specimen H1327 due to damaged FBG cables – refer to Appendix D

### Effect of disc region

In the three lumbar FSUs tested in this study, we found larger ADC values in the NP than in the AF for all loading conditions ( $p = 0.001$ ) (Table 3.5). We found no significant change in ADC between the segmented regions of the AF tissue in either state of bending (flexion  $p = 0.241$ ; extension  $p = 0.056$ ).

**Table 3.5 ADC values in different anatomic regions of the disc**

		ADC [ $10^{-4}$ mm <sup>2</sup> /s]							
		NP	AF						
		-	P	P-1	P-2	L	A-2	A-1	A
Loading Condition	Unloaded	10.23	8.81	8.60	9.67	9.74	8.50	7.80	7.30
		11.32	11.07	10.83	10.91	10.52	10.72	10.24	10.18
		11.78	9.84	9.85	10.39	11.40	9.84	9.88	9.85
	Flexion	11.03	9.01	8.99	10.56	10.51	8.17	7.51	7.39
		12.16	10.45	11.24	10.69	10.92	11.58	11.21	10.82
		12.66	10.62	10.41	10.92	11.03	10.15	10.47	11.11
	Extension	11.53	9.85	9.39	10.63	10.93	8.76	7.83	7.93
		12.84	12.75	12.17	12.13	11.78	12.31	11.65	11.46
		12.73	11.12	10.98	10.88	10.53	9.98	9.53	10.06
	Standing	12.51	10.42	9.20	11.56	11.74	9.74	8.90	8.93
		13.58	13.17	12.61	12.30	12.00	12.43	11.71	11.58
		11.53	10.04	9.52	10.14	9.67	9.41	9.59	10.11

## Effect of loading condition

We found no significant difference in ADC values between any loading conditions (supine, standing, flexion, extension) in either the NP or any of the segmented regions of the AF (Table 3.6). Significance values ranged from  $p = 0.109$  to  $p = 1$ .

**Table 3.6 Significance values between different postural loading conditions in the segmented regions of the disc.**

Region	Standing - Supine	Flexion - Supine	Extension - Supine	Flexion - Standing	Extension - Standing	Extension - Flexion
Nucleus	0.285	0.109	0.109	0.285	1	0.109
Posterior	0.109	0.593	0.109	0.285	1	0.109
Posterior-1	0.285	0.109	0.109	0.593	0.593	0.109
Posterior-2	0.285	0.285	0.109	0.285	0.593	0.285
Lateral	0.593	0.285	0.285	1	1	0.593
Anterior-2	0.285	0.593	0.109	0.285	0.593	0.285
Anterior-1	0.285	0.285	0.593	0.593	0.109	1
Anterior	0.109	0.109	0.109	0.593	0.109	1

## 3.6 Discussion

### Force measurement

For these experiments, we aimed to simulate four relevant physiological loading conditions acting on the IVD for the duration of the MRI scan time: supine, standing, flexion, and extension. We found that the loading conditions used here match previously reported values for applied force, flexion/extension angle, and bending moment for the relevant postures.

Peak forces recorded by the FBGs during these loading conditions simulating spinal postures fell within the range of 800 – 1950 N, which align with previously reported measurements of forces acting on the disc for these postures [30], [33], [34], [103], [110]. The

stress-relaxation observed during the 30-minute scan time for a constant displacement match previous studies on the viscoelastic response of the intervertebral disc [23]. We also observed a steeper initial drop in force for the higher peak force values, consistent with previous findings [122], [123].

We also note that the presence of the posterior elements play a role in load transfer through the FSU. In the young healthy disc, the neural arch has been found to transfer approximately 20% of load, which can increase up to 50% in older specimens over 70 years of age [58]. While each specimen was assessed to have only mild levels of degeneration, the ages of the specimens was limited to older adults and so load transfer through the neural arch may have been higher in certain specimens. In the current setup, the posterior force measurement was unable to distinguish load transferred through the AF tissue from that of the neural arch.

Additionally, due to the need to move between the MR scan room and control room to control the LabView VI program which recorded FBG wavelength, several trials had the force begin measuring after an initial compressive force had already been applied to the specimen. This was a result of when it was practically feasible to leave the MR scan room to initiate the recording of the force from the control room; in reality, each specimen started with an initial applied force of 0 N and then a controlled displacement was applied until the desired peak force was reached.

We approximated bending moments to fall within the range of 8 – 19 Nm for a corresponding range of flexion/extension angle of 5.8 – 14.4°, both of which align closely with previous studies: A study of 42 lumbar cadaver FSUs found the flexion angle at the elastic limit to be 5.3 - 12.0°, under combined bending and compressive loading in the ranges of 16 – 100 Nm and 500 – 2000 N, respectively [119]. The bending moments approximated for this study are

closest to the low end reported in this study. This is likely a result of the shorter moment arm, as the offset distance,  $d$ , for our setup was 1.5 inches (31.75 mm) while this previous study increased the offset distance of the applied force up to 60 mm, for the same range of forces. A limitation with this moment approximation that should be noted is the use of FBG-measured peak force as the force applied by the differential screw. In reality, the FBG sensors measures the force on the anterior posterior sides of the bottom cap, and is not a direct measurement of the force generated by the differential screw on the loading plate. However, when combining this approximated moment range with the measured force range and flexion/extension angles, we believe the joint loading rig simulates the relevant postures (supine, standing, flexion, extension) to a reasonable approximation for an exploratory study.

### **ADC measurement**

The main goal of this thesis was to establish how ADC changes as a result of disc region and loading condition. To achieve this, a protocol to measure ADC in the IVD on the 7 T MR scanner was developed. Through an iterative process, we established a protocol that allowed us to measure ADC values in the IVD of three human lumbar cadaveric specimens in four physiologically relevant loading conditions (supine, standing, flexion, and extension).

We found ADC values to be higher in the NP than in the AF ( $p = 0.001$ ) a finding consistent with several other measurements of ADC in these disc regions [15], [85], [93], [94]. We were surprised to find no difference in ADC values in the segmented regions of the AF tissue for each given loading state. We expected to see the lowest ADC values in the central anterior and posterior regions in flexion and extension, respectively, while these regions experienced large compressive strains. Rather, we found no significant change in ADC in any region of the

disc between different loading conditions, while statistically significant decrease in ADC with increasing load was previously reported [15].

We believe our results differ from these previous results because the relationship between ADC may not correlate as closely with compressive load as previously reported. We note that our study had a small sample size ( $n = 3$ ) and so the power of our statistical analysis is limited. While this previous study reported significance, their study also contained a small sample size ( $n = 5$ ) and observed high variability; in both the NP and the AF, two of the five samples saw either no change in ADC or an increase in ADC with compressive load, however the overall trend across five samples was a negative correlation of ADC and compressive load. These results, when combined with the lack of correlation in the present study, suggest that the relationship between ADC and compressive load is not as significant as previously reported [15].

Moreover, this previous study measured ADC changes in the AF under compressive load, but did not consider the mechanics of the resultant strain in the tissue. We believe changes in ADC as a result of compressive load are likely a result of strain induced in the tissue, altering the diffusion pathways of water contained within the disc. However, compressive load of a neutral posture, the posterior annulus fibrosus has been shown to be have the largest tensile strains felt in the disc, while the anterior and lateral anterior annulus tissues experienced large compressive strains [124]. We performed additional tests to better establish the relationship between ADC measurements and compressive strain in the AF tissue, the results of which are presented in more detail in Chapter 4: of this thesis.

In evaluating the results of this study, there are several limitations that must be considered. Firstly, the sample size is small and could have missed relationships that may have shown significance with a much larger study. Additionally, the use of cadaveric specimens does

not account for factors such as muscle activation, and simply cannot completely capture the mechanical environment of the disc *in vivo*. Further, diffusion affects may be moderately amplified *in vivo* as a result of metabolic effects and nutrient transport from nearby blood vessels. We believe this effect may be small, however, since the tissue is avascular and there is limited metabolic activity relative to other tissues in the body. The age range of our specimens also could have affected the measurements, as ADC has been shown to correlate with age, and in this study we only used specimens from a relatively advanced age range (58 to 79 years of age).

The scan time for the diffusion sequence is another limiting factor in this study. Diffusion weighted sequences are generally long relative to other MRI techniques, which likely affected the results due to the observed stress-relaxation of the tissue over the duration of the scan. This relaxation may have affected the diffusion of free water within the tissue that we would expect to be restricted as a result of a compressive force. In future, it would be beneficial to conduct similar testing applying a constant load (creep) instead a constant displacement (stress-relaxation) as done in this study, and to compare the results.

## **Chapter 4: Analysis of the apparent diffusion coefficient under compressive strain in the annulus fibrosus**

This chapter introduces the experiment that expands on the findings presented in Chapter 3, that further addresses the third objective of this thesis: To determine the relationship between ADC values and loading conditions, simulating relevant postures (supine, upright standing, flexion, and extension) to both healthy and degenerated disc.

For this part of the study, we aimed to deepen our understanding of the relationship between ADC measurements and loading conditions simulating postures of the spine by directly assessing the relationship between ADC and compressive strain, a comparison which was not considered in previous similar work [15]. The need to establish this relationship was motivated by previous evidence that both compressive and tensile strains are experienced by the AF tissue during compressive loading [124]. To address this, we created a more controlled environment, using isolated samples of AF tissue instead of entire FSUs, which allowed us to apply a known and measurable compressive strain to the tissue. We then used this to accurately measure the change to the average ADC value within the disc tissue as a function of applied strain; we hypothesized that there will be a concordant decrease in the average ADC value within the tissue. We then predicted that these results could be used as a tool to interpret the results from Chapter 3 and also be applied in future studies to further investigate the relationship between disc mechanical properties and the associated MR parameters.

This chapter introduces the development and fabrication of the loading apparatus for applying axial compressive strain, the methods for developing a modified image acquisition and processing for this secondary experiment, and finally presents and discusses the results regarding

the relationship between ADC and compressive strain in the annulus fibrosus of the lumbar intervertebral disc.

#### **4.1 Loading device design**

A device was designed that was able to apply a controlled, compressive strain to samples of tissue from the annulus fibrosus of the lumbar intervertebral disc. The requirements for the apparatus were as follows:

- House a section of annulus disc tissue with cross-sectional area of  $5 \times 10$  ( $w \times L$ ) mm and a height in the range of 2 – 6 mm;
- Position the tissue sample within the isocentre of the MRI scanner;
- Apply an axial force resulting in compressive strain of the tissue;
- Prevent any bulging or movement of the disc tissue except in the direction of the applied load such that a pure axial compressive strain is felt by the tissue;
- Hold the applied strain for the duration of the scan sequence (~26 minutes); and
- Have no interaction with the magnetic field of the MRI scan room.

The dimensions of the tissue sample were determined from the segmented images of the previously tested specimens. The minimum annulus width and length as measured from the segmented specimens in Chapter 3 were taken as the critical dimensions for the apparatus, such that no dissected tissue sample would be smaller than the housing, which could allow for bulging or expansion of the tissue.

The design was developed for fabrication via rapid prototyping in order to minimize cost and development time. A model of the apparatus was developed in SolidWorks, and manufactured via fused filament fabrication (Ultimaker 2+, Geldermalsen, Netherlands). All threaded holes



were manually tapped after the print was complete (Figure 4.1). Refer to Appendix F for further design details.

The tissue was housed within an assembly comprised of three components: a 10 cc syringe, a tissue mount, and a porous plunger. The tissue mount and plunger were designed to hold the tissue sample in the desired orientation, and tolerance to slide-fit in the 10 cc syringe for easy alignment of the two pieces within the syringe. This design was chosen after investigating concerns with sterility: it has previously been shown that 3D-printing methods for PLA plastic can produce functionally sterile parts [125]. However, re-sterilization of these components after coming in contact with human tissue has shown higher rates of contamination [125]. Therefore, in order to ensure sterility of materials between trials, these two components that came into contact with the human tissue samples were designed to be disposable pieces, and were replaced between subsequent trials in the final design.

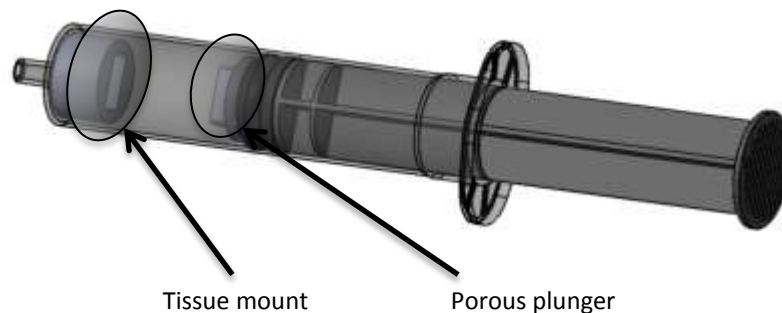


**Figure 4.1 Rendering of the tissue mounting assembly**

On the main body of the apparatus, the arches were dimensioned to slide fit into the MRI bore, with two set screws on either side to prevent movement of the apparatus once positioned correctly within the MRI (Figure 4.2). Because visibility within the MRI bore is limited, the dowels protruding from the body were designed to contact the outer edges of the receiver coil when the tissue sample is in the isocentre of the MRI bore. They act to prevent further insertion of the apparatus into the bore, thus ensuring proper alignment of the device within the receiver

coil; the distance from the edge of the receiver coil to the isocentre of the MRI was 37 mm. The flanges of a 10 cc syringe slide into the main body of the apparatus to hold the specimen at a distance of 40 mm from the lowest point of the bore MRI in the direction of the centre-point. These two dimensions were critical for alignment of the tissue sample at the isocentre of the bore, as measured during pilot testing.

A custom Allen key was designed and fabricated for use with the set screws on the curved surfaces of the device (Figure 4.3 and Appendix F.2); conventional Allen keys are typically made from ferrous metals, which cannot be used inside the MRI bore. Furthermore, the limited space and visibility of the set screws once the device was placed within the bore made the positioning of conventional Allen keys very difficult; the custom Allen key helped to address this issue. A threaded hole is centred on the back side of the body of the device such that an M8 nylon screw can be inserted to apply an axial displacement to the tissue sample via the plunger of the syringe.

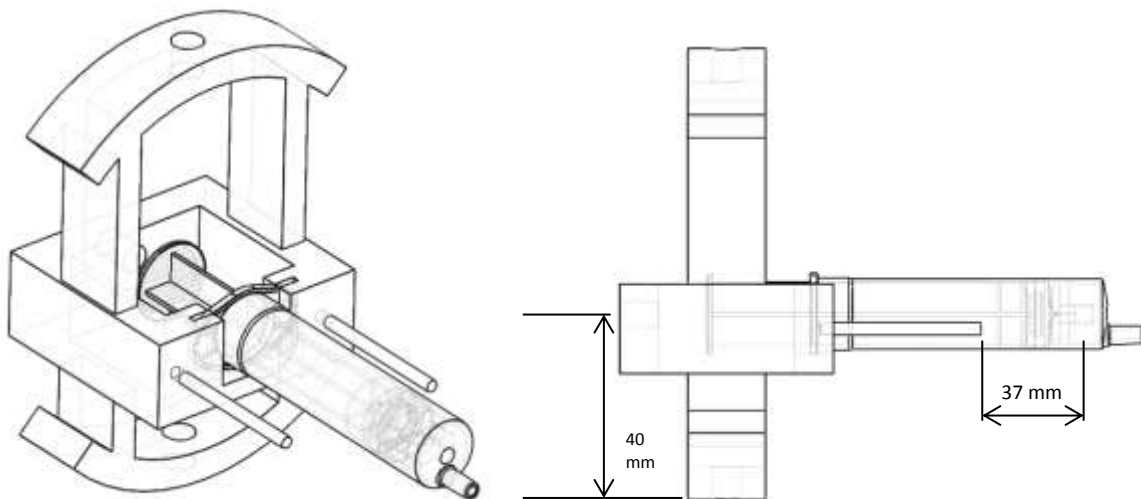


**Figure 4.2 Rendering of loading device: Isometric view (left) and side view (right) labeling dimensions required for centering of the device within the isocentre of the MRI bore**



**Figure 4.3 Rendering of the custom Allen key used with the loading apparatus**

## **4.2 Test protocol**

### **Image acquisition**

Modifications were made to the imaging sequence outlined in Chapter 3 on the Bruker Biospec 70/30 7.0 Tesla MRI scanner for acquiring images of annulus tissue samples. The same methods were followed for protocol development, but a modified set of criteria was used for determining an adequate sequence. The criteria for the image acquisition for this part of the study were as follows:

- A minimum slice thickness such that three slices could be taken axially through the disc tissue sample;
- Adequate signal-to-noise ratio (SNR) such that the individual lamellar layers could be identified; and
- Consistency with the imaging protocol used in Chapter 3, defined for the purposes of this study as identical diffusion parameters and changes only to the geometric and general parameters to obtain the required SNR for the reduced field of view.

The parameters for the final image sequence were very similar to the protocol developed in Chapter 3, with the biggest changes to the FOV and matrix size (Table 4.1). The protocol development was an iterative process imaging a section of bovine annulus disc tissue obtained from a local butcher shop until a sequence was developed that met the above criteria. Minor changes were made to the general and geometry parameters of the scan sequence to accommodate the significant drop in size and volume of the sample being investigated. All diffusion values were kept constant to maximize consistency of the resultant ADC maps between the intervertebral disc bending and tissue strain experiments.

**Table 4.1 Diffusion weighted imaging sequence parameters**

Parameter	Value
<i>General</i>	
TE	29.4 ms
TR	750 ms
Averages	1
Scan time	26 m 52 s 00 ms
<i>Geometry</i>	
Field of View (FOV)	19.2 x 19.2 mm
Matrix Size	128 x 64
In Plane Resolution	0.150 x 0.300 mm
Slice Thickness	2.0 mm
# Slices: 3	3
<i>Diffusion</i>	
Directions	6
B-values	100, 400, 700, 1000 s/mm <sup>2</sup>
Gradient duration	8 ms
Gradient Separation	15 ms

## Specimen preparation

Discs were harvested from previously frozen cadaveric lumbar specimens (Table 4.2). Prior to preparation, spines were radiographed and evaluated by Shun Yamamoto, an orthopaedic surgeon to exclude bone pathology and categorize levels of disc degeneration. Specimens were thawed for 36 hours in a refrigeration unit maintained at 4 degrees Celsius in advance of preparation to ensure that they were completely thawed. Samples were harvested from discs across several donors. The same methods for degeneration assessment were done here as described in Chapter 3, Section 3.3.

**Table 4.2 Specimen and donor information**

<i><b>Donor ID</b></i>	<i><b>Level</b></i>	<i><b>Sex</b></i>	<i><b>Age</b></i>	<i><b>Degeneration</b></i>
H1013	L2-3 L3-4	M	76	Severe Moderate
H1275	L1-2 L2-3	M	79	Severe Moderate
H1331	L1-2 L2-3	F	79	Mild Mild

One day before testing in the MRI scanner, fat, muscle, and ligaments were resected from the lumbar specimens. The intervertebral disc was then carefully cut away from the cartilaginous endplates on either side. The outer layer of the annulus fibrosus was removed because it showed signs of minor freezer burn, defined for the purposes of this study as a discolouration and toughening of the exposed outer layer due to oxidation. This was noticed on the outer edges of several specimens. The remaining annulus fibrosus tissue was cut into 8.9 x 4.0 mm sections using a scalpel and a custom steel plate mounting a ruler with half-millimetre resolution (Figure 4.4). The height of the disc was kept intact and varied between samples.

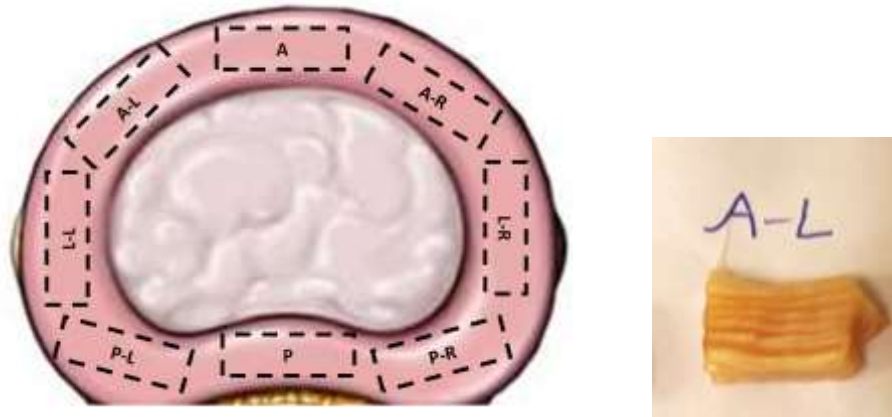


**Figure 4.4 Drawing of regions harvested for annulus fibrosus tissue samples (left) and photo of tissue sample harvested from the anterior-lateral side of the disc (right)**

## Experimental procedure

Once prepped, tissue samples were sprayed with a saline solution then stored in a refrigerator at 4 °C overnight wrapped in saline-soaked gauze. The samples were removed from the fridge in the morning and placed into the 3-D printed tissue mounts, with the caudal side in contact with the base and the cranial side facing upwards, exposed to the porous plunger. The tissue mounts were then aligned in the 10 cc syringe and the syringe was mounted into the loading device.

The loading device was then positioned within the receiver coil mounted inside the MRI bore, and the following steps were followed to obtain the necessary scans:

1. Loading device positioned within receiver coil in the MRI bore;
2. Anatomic reference scan - High-resolution T2-weighted axial;
3. Anatomic reference scan - High-resolution T2-weighted sagittal;
4. Axial diffusion weighted scan;
5. Compressive load applied to tissue sample;

6. Anatomic reference scan - High-resolution T2-weighted axial;
7. Anatomic reference scan - High-resolution T2-weighted sagittal; and
8. Axial diffusion weighted scan.

Once the protocol was completed, the syringe was removed and a new syringe containing the next sample was placed into the loading device within the MRI bore. This process was executed 18 times, with six tissue samples at each assessed level of degeneration (mild, moderate, severe).

After all 18 samples were tested, specimen H1331-A was re-imaged for 4 straight diffusion-weighted sequences, in an unloaded condition. This was done so that the repeatability of measurements could be evaluated – further details regarding this repeatability test are presented in Appendix G.

### **Image processing**

Compressive strain was measured from the sagittal anatomic reference scans before and after the load was applied to the sample using measurement tools in image processing software (3D slicer, version 4.6.2, Boston, MA). Because the disc tissue was constrained by both the floor of the mounting plate and the flat face of the plunger, which always remained parallel to each other, the height of the tissue remained constant throughout the sample. The distance between these two surfaces were measured at two locations across the length of the tissue sample, and the strain was taken as the average between the two.

Apparent diffusion coefficient maps were generated using a custom script calculating the ADC value for each voxel (MATLAB Mathworks, Natick, MA). The axial slice at the geometric centre of the disc of the ADC scan dataset was then segmented into an 8.9 x 4.0 mm section, defined as the region of interest (Figure 4.5). A tolerance of  $\pm 0.05$  mm was specified for each

dimension. This size was chosen because it eliminated one pixel-width from each edge of the cross-sectional area of the sample in order to minimize any partial volume effects; should any of the pixels on the outer edge of the sample overlap partially with the tissue mount, there would be contribution to the received signal from the plastic tissue mount, which would skew the relevant ADC value calculated for those voxels.

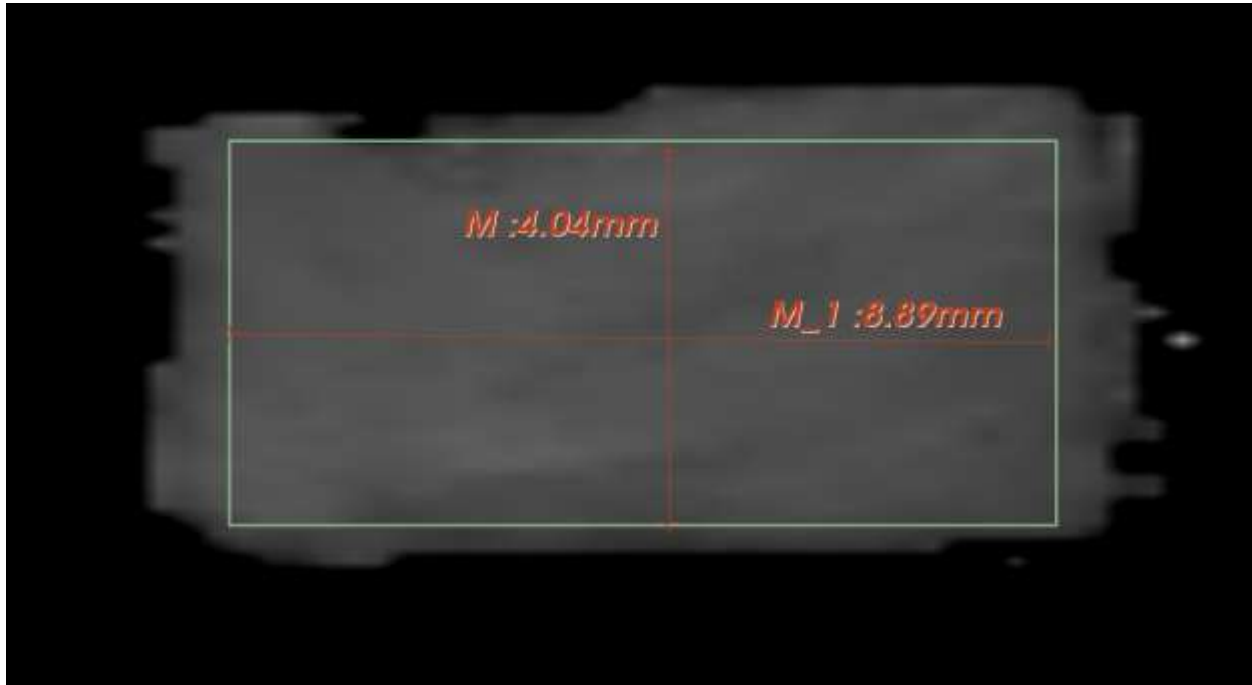


**Figure 4.5 Segmentation of annulus tissue sample in 3D Slicer.**

*The green line represents the segmented region; the dimensions of the region are shown in orange.*

Marker-based registration was performed within 3-D slicer to align unloaded and loaded images from corners of the mounting plate, which remained fixed between trials, as there were minor amounts of movement to the positioning of the loading device within the MRI bore during handling. Once the registration was completed, the same ROI was used for the unloaded and loaded scans by applying the same 8.9 x 4.0 mm mask to each respectively. Within the ROI, average ADC value and standard deviation was calculated for each state: loaded and unloaded (3D slicer, version 4.6.2, Boston, MA).



## **Statistical analysis**

Two-way analysis of variance with repeated measures was performed (SPSS Statistics, Version 23, Chicago, IL) to test for the effect of strain and degeneration on the change in mean apparent diffusion coefficient (ADC) within the annulus tissue. The same analysis was then repeated to test for the effect of strain and degenerative state on the change in coefficient of variance (COV), calculated as the ratio of standard deviation to the mean. Post-hoc tests were run using Tukey's Honestly Significant Difference to test for significance between individual parameters. Significance was set at  $p \leq 0.05$  for all tests in this study.

## **4.3 Results**

For each AF tissue sample, the apparent diffusion coefficient in the tissue was measured and compared between the unloaded (no strain) and loaded (compressive strain) states (Figure 4.6).

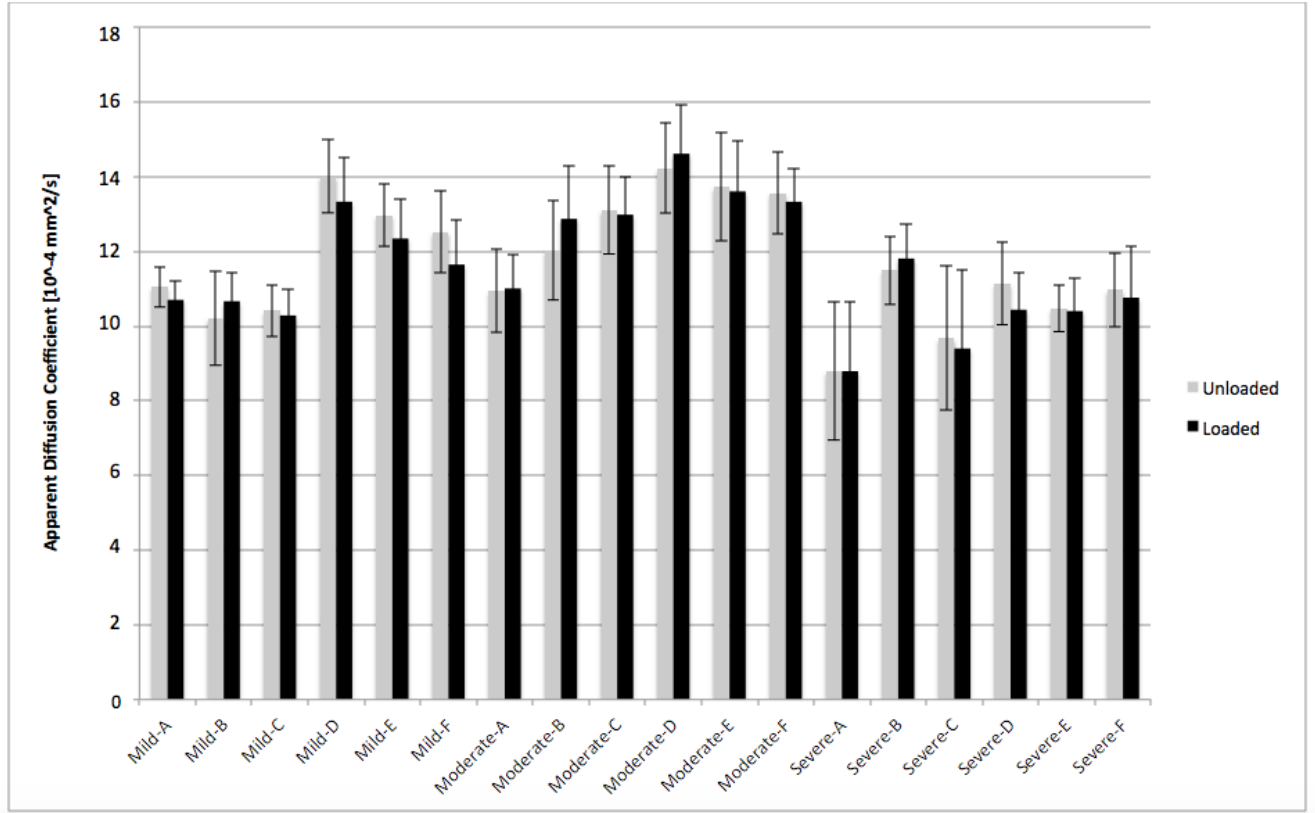


**Figure 4.6 ADC values in unloaded and loaded states across different degenerative grades**

To better visualize the change to the MR parameter as a result of the applied compression, we calculated the change in ADC as  $ADC_{unload} - ADC_{load}$ . We found that  $\Delta ADC$  was widely distributed; five samples were observed to have a negative  $\Delta ADC$ , representing an increase in the average ADC value with increasing compressive strain, while 13 samples were observed to have a positive  $\Delta ADC$  or a decrease in mean ADC with increasing compressive strain (Figure 4.7). A linear best-fit line of the  $\Delta ADC$  was calculated, with an R-squared value of +0.207.

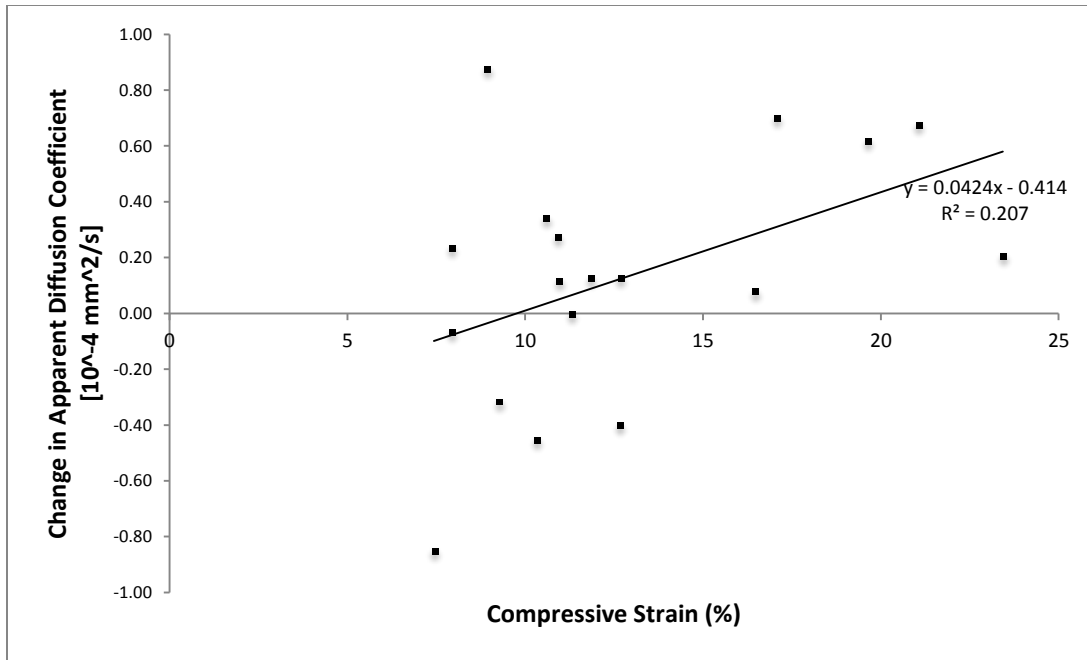


**Figure 4.7** Change in average ADC as a function of compressive strain for annulus fibrosus tissue samples

There was no significant change in ADC value with increasing strain, regardless of degeneration level ( $p = 0.235$ ). The Coefficient of Variance was compared at different levels of degeneration in both loaded and unloaded states (Table 4.3). We observed no significant change in COV with an increase in degenerative level ( $p = 0.191$ ) (Figure 4.8). Additionally, there was no significant change to COV with loading state ( $p = 0.669$ ).

**Table 4.3** Coefficient of Variance for the different levels of degeneration and loading state

Degenerative Level	COV (%)	COV (%)
	Unloaded state	Loaded state
Mild	7.7	7.7
Moderate	8.6	8.3
Severe	8.4	8.9

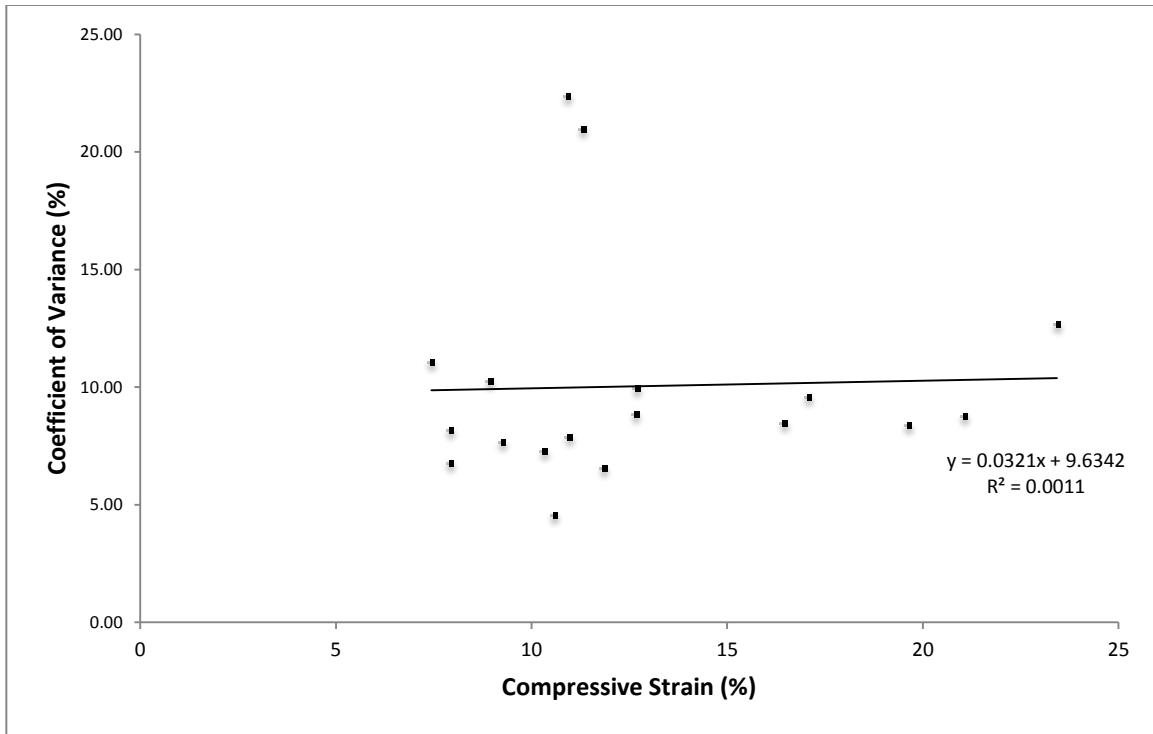


**Figure 4.8 COV of the ADC value in the annulus fibrosus tissue as a function of compressive strain**

Average ADC values, regardless of loading state, were compared between degenerative groups (Figure 4.9). We found that there was a significant decrease in ADC values between mild and severe degenerative grades ( $p = 0.047$ ) and moderate and severe degenerative grades ( $p = 0.002$ ). There was no change in discernable change in ADC between mild and moderate degenerative grades ( $p = 0.312$ ).

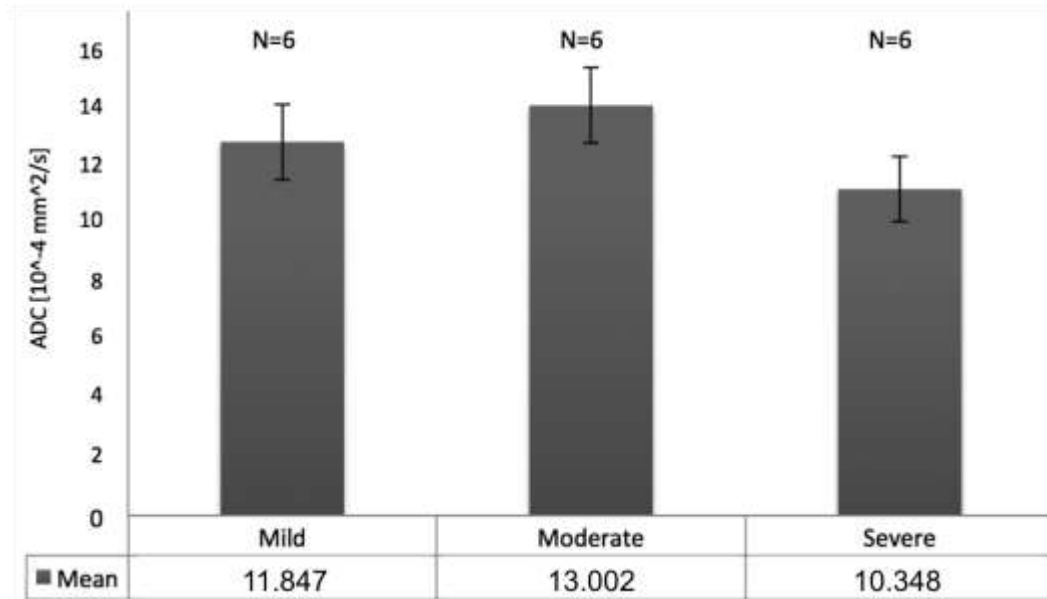


**Figure 4.9 Mean ADC measurements for different levels of degeneration**

#### **4.4 Discussion**

The purpose of this study was to investigate the relationship between apparent diffusion and compressive strain. We hypothesized that there would be a decrease in average ADC within the tissue for increasing compressive strain, but the data collected and analyzed in this study has caused us to reject this hypothesis. We found no statistically significant decrease in ADC after a compressive strain was applied to the tissue.

A statistically significant decrease in ADC with applied load within the annulus has been previously been reported [15], however our study found no such relationship. Furthermore, the same study found a statistically significant increase in COV with increasing level of degeneration, a finding that was also not replicated in this study.

An important consideration when comparing ADC measurements to compressive load is the resultant strain within the AF tissue. In a neutral (standing) posture, different regions of the AF tissue have been found to be subjected to both compressive and tensile strains [124].

Furthermore, during bending, the anterior region of the annulus shifts from a compressive strain

to a tensile strain when moving from flexion to extension, and the opposite trend was observed in the posterior region [124] (Figure 4.10). This combination of compressive and tensile strains in the disc was not considered previously when comparing ADC and loading condition, whereas the present study directly assessed this relationship by focussing solely on the relationship between ADC and compressive strain.

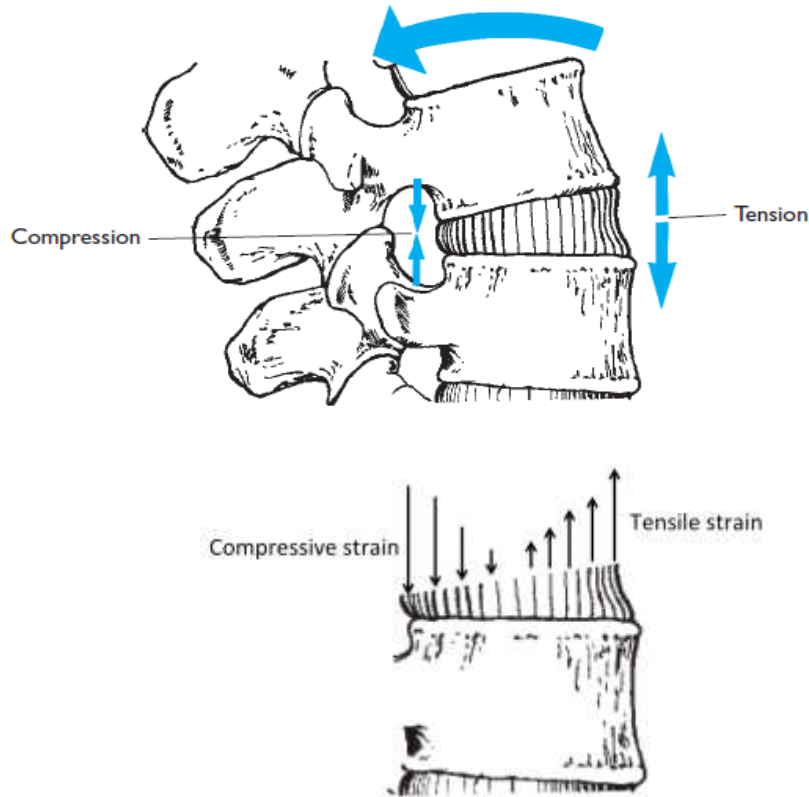


**Figure 4.10 Bending moment resulting in extension of the spine (top) and resultant strain profile through the disc (bottom)**

© Modified from [126], with permission

It is important to note, however, that the compressive strain applied to the specimens in this study is not fully representative of the strain profile *in vivo*. Here, the specimen was constrained on all sides, and were then subjected to an axial compressive strain. In reality, the strain induced in the AF tissue is more complex than this, as there is also load transfer from the NP to the AF during axial compression, which results in tensile circumferential strains in the outermost region

of the AF as the disc bulges outwards [127]. We chose to examine a simplified model of the strain state of the AF tissue so that the influence of the axial compressive strain on the change in ADC measurements could be directly evaluated. However, future work should incorporate this circumferential strain in order to more closely simulate *in vivo* loading conditions,

We anticipate that the change to the diffusion signal as a result of compressive strain is small relative to this natural variation, likely a result of the limitations of diffusion weighted imaging, which has poor image quality and worse resolution than other MRI sequences. We found high variation in the ADC of healthy AF tissue in an unloaded state (mean=  $11.85 [10^{-4}mm^2/s]$  and a standard deviation =  $1.220 [10^{-4}mm^2/s]$ ). The signal collected by the receiver coil in a diffusion weighted scan is that of the random movement of the free water in the disc tissue. When that movement becomes restricted, there is a concordant loss to the signal collected by the receiver coil. While the application of a compressive strain likely alters the diffusion of this free water, we expect that this was not significant enough to produce a reliable change to the measured ADC value. We also note that the disc, especially the AF, has been shown to undergo larger compressive and tensile strains in the degenerated disc [37]. The lack of correlation of ADC to strain, across all levels of degeneration, provides further support to our findings that ADC is not an effective parameter for assessing disc mechanical function.

There was a significant difference in ADC values between mild and severe degenerative grades and moderate and severe degenerative grades, with  $p = 0.047$  and  $p = 0.002$  respectively, regardless of loading condition. These correspond to an average decrease in ADC of 13% and 21%, respectively, which are similar findings to previous work: One study found a moderate decrease in ADC with increasing degeneration of 4% [95] while several other studies reported values similar to those reported here, ranging from 10 to 27% [85], [91], [121]. We

hypothesize that this significant decrease in ADC as a result of degeneration is a direct result of a decrease in the amount of free water within the annulus tissue. This water is the biggest contributor to signal in a diffusion weighted MRI scan. Since the amount of water decreases in the tissue as degeneration advances [27], [45], [128], there will be a concordant loss of signal on the MRI scan.

While there was significance decrease in ADC value with increasing degenerative level, this change was only observed with severe degenerative changes, suggesting that it may not be a more useful measurement tool than other common MRI sequences for investigating degenerative changes. Several other studies have reported a correlation between degeneration and water content as measured by MR imaging techniques, including T2-weighted MRI scans [129], [130] and proton density (PD) MRI [131]. The scan time for T2-weighted and PD sequences are significantly shorter than DWI. Therefore, if ADC measurements do not provide additional information regarding changes to the mechanics of the disc, it is not as likely to be a useful clinical tool as these faster MRI techniques due to the increased scan time.

A major limitation to the clinical relevance of the observed relationship between ADC and degenerative state is that changes were only evident with severe degenerative changes. There is still a need to develop a method to non-invasively identify subtle changes to the disc in the early stages of degeneration. While it has previously been suggested that apparent diffusion coefficient measurements may be able to identify these more subtle changes [15], the results of this study suggest this is not the case.

We note, however, that we have a relatively small sample size here, and so relationships may have been present that would be more apparent in a larger study. Based on the results presented here, in order to achieve a power of 0.8 and an effect size of 0.25, a minimum sample size of 51



specimens would be recommended for further investigation of the parameters studied in the present work.

## **Conclusion**

This chapter outlined the investigation of the relationship between apparent diffusion coefficient and compressive strain in isolated annulus fibrosus tissue samples of the lumbar intervertebral disc. We found no statistically significant change to ADC with an increase in compressive strain, regardless of degenerative state, in a study of 18 samples of cadaveric lumbar AF tissue.

ADC values were found to significantly decrease with increasing degeneration. However, this increase in degenerative level was only evident for a progression from mild or moderate generation to severe degeneration; there was no detectable change between mild and moderate levels of degeneration. While previous work suggested that ADC might be able to identify these more subtle changes in the degenerative process before reaching the ‘severe’ degenerative state, our results provide no evidence of this relationship between ADC and early-stage degeneration or mechanical behaviour.

## Chapter 5: Integrated discussion

### 5.1 Overview

The main objective of this research was to study the relationship between the apparent diffusion coefficient and physiologically relevant loading conditions. We expanded on previous work that explored the relationship between ADC and applied load in neutral postures (supine and standing) to include flexion and extension of the spine in order to further establish the feasibility of using ADC measurement as a tool to assess disc mechanics. Understanding the relationship between degeneration and altered disc mechanics may help bridge the gap between our current understanding of disc degeneration and discogenic pain, as current MRI assessment methods for stages of disc degeneration often do not align with the severity of symptoms seen clinically [21], [73], [74]. Previous MRI measurements in the disc were shown to be sensitive to loading conditions, with a significant decrease in ADC with increasing compressive load [15], however the findings presented in this thesis did not support such a relationship; we propose that alternative measures of disc mechanics for clinical applications are worth exploring over the use of ADC measurements.

The main contributions that arose from this work are:

- The development of a load measurement system compatible with a joint loading rig to measure forces acting on the intervertebral disc in the MRI environment. This rig was verified to accurately measure forces in the intervertebral disc up to 2500 N.
- The development of a methodology and imaging protocol to obtain ADC measurements in the intervertebral disc under four different loading conditions simulating postures of the spine (supine, standing, flexion, extension), which

provided evidence that the relationship between ADC and loading condition is not as strong as previously reported [15] and also expanded on this earlier study to include bending of the spine, which had not previously been considered.

- The development of a methodology and imaging protocol for studying the relationship between ADC and pure compressive strain on isolated samples of annulus fibrosus tissue. This portion of the study provided more conclusive evidence, in conjunction with the findings from Chapter 3, that ADC is not a sensitive measure of compressive strain caused by the loading conditions associated with different postures of the spine (supine, standing, flexion, and extension).

## **5.2 Strengths and contributions**

A central contribution of this work was the development of the load measurement system; its advantage over previously developed systems is its operational range. Previous groups have utilized similar fibre optic technologies to measure forces in the MRI environment, however the maximum forces they were able to measure fell well below peak forces experienced by the disc during postures such as standing, flexion, and extension of the spine [30], [33], [34], [103], [110]. We were able to develop a system capable of measuring forces during load applications that simulated loads experienced by the disc, *in vivo*, from natural (non-injurious) postures of the spine in the healthy adult disc [103]. This was a critical step in order to conduct the next portion of the study, where cadaveric lumbar specimens were subjected to loading conditions that simulated various postures of the spine in the MRI environment. The force measurement system allowed us to estimate forces and bending moments acting on the disc

directly within the bore of the MRI, ensuring that the conditions applied by the loading rig during the scan protocol aligned closely with previous reports of forces and moments resulting from the relevant simulated postures. Without these measurements during collection of the imaging data in the MRI environment, inaccurate loading conditions could have been applied and assumed to simulate these relevant postures, leading to false interpretation of the relationship between ADC and loading condition in the IVD.

Finally, another strength of the developed system is its portability and transferability. The placement of the FBG sensors within the removable piece of acrylic tubing in the IVD joint loading rig allows these sensors to easily be transferred to, and utilized by, other similar joint loading rigs for force measurement in the MRI environment.

Using the loading rig developed for this study, we were successful in applying loading conditions simulating relevant postures (supine, standing, flexion, and extension) to cadaveric functional spinal units. We were able to verify that the forces and bending moments fell within previously reported ranges for compressive force under similar postures [30], [33], [34], [103], [110] by using the fibre optic force measurement system during data collection. In parallel with the development of the joint loading rig, an imaging protocol on the 7.0 Tesla MRI scanner was developed to obtain diffusion-weighted axial scans of the lumbar intervertebral disc and to generate ADC maps from these scans.

There were several advantages provided by the developed method to quantify the boundary between nucleus and annulus tissue: firstly, it reduced data processing time by automating an otherwise tedious and time-consuming manual task. Secondly, it created a consistent definition of the NP-AF boundary between different test subjects. This helped to ensure that the comparison of ADC values between specimens was not significantly influenced

by variation resulting from manual segmentation, which is subject to human error. Furthermore, this method has great potential to be utilized in future studies of the IVD in which defining the boundary between the NP and the AF is necessary.

In order for ADC measurements to help improve current assessment methods, there would need to be a clear and consistent change in the ADC value under different loading conditions. From there, the changes in this relationship as a disc progresses from a healthy to degenerated state could then be established. This would allow for a non-invasive, *in vivo* assessment of the mechanics of the intervertebral disc, and how the mechanical behaviour changes as a result of disc degeneration. When used in addition to current assessment methods analyzing anatomic degenerative changes, we theorize that this information regarding disc mechanics could drastically improve the link between our current understanding of disc degeneration and clinical symptoms due to the importance of the mechanical role of the disc.

In this study, which was the first to investigate the relationship between the apparent diffusion coefficient and flexion/extension bending superimposed with compressive loads of cadaveric lumbar discs, we found no statistically significant change in ADC values between any two loading states (supine, standing, flexion and extension). Especially within the most anterior and posterior regions of the AF, we would expect to see a significant change in ADC between flexion and extension if it was sensitive to loading condition, as the tissue is subject to a very different mechanical state in either posture [36]; no statistically significant changes were observed between these two loading conditions, in either the anterior or posterior regions of the disc. While it has previously been suggested that ADC measurements have the potential to identify changes in disc mechanics in the MRI environment [15], we provide preliminary evidence that ADC measurements are not sensitive to different loading conditions and, as a

result, such measurements may not be an adequate tool for the proposed improvement to current clinical assessment methods.

To provide further evidence to our findings from testing full cadaver FSUs, we conducted a more controlled study using isolated AF tissues samples that allowed us to directly assess the relationship between ADC and compressive strain resulting from an applied load in the AF specifically. When considering the methodologies of the previous work correlating compressive load and ADC, the AF tissue was evaluated as a whole and did not specifically consider the strain induced by the compressive force [15]. However, studies have shown that annulus fibrosus tissue can be subjected to both compressive and tensile strain in different regions as a result of compressive loading [36]. A major contribution from this portion of the present study was to directly shed light on the relationship between ADC and pure compressive strain in isolated AF tissue samples, which had not previously been done. We found no significant relationship between ADC and compressive strain, across all levels of degeneration. These findings provided additional supporting evidence to our conclusions drawn from the results of the study of functional spinal units: we did not find ADC measurements to be sensitive to changes in loading condition. Therefore, we provide preliminary evidence that such measurements may not be a strong potential source for the desired information about changes to disc mechanics as a result of degeneration that could ultimately lead to development of an accurate clinical tool.

A recent study, published while the results of this study were being analysed, found a similar lack of correlation between ADC and the mechanical response of the disc. Three MR parameters (T1rho<sup>1</sup>, T2, and ADC) were compared to the mechanical behaviour of caprine intervertebral discs by looking at changes in the recovery behaviour of the disc following

---

<sup>1</sup> Also referred to as *spin lock*, T1rho is an MRI sequence refers to spin-lattice relaxation in a rotating frame with the application of a weak but constant “spin locking” RF pulse in the transverse plane

dynamic axial loading. They found that T1rho correlated to both mechanical response of disc tissue and histological degenerative score significantly better than either T2 or ADC [131]. ADC was not shown to provide indications of early-stage degeneration or disc disease. These findings, combined with the results presented in this thesis, provide evidence that ADC does not correlate well with either mechanical behaviour or early-stage degenerative changes.

Finally, the methodologies and devices developed for this thesis – especially the force measurement system, diffusion-weighted imaging protocol, and loading rig – have the potential to be used in future investigations of intervertebral disc mechanics using MRI. Our recommendations for future studies of the IVD are discussed in more detail in section 5.4.

### **5.3 Limitations**

There were several limitations to this study that should be noted. The first limitation is the use of the load measurement system. The measurements are limited to one degree of freedom (axial loading). However, biomechanics of the intervertebral disc is complex, with translation in three directions and rotation around each of these for a total of six degrees of freedom. Furthermore, movements of the spine rarely consist of a singular direction but rather coupled movements of both translation and rotation [112]. While accurate measurements of the overall range of forces being applied to the disc can be measured, assessment of the individual components of the coupled movements cannot be distinguished; the methods developed here only measure 1-DOF loading. There is potential for the methods to be extended to measure force along multiple axes, which could then be calibrated to calculate rotational movement, however this would require additional sensors and validation not described by this thesis.

Another limitation is the constraint on the joint during bending; due to the limited environment of the MRI bore, the loading plate of the loading rig can rotate 360 degrees, however it is unable to allow any gross translational movements along with rotation of the FSU. This may result in slightly different mechanics and stress profiles of the disc compared to *in vivo* measurements. However, we recognized that the designed rig applied compressive and bending loads to the disc that were within the range of those generated by postures of the spine *in vivo*, and was adequate for a pilot study such as this to establish a base relationship between mechanics and the investigated MR parameter. Furthermore, the magnitudes of the loads applied to simulate the relevant postures are average values taken from force ranges from previous studies and may not match what would be experienced by a single individual.

There were also limitations related to the imaging protocol for this study. Diffusion scan sequences are typically quite long; for the work in this thesis, the scan protocol took 26 minutes to acquire the relevant images. In this time, significant stress-relaxation was observed, with an initial steep drop in force, eventually reaching a steady-state over time. The exact impact of this behaviour on ADC measurements in the disc tissue has not been established. Furthermore, the long scan time relative to other MRI techniques, such as T1-weighted and T2-weighted sequences, could impact the feasibility of clinical application. Longer scan times result in increased costs, higher likelihood of poor image quality due to patient movement, and reduced comfort of the patient during assessment due the increased assessment time.

Another limitation of this study was that only the AF was considered in the study of isolated disc tissue examining the relationship between ADC and compressive strain. This was largely due to the more difficult nature of assessing mechanics of the nucleus pulposus tissue: due to its high water content and hydrostatic pressure under load (in healthy, young discs),



perforating the tissue to section it or dissecting away the surrounding annulus tissue has been shown to alter its mechanical behaviour [33]. Furthermore, we only considered compressive strain for the purposes of this study, though the annulus tissue is known to experience large tensile strains due to postural loading in addition to compression [36]. We also looked at axial compressive strain, and constrained the AF tissue from expanding radially. *In vivo*, the disc will bulge, resulting in large tensile circumferential strains in the outer regions of the AF tissue. The influence of circumferential strain on ADC measurements has not been fully established and may be worth investigating in future work.

The limited age range of the specimens used in this study is another limitation that should be addressed. This was driven by practical reasons, as young and healthy specimens are much more difficult to acquire. As a result, all of our specimens fell within the age range of 58-79 years of age. However, previous studies have shown that ADC values in the IVD are negatively correlated with age [85], [89], [90]; therefore, the effect of loading condition on ADC measurements may be more prevalent in young healthy discs, where average ADC values are generally higher and may show larger changes under load.

A further limitation is that our study only considers the nucleus pulposus and annulus fibrosus tissue, but does not address the role of the vertebral or cartilaginous endplate. As discussed in the first chapter of this thesis, the endplate plays an important role in the health and mechanics of the intervertebral disc: endplates play an important role in interfacing between the compliant IVD and the rigid vertebral bodies, and is also essential for the diffusion of water into and out of the disc [132]. Therefore, future investigations of the relationship between MR diffusion properties and mechanical behaviour of the disc may wish to incorporate the endplate, and is discussed further in the next section of this chapter.

## 5.4 Future work and recommendations

The first recommendation for future work is to use the devices and test protocols developed in this study to conduct a more thorough investigation of ADC measurements. We provide preliminary evidence of the relationship between ADC and loading condition with a very small sample size. The results here provide a foundation for future work to build on with a much larger sample size ( $n > 51$ ). We also recommend further investigation into the effect of age of the sample population tested on ADC measurement in conjunction with loading condition, as this study only look at relatively older IVDs, and the influence of this on the response of ADC to different loading conditions has not yet been established.

Secondly, we recommend future work to take into consideration more than just the NP and AF tissue and to consider the endplates. Permeability and diffusivity are also closely attributed to properties of the extrafibrillar matrix of the annulus fibrosus, which is also the main contributor to bearing compressive properties of the intervertebral disc. Therefore, it is reasonable to assume that MR diffusion properties of the disc are related to mechanical behaviour. Based on the findings from this research, however, the relationship between ADC and loading conditions simulating postures of the spine alone does not have significant potential as a clinical assessment tool as it does not provide any additional information regarding changes to the mechanics of the disc with increasing degeneration.

What may be of particular interest is using the methods developed here to investigate the properties and behaviour of the cartilaginous endplate in addition to the NP and AF. A study of 38 cadaveric lumbar motion segments found that damage to the vertebral endplate resulted in a drop in pressure in the nucleus pulposus by 25% and generated large compressive stresses in the annulus fibrosus [133]. Since the intervertebral disc is the largest avascular structure in the

body, diffusion of nutrients through the endplate is essential for disc health and performance. Diffusion imaging and apparent diffusion coefficient mapping may be of more interest in this area than in the disc tissue alone and has the potential to provide a more thorough understanding of changes to the disc as a result of degeneration by means of investigating diffusion properties.

My third recommendation for future work is to consider other MR parameters beyond the apparent diffusion coefficient alone. Recently, T1rho was found to correlate more strongly with mechanical behaviour – specifically changes in recovery behaviour following dynamic axial loading – than ADC in the intervertebral disc [131]. Furthermore, previous studies have found insignificant correlations between T2 and degenerative changes or mechanical behaviour, however these studies did not consider multi-component T2-mapping techniques. This imaging technique has shown great promise in other biomedical applications, and may be of interest to study with regards to the intervertebral disc. This may have greater potential than ADC measurements in order to translate the findings to *in vivo* studies; generally, T2 imaging sequences have been used more often than diffusion sequences for investigations of the IVD, and thus a study focusing on this property may have stronger established groundwork and available resources for *in vivo* investigations.

## **5.5 Conclusion**

This thesis outlines the three stages of work, each of which led to the establishment of the relationship between ADC values and loading conditions resulting from simulated postures of the spine in cadaveric lumbar specimens, which ultimately contributes to our understanding of MR measures of disc mechanics. Assessing mechanical behaviour of both healthy and degenerated discs is important to further our understanding of the degenerative process and make more informed clinical recommendations. The first stage of work involved the development of a

load measurement system for assessing loading conditions on the lumbar intervertebral disc in an MRI environment. Secondly, the study utilized this force measurement system to investigate changes to the apparent diffusion coefficient in four different loading conditions simulating relevant postures (supine, standing, flexion, and extension). Thirdly, this work directly related ADC values to compressive strain in isolated AF tissue samples. The results show that ADC is significantly higher in the NP than the AF, and decreases significantly with severe degeneration. However, no change to ADC (away from unloaded neutral posture readings) with simulated standing, flexion, and extension postures was observed. This lack of correlation between ADC and loading condition was further verified by the findings of the portion of the study relating ADC to compressive strain in small, isolated AF segments. We found no significant change to ADC with increasing compressive strain, regardless of degenerative state. These preliminary findings suggest that ADC measurements alone may not be useful for detecting subtle changes to disc mechanics that presumably accompany degeneration and compression of the tissue. We recommend future studies to include information from the vertebral endplates and possibly other MR parameters to further establish the relationship between subtle change to disc mechanics and early stage degeneration.

## Bibliography

- [1] J. Lawrence, "Disc degeneration. Its frequency and relationship to symptoms.," *Ann Rheum Dis*, vol. 28, no. 2, pp. 121–138, 1969.
- [2] J. W. Frymoyer, M. H. Pope, J. H. Clements, D. G. Wilder, B. MacPherson, and T. Ashikaga, "Risk factors in low-back pain. An epidemiological survey," *J. Bone Joint Surg. Am.*, vol. 65, no. 2, pp. 213–218, Feb. 1983.
- [3] M. C. Battié, T. Videman, and E. Parent, "Lumbar disc degeneration: epidemiology and genetic influences," *Spine*, vol. 29, no. 23, pp. 2679–2690, Dec. 2004.
- [4] S. Dagenais, J. Caro, and S. Haldeman, "A systematic review of low back pain cost of illness studies in the United States and internationally," *Spine J.*, vol. 8, no. 1, pp. 8–20, Jan. 2008.
- [5] J. N. Katz, "Lumbar disc disorders and low-back pain: socioeconomic factors and consequences," *J. Bone Joint Surg. Am.*, vol. 88 Suppl 2, pp. 21–24, Apr. 2006.
- [6] M.-V. Corniola *et al.*, "Correlation of pain, functional impairment, and health-related quality of life with radiological grading scales of lumbar degenerative disc disease," *Acta Neurochir. (Wien)*, vol. 158, no. 3, pp. 499–505, Mar. 2016.
- [7] J. Takatalo *et al.*, "Does lumbar disc degeneration on magnetic resonance imaging associate with low back symptom severity in young Finnish adults?," *Spine*, vol. 36, no. 25, pp. 2180–2189, Dec. 2011.
- [8] P. F. Beattie, "Diffusion-weighted magnetic resonance imaging of the musculoskeletal system: an emerging technology with potential to impact clinical decision making," *J. Orthop. Sports Phys. Ther.*, vol. 41, no. 11, pp. 887–895, Nov. 2011.
- [9] K. Luoma, H. Riihimäki, R. Luukkonen, R. Raininko, E. Viikari-Juntura, and A. Lamminen, "Low back pain in relation to lumbar disc degeneration," *Spine*, vol. 25, no. 4, pp. 487–492, Feb. 2000.
- [10] R. Chou, R. Fu, J. A. Carrino, and R. A. Deyo, "Imaging strategies for low-back pain: systematic review and meta-analysis," *Lancet Lond. Engl.*, vol. 373, no. 9662, pp. 463–472, Feb. 2009.
- [11] S. D. French *et al.*, "Imaging use for low back pain by Ontario primary care clinicians: protocol for a mixed methods study - the Back ON study," *BMC Musculoskelet. Disord.*, vol. 20, no. 1, p. 50, Feb. 2019.
- [12] A. Werber and M. Schiltenswolf, "Treatment of Lower Back Pain-The Gap between Guideline-Based Treatment and Medical Care Reality," *Healthc. Basel Switz.*, vol. 4, no. 3, Jul. 2016.
- [13] C. W. Pfirrmann, A. Metzdorf, M. Zanetti, J. Hodler, and N. Boos, "Magnetic resonance classification of lumbar intervertebral disc degeneration," *Spine*, vol. 26, no. 17, pp. 1873–1878, Sep. 2001.
- [14] D. C. Rim, "Quantitative Pfirrmann Disc Degeneration Grading System to Overcome the Limitation of Pfirrmann Disc Degeneration Grade," *Korean J. Spine*, vol. 13, no. 1, pp. 1–8, Mar. 2016.
- [15] R. N. Alkalay, D. Burstein, C. F. Westin, D. Meier, and D. Hackney, "MR diffusion is sensitive to mechanical loading in human intervertebral disks ex vivo."
- [16] S. Roberts, J. Menage, and J. P. Urban, "Biochemical and structural properties of the cartilage end-plate and its relation to the intervertebral disc," *Spine*, vol. 14, no. 2, pp. 166–174, Feb. 1989.

- [17] L. T. Twomey and J. R. Taylor, "Age changes in lumbar vertebrae and intervertebral discs," *Clin. Orthop.*, no. 224, pp. 97–104, Nov. 1987.
- [18] H. Inoue, "Three-dimensional architecture of lumbar intervertebral discs," *Spine*, vol. 6, no. 2, pp. 139–146, Apr. 1981.
- [19] J. Yu, P. C. Winlove, S. Roberts, and J. P. G. Urban, "Elastic fibre organization in the intervertebral discs of the bovine tail," *J. Anat.*, vol. 201, no. 6, pp. 465–475, Dec. 2002.
- [20] S. C. W. Chan, S. J. Ferguson, and B. Gantenbein-Ritter, "The effects of dynamic loading on the intervertebral disc," *Eur. Spine J.*, vol. 20, no. 11, pp. 1796–1812, Nov. 2011.
- [21] P. P. Raj, "Intervertebral disc: anatomy-physiology-pathophysiology-treatment," *Pain Pract. Off. J. World Inst. Pain*, vol. 8, no. 1, pp. 18–44, Feb. 2008.
- [22] M. Katz, A. Hargens, and S. Garfin, "Intervertebral disc nutrition. Diffusion versus convection. - PubMed - NCBI."
- [23] D. H. Cortes and D. M. Elliott, "The Intervertebral Disc: Overview of Disc Mechanics," in *The Intervertebral Disc: Molecular and Structural Studies of the Disc in Health and Disease*, I. M. Shapiro and M. V. Risbud, Eds. Vienna: Springer Vienna, 2014, pp. 17–31.
- [24] D. R. Eyre and H. Muir, "Quantitative analysis of types I and II collagens in human intervertebral discs at various ages," *Biochim. Biophys. Acta*, vol. 492, no. 1, pp. 29–42, May 1977.
- [25] B. Johnstone and M. T. Bayliss, "The large proteoglycans of the human intervertebral disc. Changes in their biosynthesis and structure with age, topography, and pathology," *Spine*, vol. 20, no. 6, pp. 674–684, Mar. 1995.
- [26] S. Roberts, S. M. Eisenstein, J. Menage, E. H. Evans, and I. K. Ashton, "Mechanoreceptors in intervertebral discs. Morphology, distribution, and neuropeptides," *Spine*, vol. 20, no. 24, pp. 2645–2651, Dec. 1995.
- [27] J. P. Urban and S. Roberts, "Degeneration of the intervertebral disc," *Arthritis Res. Ther.*, vol. 5, no. 3, pp. 120–130, 2003.
- [28] J. Pooni, D. Hukins, P. Harris, R. Hilton, and K. Davies, "Comparison of the structure of human intervertebral discs in the cervical, thoracic and lumbar regions of the spine," *Surg. Radiol. Anat.*, vol. 8, no. 3, pp. 175–182, Sep. 1986.
- [29] A. Nachemson, "THE EFFECT OF FORWARD LEANING ON LUMBAR INTRADISCAL PRESSURE," *Acta Orthop. Scand.*, vol. 35, pp. 314–328, 1965.
- [30] A. L. Nachemson, "The load on lumbar disks in different positions of the body," *Clin. Orthop.*, vol. 45, pp. 107–122, 1966.
- [31] D. S. McNally and M. A. Adams, "Internal intervertebral disc mechanics as revealed by stress profilometry," *Spine*, vol. 17, no. 1, pp. 66–73, 1992.
- [32] A. Nachemson, "The Influence of Spinal Movements on the Lumbar Intradiscal Pressure and on the Tensile Stresses in the Annulus Fibrosus," *Acta Orthop. Scand.*, vol. 33, no. 1–4, pp. 183–207, Jan. 1963.
- [33] N. Newell, A. Christou, M. Adams, C. Adam, and S. Masouros, "Biomechanics of the human intervertebral disc: A review of testing techniques and results."
- [34] H. J. Wilke, P. Neef, M. Caimi, T. Hoogland, and L. E. Claes, "New in vivo measurements of pressures in the intervertebral disc in daily life," *Spine*, vol. 24, no. 8, pp. 755–762, 1999.
- [35] R. D. Bowles and L. A. Setton, "Biomaterials for Intervertebral Disc Regeneration and Repair," *Biomaterials*, vol. 129, pp. 54–67, Jun. 2017.
- [36] A. Tsantrizos, K. Ito, M. Aebi, and T. Steffen, "Internal strains in healthy and degenerated lumbar intervertebral discs," *Spine*, vol. 30, no. 19, pp. 2129–2137, Oct. 2005.

- [37] G. D. O'Connell, E. J. Vresilovic, and D. M. Elliott, "Human Intervertebral Disc Internal Strain in Compression: The Effect of Disc Region, Loading Position, and Degeneration."
- [38] H. Anne L. Guerin and D. M. Elliott, "Structure and Properties of Soft Tissues in the Spine," in *Spine Technology Handbook*, 2006, pp. 35–62.
- [39] D. Cortes and D. Elliott, "The Intervertebral Disc: Overview of Disc Mechanics | SpringerLink." [Online]. Available: [https://link.springer.com/chapter/10.1007%2F978-3-7091-1535-0\\_2](https://link.springer.com/chapter/10.1007%2F978-3-7091-1535-0_2). [Accessed: 04-Dec-2018].
- [40] J. Melrose, S. M. Smith, R. C. Appleyard, and C. B. Little, "Aggrecan, versican and type VI collagen are components of annular translamellar crossbridges in the intervertebral disc," *Eur. Spine J. Off. Publ. Eur. Spine Soc. Eur. Spinal Deform. Soc. Eur. Sect. Cerv. Spine Res. Soc.*, vol. 17, no. 2, pp. 314–324, Feb. 2008.
- [41] J. Yu, J. C. T. Fairbank, S. Roberts, and J. P. G. Urban, "The elastic fiber network of the annulus fibrosus of the normal and scoliotic human intervertebral disc," *Spine*, vol. 30, no. 16, pp. 1815–1820, Aug. 2005.
- [42] H.-C. Wu and R.-F. Yao, "Mechanical behavior of the human annulus fibrosus," *J. Biomech.*, vol. 9, no. 1, pp. 1–7, Jan. 1976.
- [43] F. Travascio and W. Y. Gu, "Simultaneous measurement of anisotropic solute diffusivity and binding reaction rates in biological tissues by FRAP," *Ann. Biomed. Eng.*, vol. 39, no. 1, pp. 53–65, Jan. 2011.
- [44] S. Roberts, J. Menage, and J. P. G. Urban, "Biochemical and Structural Properties of the Cartilage End-plate and its Relation to the Intervertebral Disc," *Spine*, vol. 14, no. 2, pp. 166–174, Feb. 1989.
- [45] G. Lyons, S. M. Eisenstein, and M. B. Sweet, "Biochemical changes in intervertebral disc degeneration," *Biochim. Biophys. Acta*, vol. 673, no. 4, pp. 443–453, Apr. 1981.
- [46] N. Inoue and A. A. Espinoza Orías, "Biomechanics of Intervertebral Disc Degeneration," *Orthop. Clin. North Am.*, vol. 42, no. 4, pp. 487–499, Oct. 2011.
- [47] J. A. Buckwalter, "Aging and degeneration of the human intervertebral disc," *Spine*, vol. 20, no. 11, pp. 1307–1314, Jun. 1995.
- [48] J. Antoniou *et al.*, "The human lumbar intervertebral disc: evidence for changes in the biosynthesis and denaturation of the extracellular matrix with growth, maturation, ageing, and degeneration," *J. Clin. Invest.*, vol. 98, no. 4, pp. 996–1003, Aug. 1996.
- [49] F. Marchand and A. M. Ahmed, "Investigation of the laminate structure of lumbar disc annulus fibrosus," *Spine*, vol. 15, no. 5, pp. 402–410, May 1990.
- [50] J. Iatridis, "Alterations in the mechanical behavior of the human lumbar nucleus pulposus with degeneration and aging," *J. Orthop. Res. Off. Publ. Orthop. Res. Soc.*, vol. 15, no. 2, pp. 318–22, 1997.
- [51] J. C. Iatridis, L. A. Setton, R. J. Foster, B. A. Rawlins, M. Weidenbaum, and V. Mow, "Degeneration affects the anisotropic and nonlinear behaviors of human annulus fibrosus in compression," *J. Biomech.*, vol. 31, no. 6 JUN, pp. 535–544, 1998.
- [52] I. A. F. Stokes and J. C. Iatridis, "Mechanical conditions that accelerate intervertebral disc degeneration: overload versus immobilization," *Spine*, vol. 29, no. 23, pp. 2724–2732, Dec. 2004.
- [53] K. Yong-Hing and W. H. Kirkaldy-Willis, "The pathophysiology of degenerative disease of the lumbar spine," *Orthop. Clin. North Am.*, vol. 14, no. 3, pp. 491–504, Jul. 1983.
- [54] L. E. Kazarian, "Creep characteristics of the human spinal column," *Orthop. Clin. North Am.*, vol. 6, no. 1, pp. 3–18, Jan. 1975.

- [55] T. S. Keller, D. M. Spengler, and T. H. Hansson, "Mechanical behavior of the human lumbar spine. I. Creep analysis during static compressive loading," *J. Orthop. Res. Off. Publ. Orthop. Res. Soc.*, vol. 5, no. 4, pp. 467–478, 1987.
- [56] W. J. Virgin, "Experimental investigations into the physical properties of the intervertebral disc," *Bone Jt. J.*, vol. 33–B, no. 4, pp. 607–611, Nov. 1951.
- [57] P. P. Raj, "Intervertebral Disc: Anatomy-Physiology-Pathophysiology-Treatment," *Pain Pract.*, vol. 8, no. 1, pp. 18–44, Jan. 2008.
- [58] P. Pollintine, A. S. Przybyla, P. Dolan, and M. A. Adams, "Neural arch load-bearing in old and degenerated spines," *J. Biomech.*, vol. 37, no. 2, pp. 197–204, Feb. 2004.
- [59] M. a Adams, D. S. McNally, and P. Dolan, "'Stress' distributions inside intervertebral discs. The effects of age and degeneration.," *J. Bone Joint Surg. Br.*, vol. 78, no. 6, pp. 965–72, Nov. 1996.
- [60] M. G. Muriuki *et al.*, "Effects of motion segment level, Pfirrmann intervertebral disc degeneration grade and gender on lumbar spine kinematics," *J. Orthop. Res.*, vol. 34, no. 8, pp. 1389–1398, 2016.
- [61] A. M. Ellingson, H. Mehta, D. W. Polly, J. Ellermann, and D. J. Nuckley, "Disc degeneration assessed by quantitative T2\* (T2 star) correlated with functional lumbar mechanics," *Spine*, vol. 38, no. 24, pp. E1533–1540, Nov. 2013.
- [62] M. Mimura, M. M. Panjabi, T. R. Oxland, J. J. Crisco, I. Yamamoto, and A. Vasavada, "Disc Degeneration Affects the Multidirectional Flexibility of the Lumbar Spine," *SPINE*, vol. 19, no. 12, pp. 1371–1380, 1994.
- [63] J. Nixon, "Intervertebral disc mechanics: a review.," *J. R. Soc. Med.*, vol. 79, no. 2, pp. 100–104, Feb. 1986.
- [64] S. A. Zirbel, D. K. Stolworthy, L. L. Howell, and A. E. Bowden, "Intervertebral disc degeneration alters lumbar spine segmental stiffness in all modes of loading under a compressive follower load," *Spine J. Off. J. North Am. Spine Soc.*, vol. 13, no. 9, pp. 1134–1147, Sep. 2013.
- [65] E. J. Carragee and T. F. Alamin, "Discography: a review," *Spine J.*, vol. 1, no. 5, pp. 364–372, Sep. 2001.
- [66] A. R. Block, H. Vanharanta, D. D. Ohnmeiss, and R. D. Guyer, "Discographic Pain Report: Influence of Psychological Factors," *Spine*, vol. 21, no. 3, p. 334, Feb. 1996.
- [67] E. J. Carragee, Y. Chen, C. M. Tanner, T. K. T. Truong, E. Lau, and J. V. de Brito, "Provocative discography in patients after limited lumbar discectomy: A controlled, randomized study of pain response in symptomatic and asymptomatic subjects.," *Spine*, vol. 25, no. 23, pp. 3065–3071, 2000.
- [68] D. D. Ohnmeiss, H. Vanharanta, and R. D. Guyer, "The association between pain drawings and computed tomographic/discographic pain responses," *Spine*, vol. 20, no. 6, pp. 729–733, Mar. 1995.
- [69] A. Kettler and H.-J. Wilke, "Review of existing grading systems for cervical or lumbar disc and facet joint degeneration," *Eur. Spine J.*, vol. 15, no. 6, pp. 705–718, Jun. 2006.
- [70] J. P. Thompson, R. H. Pearce, M. T. Schechter, M. E. Adams, I. K. Tsang, and P. B. Bishop, "Preliminary evaluation of a scheme for grading the gross morphology of the human intervertebral disc," *Spine*, vol. 15, no. 5, pp. 411–415, May 1990.
- [71] N. Boos, S. Weissbach, H. Rohrbach, C. Weiler, K. F. Spratt, and A. G. Nerlich, "Classification of age-related changes in lumbar intervertebral discs: 2002 Volvo Award in basic science," *Spine*, vol. 27, no. 23, pp. 2631–2644, Dec. 2002.



- [72] N. E. Lane, M. C. Nevitt, H. K. Genant, and M. C. Hochberg, "Reliability of new indices of radiographic osteoarthritis of the hand and hip and lumbar disc degeneration," *J. Rheumatol.*, vol. 20, no. 11, pp. 1911–1918, Nov. 1993.
- [73] J. G. Jarvik and R. A. Deyo, "Diagnostic evaluation of low back pain with emphasis on imaging," *Ann. Intern. Med.*, vol. 137, no. 7, pp. 586–597, Oct. 2002.
- [74] A. D. L. Baker, "Abnormal Magnetic-Resonance Scans of the Lumbar Spine in Asymptomatic Subjects. A Prospective Investigation," in *Classic Papers in Orthopaedics*, P. A. Banaszkiewicz and D. F. Kader, Eds. London: Springer London, 2014, pp. 245–247.
- [75] M. J. Hancock *et al.*, "Systematic review of tests to identify the disc, SIJ or facet joint as the source of low back pain," *Eur. Spine J.*, vol. 16, no. 10, pp. 1539–1550, Oct. 2007.
- [76] R. Chou, S. J. Atlas, S. P. Stanos, and R. W. Rosenquist, "Nonsurgical Interventional Therapies for Low Back Pain: A Review of the Evidence for an American Pain Society Clinical Practice Guideline," *Spine*, vol. 34, no. 10, pp. 1078–1093, May 2009.
- [77] M. F. Dempsey, B. Condon, and D. M. Hadley, "MRI safety review," *Semin. Ultrasound CT MRI*, vol. 23, no. 5, pp. 392–401, Oct. 2002.
- [78] J. Graessner, "Frequently Asked Questions: Diffusion Weighted Imaging (DWI) — Clinical MRI," *Clinical-MRI*. [Online]. Available: <http://clinical-mri.com/frequently-asked-questions-diffusion-weighted-imaging-dwi/>. [Accessed: 14-Dec-2018].
- [79] M. Y. Park and J. Y. Byun, "Understanding the Mathematics Involved in Calculating Apparent Diffusion Coefficient Maps," *Am. J. Roentgenol.*, vol. 199, no. 6, pp. W784–W784, Dec. 2012.
- [80] L. Maas and P. Mukherjee, "Diffusion MRI: Overview and clinical applications in neuroradiology." [Online]. Available: <https://appliedradiology.com/articles/diffusion-mri-overview-and-clinical-applications-in-neuroradiology>. [Accessed: 23-Feb-2019].
- [81] S. Kinner, S. Blex, S. Maderwald, M. Forsting, G. Gerken, and T. C. Lauenstein, "Addition of diffusion-weighted imaging can improve diagnostic confidence in bowel MRI," *Clin. Radiol.*, vol. 69, no. 4, pp. 372–377, Apr. 2014.
- [82] H. Haradome, L. Grazioli, M. Morone, and S. Gambarini, "T2-weighted and diffusion-weighted MRI for discriminating benign from malignant focal liver lesions: Diagnostic abilities of single versus combined interpretations | Request PDF," *ResearchGate*, vol. 35, no. 6, pp. 1388–96, Jun. 2012.
- [83] G. S. Chilla, C. H. Tan, C. Xu, and C. L. Poh, "Diffusion weighted magnetic resonance imaging and its recent trend-a survey," *Quant. Imaging Med. Surg.*, vol. 5, no. 3, pp. 407–422, Jun. 2015.
- [84] M. G. Lansberg *et al.*, "Evolution of apparent diffusion coefficient, diffusion-weighted, and T2-weighted signal intensity of acute stroke," *AJNR Am. J. Neuroradiol.*, vol. 22, no. 4, pp. 637–644, Apr. 2001.
- [85] J. Antoniou *et al.*, "Apparent diffusion coefficient of intervertebral discs related to matrix composition and integrity," *Magn. Reson. Imaging*, vol. 22, no. 7, pp. 963–972, Sep. 2004.
- [86] R. Bammer, "Basic principles of diffusion-weighted imaging," *Eur. J. Radiol.*, vol. 45, no. 3, pp. 169–184, Mar. 2003.
- [87] N. Boos and C. Boesch, "Quantitative Magnetic Resonance Imaging of the Lumbar Spine: Potential for Investigations of Water Content and Biochemical Composition," *Spine*, vol. 20, no. 21, p. 2358, Nov. 1995.


- [88] L. Kertulla, M. Kurunlahti, J. Jauhiainen, A. Koivula, J. Oikarinen, and O. Tervonen, "Apparent diffusion coefficients and T2 relaxation time measurements to evaluate disc degeneration."
- [89] S. M. Kealey, T. Aho, D. Delong, D. P. Barboriak, J. M. Provençal, and J. D. Eastwood, "Assessment of Apparent Diffusion Coefficient in Normal and Degenerated Intervertebral Lumbar Disks: Initial Experience."
- [90] Z. Zhang *et al.*, "Age-related diffusion patterns in human lumbar intervertebral discs: a pilot study in asymptomatic subjects," *Magn. Reson. Imaging*, vol. 30, no. 2, pp. 181–188, Feb. 2012.
- [91] W. Zhang *et al.*, "Assessment of apparent diffusion coefficient in lumbar intervertebral disc degeneration," *Eur. Spine J. Off. Publ. Eur. Spine Soc. Eur. Spinal Deform. Soc. Eur. Sect. Cerv. Spine Res. Soc.*, vol. 23, no. 9, pp. 1830–1836, Sep. 2014.
- [92] B. Ludescher *et al.*, "T2- and diffusion-maps reveal diurnal changes of intervertebral disc composition: An in vivo MRI study at 1.5 Tesla," *J. Magn. Reson. Imaging*, vol. 28, no. 1, pp. 252–257, Jul. 2008.
- [93] E. Belykh *et al.*, "Apparent diffusion coefficient maps in the assessment of surgical patients with lumbar spine degeneration," *PLOS ONE*, vol. 12, no. 8, p. e0183697, Aug. 2017.
- [94] E. J. Chiu, D. C. Newitt, M. R. Segal, S. S. Hu, J. C. Lotz, and S. Majumdar, "Magnetic resonance imaging measurement of relaxation and water diffusion in the human lumbar intervertebral disc under compression in vitro," *Spine*, vol. 26, no. 19, pp. E437–444, Oct. 2001.
- [95] J. Niinimäki *et al.*, "Association between visual degeneration of intervertebral discs and the apparent diffusion coefficient," *Magn. Reson. Imaging*, vol. 27, no. 5, pp. 641–647, Jun. 2009.
- [96] A. Watanabe, L. M. Benneker, C. Boesch, T. Watanabe, T. Obata, and S. E. Anderson, "Classification of intervertebral disk degeneration with axial T2 mapping," *AJR Am. J. Roentgenol.*, vol. 189, no. 4, pp. 936–942, Oct. 2007.
- [97] D. M. Krainak, T. B. Parrish, and J. P. A. Dewald, "A method to capture six-degrees-of-freedom mechanical measurements of isometric shoulder and elbow torques during event-related fMRI," *J. Neurosci. Methods*, vol. 161, no. 2, pp. 314–322, Apr. 2007.
- [98] R. Gassert, D. Chapuis, H. Bleuler, and E. Burdet, "Sensors for Applications in Magnetic Resonance Environments," *IEEEASME Trans. Mechatron.*, vol. 13, no. 3, pp. 335–344, Jun. 2008.
- [99] T. Butzer, M. Rinderknecht, G. Johannes, W. Popp, O. Lehner, and R. Gassert, "Design and Evaluation of a Fiber-Optic Grip Force Sensor with Compliant 3D-Printable Structure for (f)MRI Applications." [Online]. Available: <https://www.hindawi.com/journals/js/2016/6248178/>. [Accessed: 09-Nov-2018].
- [100] L. Dziuda, M. Krej, and F. W. Skibniewski, "Fiber Bragg Grating Strain Sensor Incorporated to Monitor Patient Vital Signs During MRI," *IEEE Sens. J.*, vol. 13, no. 12, pp. 4986–4991, Dec. 2013.
- [101] K. Moerman, A. Sprengers, A. Nederveen, and C. Simms, "A novel MRI compatible soft tissue indenter and fibre Bragg grating force sensor. - PubMed - NCBI." [Online]. Available: <https://www.ncbi.nlm.nih.gov/pubmed/?term=A+novel+MRI+compatible+soft+tissue++indenter+and+fibre+Bragg+grating+force+sensor.> [Accessed: 09-Nov-2018].

- [102] C. Dennison, P. Wild, D. Wilson, and M. Gilbert, "An in-fiber Bragg grating sensor for contact force and stress measurements in articular joints - IOPscience," *Meas. Sci. Technol.*, vol. 21, no. 11.
- [103] A. L. Nachemson and J. M. Morris, "In Vivo Measurements of Intradiscal Pressure: Discometry, Method for the Determination of Pressure in the Lower Lumbar Discs," *J. Bone Jt. Surgery American Vol.*, vol. 46-A, no. 5, pp. 1077–1092, 1964.
- [104] M. A. Adams, D. S. McNally, H. Chinn, and P. Dolan, "The clinical biomechanics award paper 1993 Posture and the compressive strength of the lumbar spine," *Clin. Biomech.*, vol. 9, no. 1, pp. 5–14, Jan. 1994.
- [105] R. Measures, *Structural Monitoring with Fiber Optic Technology*, 1st ed. Academic Press, 2001.
- [106] M. Aly and F. Heba, "Compensating Bragg Wavelength Drift due to Temperature and Pressure by Applying an Artificial Strain."
- [107] R. Marsili, G. Rossi, and E. Speranzini, "Fibre Bragg Gratings for the Monitoring of Wooden Structures," *Materials*, vol. 11, no. 1, Dec. 2017.
- [108] B. K. A. Ngoi, J. Paul, L. P. Zhao, and Z. P. Fang, "Enhanced lateral pressure tuning of fiber Bragg gratings by polymer packaging," *Opt. Commun.*, vol. 242, no. 4, pp. 425–430, Dec. 2004.
- [109] H. van Duinen, M. Post, K. Vaartjes, H. Hoogduin, and I. Zijdwind, "MR compatible strain gauge based force transducer," *J. Neurosci. Methods*, vol. 164, no. 2, pp. 247–254, Aug. 2007.
- [110] A. Rohlmann, L. E. Claes, G. Bergmann, F. Graichen, P. Neef, and H. J. Wilke, "Comparison of intradiscal pressures and spinal fixator loads for different body positions and exercises," *Ergonomics*, vol. 44, no. 8, pp. 781–94, 2001.
- [111] L. Xu, L. A. Feuerman, J. Ge, K. R. Nilsson, and M. P. Fok, "Temperature-Insensitive Contact Force Sensing in Bi-Directional Catheter Using Fiber Bragg Grating Pair," *IEEE Sens. J.*, vol. PP, pp. 1–1, Jun. 2017.
- [112] M. Panjabi, T. Oxland, I. Yamamoto, and J. Crisco, "Mechanical behavior of the human lumbar and lumbosacral spine as shown by three-dimensional load-displacement curves," *J Bone Jt. Surg Am*, vol. 76, no. 3, pp. 413–424, Mar. 1994.
- [113] N. Crawford, A. G. U. Brantley, C. A. Dickman, and E. J. Koeneman, "An apparatus for applying pure nonconstraining moments to spine segments in vitro," *Spine*, vol. 20, pp. 2097–2100, 1995.
- [114] E. Pusey *et al.*, "Magnetic resonance imaging artifacts: mechanism and clinical significance," *RadioGraphics*, vol. 6, no. 5, pp. 891–911, Sep. 1986.
- [115] E. K. Keeler *et al.*, "Accessory equipment considerations with respect to MRI compatibility," *J. Magn. Reson. Imaging*, vol. 8, no. 1, pp. 12–18, Jan. 1998.
- [116] H. J. Wilke, L. Claes, H. Schmitt, and S. Wolf, "A universal spine tester for in vitro experiments with muscle force simulation," *Eur. Spine J.*, vol. 3, no. 2, pp. 91–7, 1994.
- [117] A. G. Patwardhan *et al.*, "Effect of compressive follower preload on the flexion-extension response of the human lumbar spine," *J Orthop Res*, vol. 21, no. 3, pp. 540–6, 2003.
- [118] H.-J. Wilke, F. Rohlmann, C. Neidlinger-Wilke, A. Kettler, K. Werner, and L. Claes, "Validity and interobserver agreement of a new radiographic grading system for intervertebral disc degeneration: Part I. Lumbar spine," *Eur. Spine J. Off. Publ. Eur. Spine Soc. Eur. Spinal Deform. Soc. Eur. Sect. Cerv. Spine Res. Soc.*, vol. 15, no. 6, pp. 720–730, Jun. 2006.

- [119] M. A. Adams and P. Dolan, "A technique for quantifying the bending moment acting on the lumbar spine in vivo," *J Biomech*, vol. 24, no. 2, pp. 117–26, 1991.
- [120] K. R Wade, P. A Robertson, and N. D Broom, "On the Extent and Nature of Nucleus-Annulus Integration," *Spine*, vol. 37, pp. 1826–33, Jun. 2012.
- [121] E. J. Chiu, D. C. Newitt, M. R. Segal, S. S. Hu, J. C. Lotz, and S. Majumdar, "Magnetic resonance imaging measurement of relaxation and water diffusion in the human lumbar intervertebral disc under compression in vitro," *Spine*, vol. 26, no. 19, pp. E437-444, Oct. 2001.
- [122] A. D. Holmes and D. W. L. Hukins, "Analysis of load-relaxation in compressed segments of lumbar spine," *Med. Eng. Phys.*, vol. 18, no. 2, pp. 99–104, 1996.
- [123] K. Markolf and J. Morris, "The Structural Components of the Intervertebral Disc," *J. Bone Jt. Surg.*, vol. 56, no. 4, pp. 675–687, Jun. 1974.
- [124] G. D. O'Connell, W. Johannessen, E. J. Vresilovic, and D. M. Elliott, "Human Internal Disc Strains in Axial Compression Measured Noninvasively Using Magnetic Resonance Imaging," *Spine*, vol. 32, no. 25, p. 2860, Dec. 2007.
- [125] R. Y. Neches, K. J. Flynn, L. Zaman, E. Tung, and N. Pudlo, "On the intrinsic sterility of 3D printing," *PeerJ*, vol. 4, Dec. 2016.
- [126] S. J. Hall, *Basic Biomechanics*, 7th ed. New York: McGraw-Hill, 2015.
- [127] A. Michalek, M. Gardner-Morse, and J. Iatridis, "Large Residual Strains are Present in the Intervertebral Disc Annulus Fibrosus in the Unloaded State," *J. Biomech.*, vol. 45, no. 7, pp. 1227–1231, Apr. 2012.
- [128] J. P. G. Urban, S. Roberts, and J. R. Ralphs, "The Nucleus of the Intervertebral Disc from Development to Degeneration," *Integr. Comp. Biol.*, vol. 40, no. 1, pp. 53–061, Feb. 2000.
- [129] L. Kerttula, M. Kurunlahti, J. Jauhiainen, A. Koivula, J. Oikarinen, and O. Tervonen, "Apparent diffusion coefficients and T2 relaxation time measurements to evaluate disc degeneration. A quantitative MR study of young patients with previous vertebral fracture," *Acta Radiol. Stockh. Swed.* 1987, vol. 42, no. 6, pp. 585–591, Nov. 2001.
- [130] K. Chatani, Y. Kusaka, T. Mifune, and H. Nishikawa, "Topographic differences of <sup>1</sup>H-NMR relaxation times (T1, T2) in the normal intervertebral disc and its relationship to water content," *Spine*, vol. 18, no. 15, pp. 2271–2275, Nov. 1993.
- [131] C. Paul, T. Smit, M. de Graaf, R. Holewijn, and A. Bisschop, "Quantitative MRI in early intervertebral disc degeneration: T1rho correlates better than T2 and ADC with biomechanics, histology and matrix content." [Online]. Available: <https://www.ncbi.nlm.nih.gov/pmc/articles/PMC5790235/>. [Accessed: 04-Dec-2018].
- [132] J. C. Lotz, A. J. Fields, and E. C. Liebenberg, "The role of the vertebral end plate in low back pain," *Glob. Spine J.*, vol. 3, no. 3, pp. 153–164, Jun. 2013.
- [133] M. A. Adams, B. J. C. Freeman, H. P. Morrison, I. W. Nelson, and P. Dolan, "Mechanical Initiation of Intervertebral Disc Degeneration," *Spine*, vol. 25, no. 13, p. 1625, Jul. 2000.

## Appendices


### Appendix A Load measurement system specification



INNOVATIONSPRODUCTSSUPPORTCOMMUNITY

MY ACCOUNT  
Log In

0



## PXIe-1078

### PXI Chassis

Starting from **CAD 3,815.00**

[VIEW PRODUCT DETAILS](#)[Configure A Custom NI System](#)

**PXIe, 9-Slot, Up to 1.75 GB/s PXI Chassis**—The PXIe-1078 features a backplane that incorporates a PCI Express connection to every slot to meet a wide range of test and measurement application needs. It accepts PXI Express modules in every slot and supports standard PXI hybrid-compatible modules in up to five slots.



# PXIe-8133

## PXI Controller

[Request Pricing](#)

Life Cycle Status: [Obsolete](#)

**3.06 GHz, Quad-Core Processor, PXI Embedded Controller**—The PXIe-8133 is an Intel Core i7 embedded controller for PXI and CompactPCI systems. It is used for modular instrumentation and DAQ applications. The PXIe-8133 includes 10/100/1000BASE-TX (Gigabit) Ethernet and four Hi-Speed USB ports, as well as an integrated hard drive and other peripheral I/O.



# PXIe-4844

## PXI Universal Input Module

[Request Pricing](#)

Life Cycle Status: [Mature](#) | Last Orderable Date: 29/06/17

**Optical Sensor, 4-Channel PXI Universal Input Module** —The PXIe-4844 is a dual-slot data acquisition module for fiber Bragg grating (FBG) optical sensors. The PXIe-4844 features an optical core which combines a high-power, low-noise swept wavelength laser with fiber Fabry-Perot tunable filter technology from Micron Optics. You can extend the maximum number of FBG sensors per module by connecting one or more optical channels to an external optical multiplexer or by adding multiple PXIe-4844 modules to the same chassis.

You configure the NI PXIe-4844 in the NI-OSI Explorer, a configuration manager that scans the optical wavelength range to identify all connected FBG sensors. After you specify the range and scaling equations, all scans automatically parse the data into individual sensor measurements and scale the data appropriately.

## **Specifications Support Document for Technica Quote TOC180517-AC1**

### **Single FBG Sensor Specifications:**

CW: 1555nm

CW Tolerance: +/- 0.5 nm

BW (Bandwidth @ 3dB): 0.3nm

BW Tolerance: +/- 0.05nm

Reflectivity: >50%

SLSR (Side Lobe Suppression Ratio): >15dB

Fiber type: smf28c

Coating type: Polyimide

Optical Connectors: FC/APC

Single FBG sensor construction: FC/APC – 0.75m fiber – FBG1 – 0.015m fiber

Temperature rating: 100C



## Clear Cast Acrylic Tube

5" OD x 4-1/2" ID



Length, ft.

1

3

5



Each

**ADD TO ORDER**

8486K581

Material	Acrylic Plastic
Fabrication	Cast
Cross Section Shape	Round
Construction	Hollow
Texture	Smooth
Color	Clear
Clarity	Clear
OD	5"
OD Tolerance	-0.045" to +0.045"
Tolerance Rating	Standard
ID	4 1/2"
Wall Thickness	1/4"
Wall Thickness Tolerance	-0.038" to +0.038"
Length Tolerance	-1" to +1"
Hardness	Rockwell M95



▶ **Loctite - Industrial Adhesives and Sealants**

▼ **Product Search**

▶ **Search**

▶ Products by Applications

▶ Products by Industry Segment

▶ Our Highlights

▶ Data Sheets

▶ Where to buy

▶ Contact & Services

▶ Videos & Literature

▶ News & Events

▶ Training

▶ About Henkel

▶ Consumer: Super Glue - 60 sec.



> Loctite - Industrial Adhesives and Sealants > Product Search > Search

◀ Back to Overview



## LOCTITE AA 3525 (Known as LOCTITE 3525)

Light-cure acrylic-based adhesive. Strong and tough, it is well suited to bonding plastics and metals. Low yellowing effect in sunlight.

LOCTITE® AA 3525 is a clear, light-cured, acrylic-based adhesive that is toughened for high strength bonding. Although well suited to plastics and metals, it can also bond glass and ceramics. It offers low yellowing in a sunlit environment. The tack-free time is 10 secs, while the fixturing time is 5 secs. Depth of cure is >13 mm. Service temperature is up to 140°C.

### Your benefits

- High strength, toughened
- Well suited to plastics and metals
- Ideal for electric motor balancing applications
- Low yellowing in sunlight





## FC/APC to SC/APC Hybrid Simplex Singlemode Plastic Fiber Optic Adapter, Female to Female #22322

★★★★★ 67 Reviews

0 Question

[Get a Quote](#)

[Request Stock](#)

**CA\$ 0.88**

FS P/N: AD-FCA-SCA-SM-SXP-FS

[653 In Stock, U.S. Warehouse](#) ⓘ

Deliver to [Canada](#)

Free Shipping on orders over CA\$ 105

Get it by Thu, Dec. 20 ▾



## 10m (33ft) LC APC to LC APC Simplex 2.0mm PVC (OFNR) 9/125 Single Mode Fiber Patch Cable #41577



621 Reviews

0 Question

[Get a Quote](#)[Request Stock](#)**CA\$ 3.50**

FS P/N: SM-LCA-LCA-SX-FS-10M-PVC

Length:

[1m](#)[2m](#)[3m](#)[5m](#)[7m](#)[10m](#)[15m](#)[Customized](#)

Size:

[1 piece](#)[80 pcs/case](#)



[Click to open expanded view](#)

## LC Female to ST Male Simplex Singlemode Fiber Optic Adapter #12084

★★★★★ 14 Reviews

1 Question

[Get a Quote](#)

[Request Stock](#)

**CA\$ 15.00**

FS P/N: AD-LCF-STM-SM-FS

[837 In Stock, U.S. Warehouse](#) ⓘ

Deliver to [Canada](#)

**Free Shipping on orders over CA\$ 105**

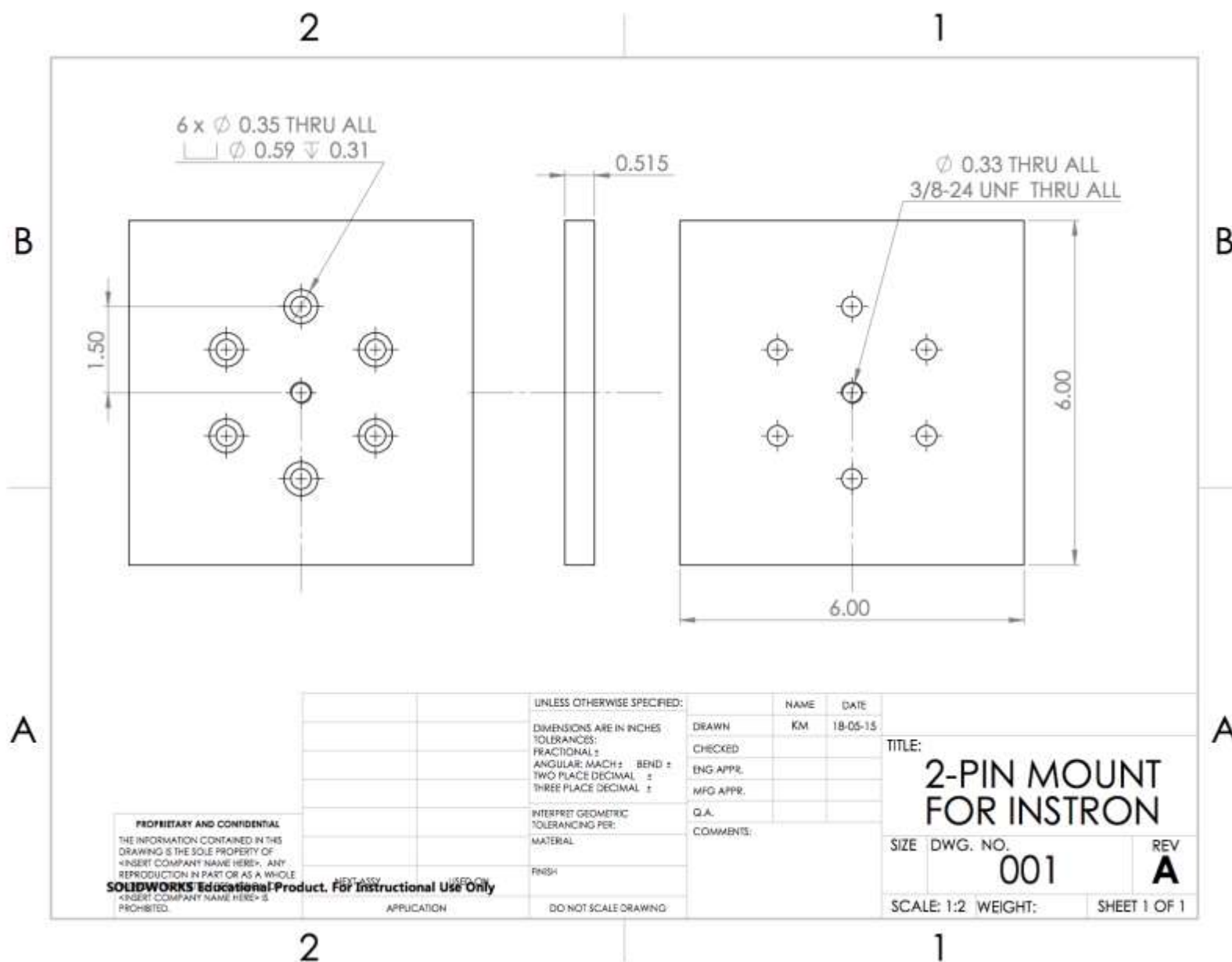
Get it by Thu, Dec. 20 ▾

Qty:

1



 [Add to Cart](#)



## Appendix B Nucleus-Annulus Boundary MATLAB script

```
% Kelsey McGivern
% Semi-automated segmentation of the nucleus - lumbar intervertebral disc
% March, 2018
%%%%%%%%%%%%%%%%%%%%%%%%%%%%%%%%%%%%%%%%%%%%%%%%%%%%%%%%%%%%%%%%%%%%%%%%

%% Read in the MRI scan as an NRRD file
pathname = 'C:\Users\kmcgiver\Google Drive\UBC\BMEG 599 Thesis\protocol
development\Testing sessions\Jan-19-18.Ox.Bending\nrrd';
% filename='25 P1 RARE_8_bas_hi-res.nrrd';
filename='26 ADC.nrrd';
fullpath = [pathname filesep filename];
data=nrrdread(fullpath);
bndry_cords=zeros(4,1); %array to store coordinates of boundary points
%% Plot the MRI scan on a new figure
figure (1); I=imagesc(data.pixelData(:,:,2)); %note that this will plot the
middle slice of the ADC scan (3 obtained in the sequence)
Img=data.pixelData(:,:,2); %image data needs to be stored in this array to
use improfile function later on
colormap('gray');

% define centroid of the disc from 2 intersecting lines
% NOTE: Draw the 1ST line through the LONG axis of the disc; 2ND line through
SHORT axis
centroid=zeros(2,1);
[cx, cy, c, xi, yi] = improfile;
[cx2, cy2, c2, xi2, yi2] = improfile;
csize=size(cx);
csize2=size(cx2);
flag=0;
for m=1:csize2(1)
    for n=1:csize(1)
        if abs(cx(n)-cx2(m))<=0.5 && abs(cy(n)-cy2(m))<=0.5
            centroid(1)=(cx(n)+cx2(m))/2;
            centroid(2)=(cy(n)+cy2(m))/2;
            flag=1;
            break
        end
    end
    if(flag==1)
        break
    end
end
display(centroid);

%% draw lines, rotating about centroid
% n_lines=6;
prompt = 'How many lines to define boundary?';
dlg_title='# Lines';
num_lines=1;
defaultans={'6'};
thres=inputdlg(prompt,dlg_title,num_lines,defaultans);
```

```

        n_lines=double(str2num(thres{:}));
alpha=pi/n_lines;
multiplier_startpt=zeros(2,n_lines); multiplier_endpt=zeros(2,n_lines);
x_lnpts=zeros(2,n_lines); y_lnpts=zeros(2,n_lines);
length=csize(1)+10;

for loop=1:n_lines
    multiplier_startpt(1,loop)=cos(alpha*(n_lines+1-loop));
    multiplier_startpt(2,loop)=-sin(alpha*(n_lines+1-loop));
    multiplier_endpt(1,loop)=cos(alpha*(loop-1));
    multiplier_endpt(2,loop)=sin(alpha*(loop-1));
end

for loop=1:n_lines
x_lnpts(1,loop)=centroid(1)+length*multiplier_startpt(1,loop);
x_lnpts(2,loop)=centroid(1)+length*multiplier_endpt(1,loop);
y_lnpts(1,loop)=centroid(2)+length*multiplier_startpt(2,loop);
y_lnpts(2,loop)=centroid(2)+length*multiplier_endpt(2,loop);
end

%% Create lines for segmentation process
for loop=1:n_lines
    xj=x_lnpts(:,loop)'; yj=y_lnpts(:,loop)';
    [cx, cy, c, xi, yi] = improfile(Img,xj,yj); %On figure, define line
profile you want to look at
    %cx, cy = nx1 array with x,y-coordinate of line (in IMAGE reference
frame)
    %c = nx1 array with image intensity value of the pixels the line
intersects (in LINE reference frame, i.e. x=1 to n)
    %xi, yi = 2x1 array with x,y-coordinate of start and endpoint of the
line
    csize=size(cx);
    figure(2); plot(c); %this plots the intensity values of the line that
was drawn above

    %% USE THIS TO CALCULATE BOUNDARY BASED ON A DEFINED THRESHOLD VALUE
    %Define threshold; set value below, or use prompt window.
    threshold=0.00125; %%USE THIS FOR ADC MAPS
%       threshold=1.40*10^4; %% USE THIS FOR T2 HI_RES_BAS SCANS
%       prompt = 'What is the boundary threshold value?';
%       dlg_title='Threshold Input';
%       num_lines=1;
%       defaultans={'0.00125'};
%       thres=inputdlg(prompt,dlg_title,num_lines,defaultans);
%       threshold=double(str2num(thres{:}));
%% USE THIS TO CALCULATE BOUNDARY FROM GAUSSIAN DIST
%       bound_dist=fitdist(c, 'Normal');
%       ybnds=pdf(bound_dist,cx);
%       mu=mean(bound_dist);
%       fWHM=2*sqrt(2*ln(2))*mu;
%       c_val(1)=mu-FWHM/2;
%       c_val(2)=mu+FWHM/2;
%       % plot(cx,ybnds,'LineWidth',2);

```



```

%% test
c_val=zeros(2,1);
x=int32(csize(1)/2); % annulus should be at least 3 pixels in width, so
only start searching at boundary

%search along line until the pixel intensity exceeds threshold
while x>0
    if c(x) < threshold
        c_val(1)=x+1;
        break
    end
    x=x-1;
end

%continue searching along line from the same point for when intensity
drops back below threshold
y=int32(csize(1)/2);
while y<=(csize(1))
    if c(y) < threshold
        c_val(2)=y-1;
        break
    end
    y=y+1;
end

%% USE THIS FOR MANUAL INPUT OF THE BOUNDARY POINTS. TYPE X VALUE ALONG
LINE INTO DIALOGUE BOX
% x = inputdlg('Enter space-separated numbers for boundary points along C:
Example: "17 54"',...
%         'Sample', [1 62]);
% c_val = str2num(x{:});

%% Record the coordinates of the determined boundary points into an array
addcol1= [cx(c_val(1)); cy(c_val(1)); 1; 1]; %first point to add to array
addcol2= [cx(c_val(2)); cy(c_val(2)); 1; 1]; %second point to add
bndry_cords = [bndry_cords addcol1 addcol2]; %append coordinates to
variable
close(figure(2));
end
%% plot the define boundary coordinates on the MRI scan
bndry_cords(:,1)=[]; %removes the (0,0) point from the matrix
figure(1); hold on; plot(bndry_cords(1,:),bndry_cords(2,:), 'o',
'MarkerSize', 5, 'MarkerEdgeColor','b');
% [x, y] = ginput;
% spcv = cscvn( [x, y].' );
% fnplt( spcv );

%% Draw spline connecting the defined boundary coordinates
x=bndry_cords(1,:);
y=bndry_cords(2,:);

% this re-orders the x and y coordinates so it samples the points cw around

```

```

the disc,
% instead of jumping from one side of the disc to the other then back again
x_odd = x(1:2:end,:); % odd matrix
x_even = x(2:2:end,:); % even matrix
x_new= [x_odd' x_even' x_odd(1)]'; % reorder in odd, even, connecting to
first odd point again to close the loop

y_odd = y(1:2:end,:);
y_even = y(2:2:end,:);
y_new= [y_odd' y_even' y_odd(1)]';

spcv = cscvn( [x_new, y_new].' );
fnplt( spcv );
%% Save boundary locations to text file to input into slicer as fiducial
markers
fileID = fopen('fiducial marker locations.txt','w');
fprintf(fileID, '%f %f\n', bndry_cords(:, :));
fclose(fileID);

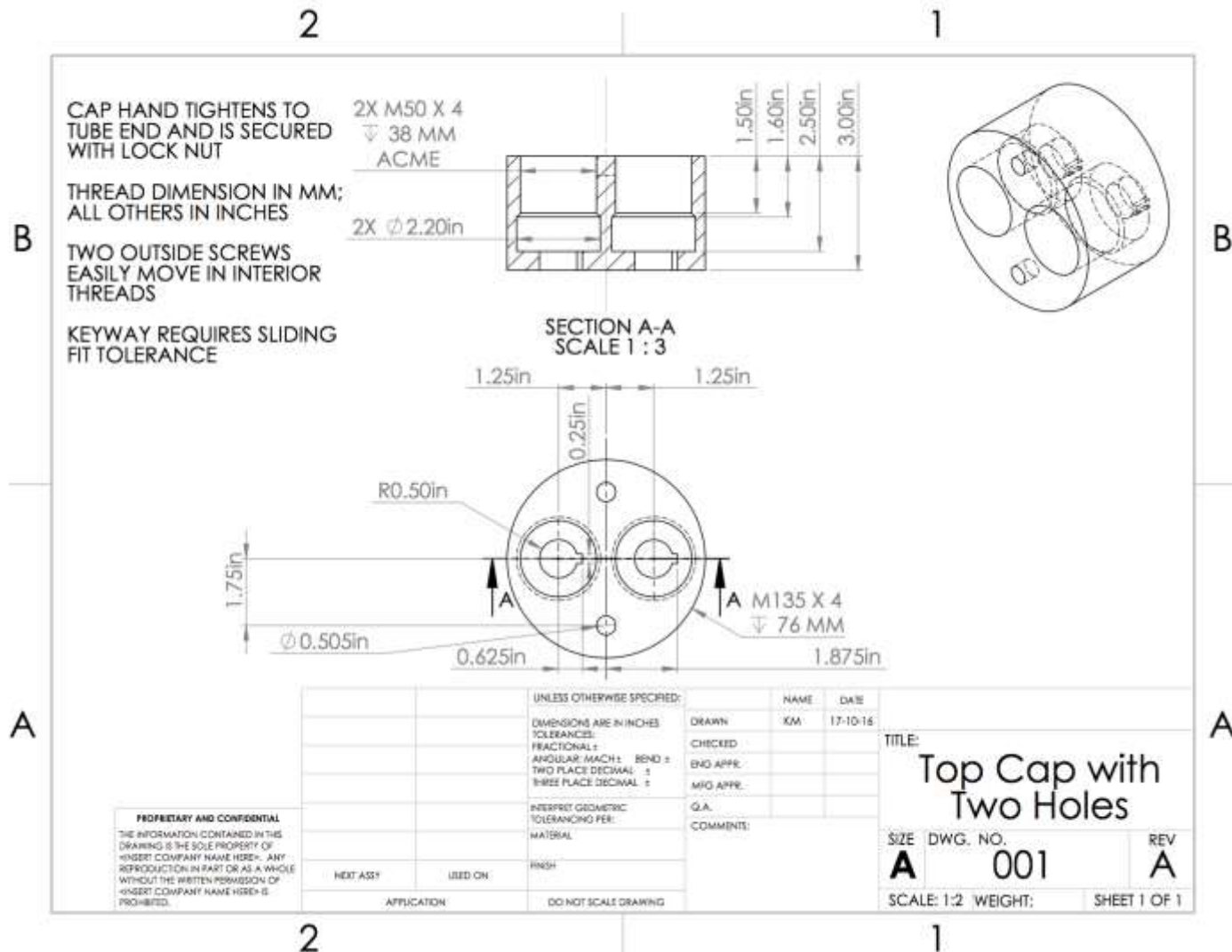
%% Save boundary locations to text file **IN RAS COORDINATES
ijktoras=[-0.5312 -0.3283 -0.0643 55.3396; 0.3277 -0.5319 0.0463 12.8248;
-0.0329 0.0023 1.4979 -5.8568; 0 0 0 1];
RAS_cords=zeros(4,n_lines*2);
for x=1:n_lines*2
    RAS_cords(:,x)=ijktoras*bndry_cords(:,x);
end

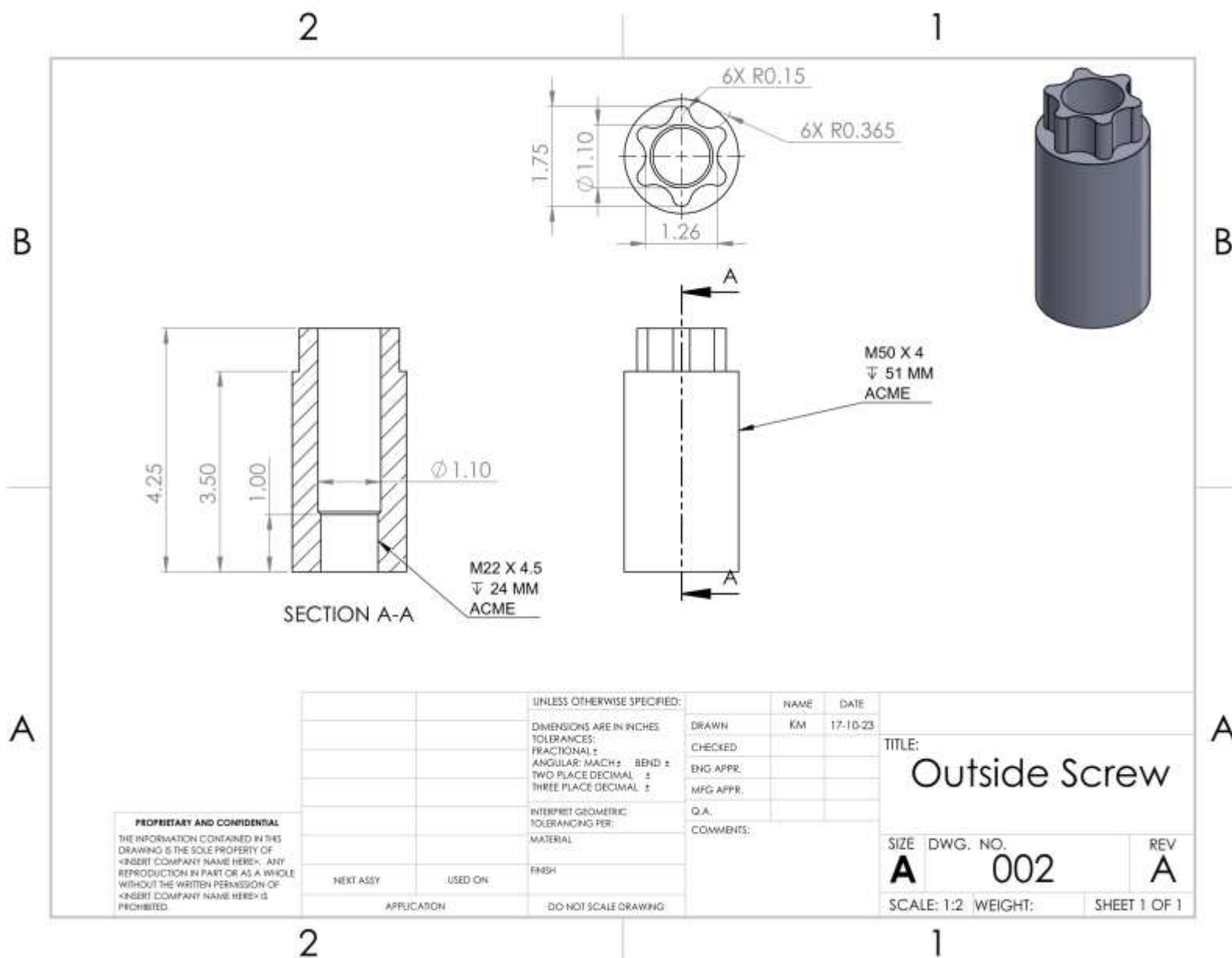
fileID = fopen('yx-RAS marker locations.txt','w');
for x=1:n_lines*2
    fprintf(fileID, 'slicer.modules.markups.logic().AddFiducial(%f, %f, %f)
\n', RAS_cords(2,x), RAS_cords(1,x), RAS_cords(3,x));
end
fclose(fileID);

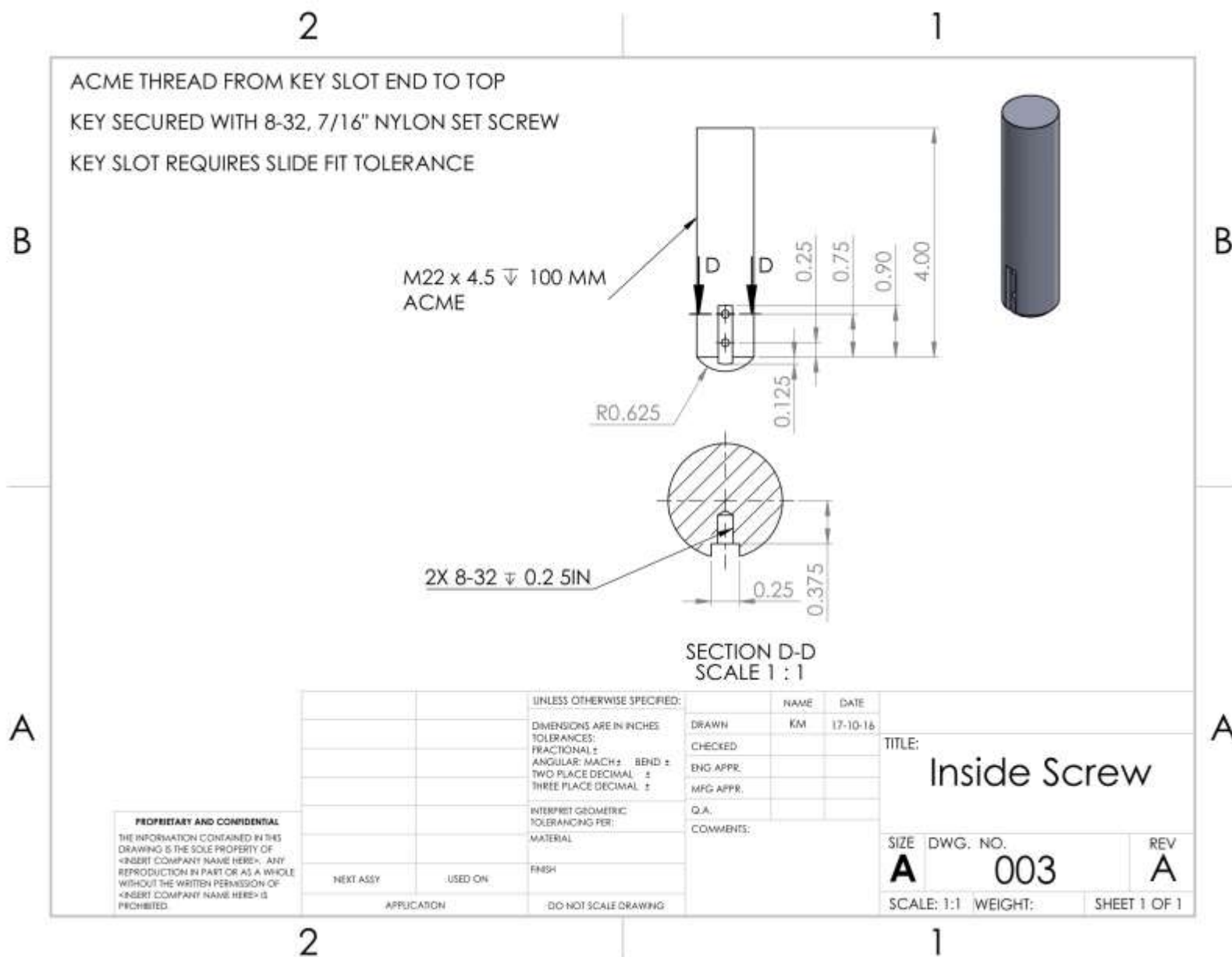
fileID = fopen('xy-RAS marker locations.txt','w');
for x=1:n_lines*2
    fprintf(fileID, 'slicer.modules.markups.logic().AddFiducial(%f, %f, %f)
\n', RAS_cords(1,x), RAS_cords(2,x), RAS_cords(3,x));
end
fclose(fileID);

```

## Appendix C Loading Rig Specification







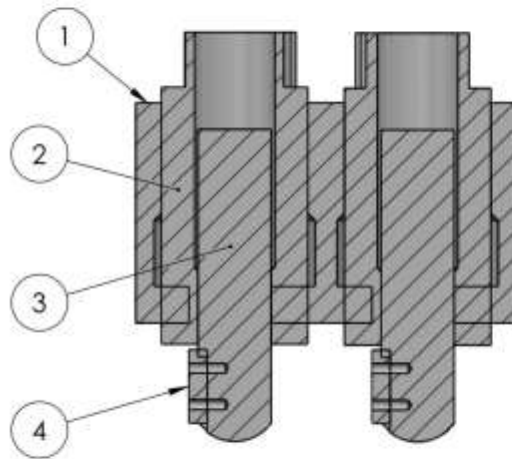
2

1

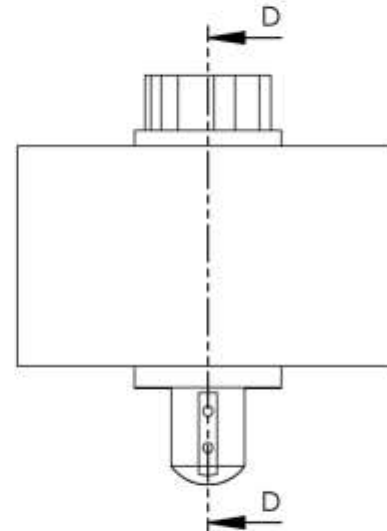
ITEM NO.	DESCRIPTION	MATERIAL	QTY.
1	Top Cap with 2 Holes	DELIN, 6" ROD	1
2	Outside Screw	DELIN, 2.5" ROD	2
3	Inside Screw	PEEK, 1" ROD	2
4	Key	DELIN, 0.5" SHEET	2

ALL RIGHT HAND THREADS

KEY FITS INSIDE SCREW AND  
SECURED WITH SET SCREW.  
SLIDES ON TOP CAP TO  
PREVENT ROTATION OF INSIDE  
SCREW.



SECTION D-D



**PROPRIETARY AND CONFIDENTIAL**  
THE INFORMATION CONTAINED IN THIS  
DRAWING IS THE SOLE PROPERTY OF  
<INSERT COMPANY NAME HERE>. ANY  
REPRODUCTION IN PART OR AS A WHOLE  
WITHOUT THE WRITTEN PERMISSION OF  
<INSERT COMPANY NAME HERE> IS  
PROHIBITED.

NEXT ASSY

USED ON

APPLICATION

UNLESS OTHERWISE SPECIFIED:

DIMENSIONS ARE IN INCHES  
TOLERANCES:  
FRACTIONAL ±  
ANGULAR: MACH ± BEND ±  
TWO PLACE DECIMAL ±  
THREE PLACE DECIMAL ±

INTERPRET GEOMETRIC  
TOLERANCING PER:  
MATERIAL

FINISH

DO NOT SCALE DRAWING

DRAWN

NAME

KM

DATE

17-10-16

CHECKED

ENG APPR.

MFG APPR.

Q.A.

COMMENTS:

TITLE:

# Differential Screw Assembly

SIZE

**A**

DWG. NO.

**004**

REV

**A**

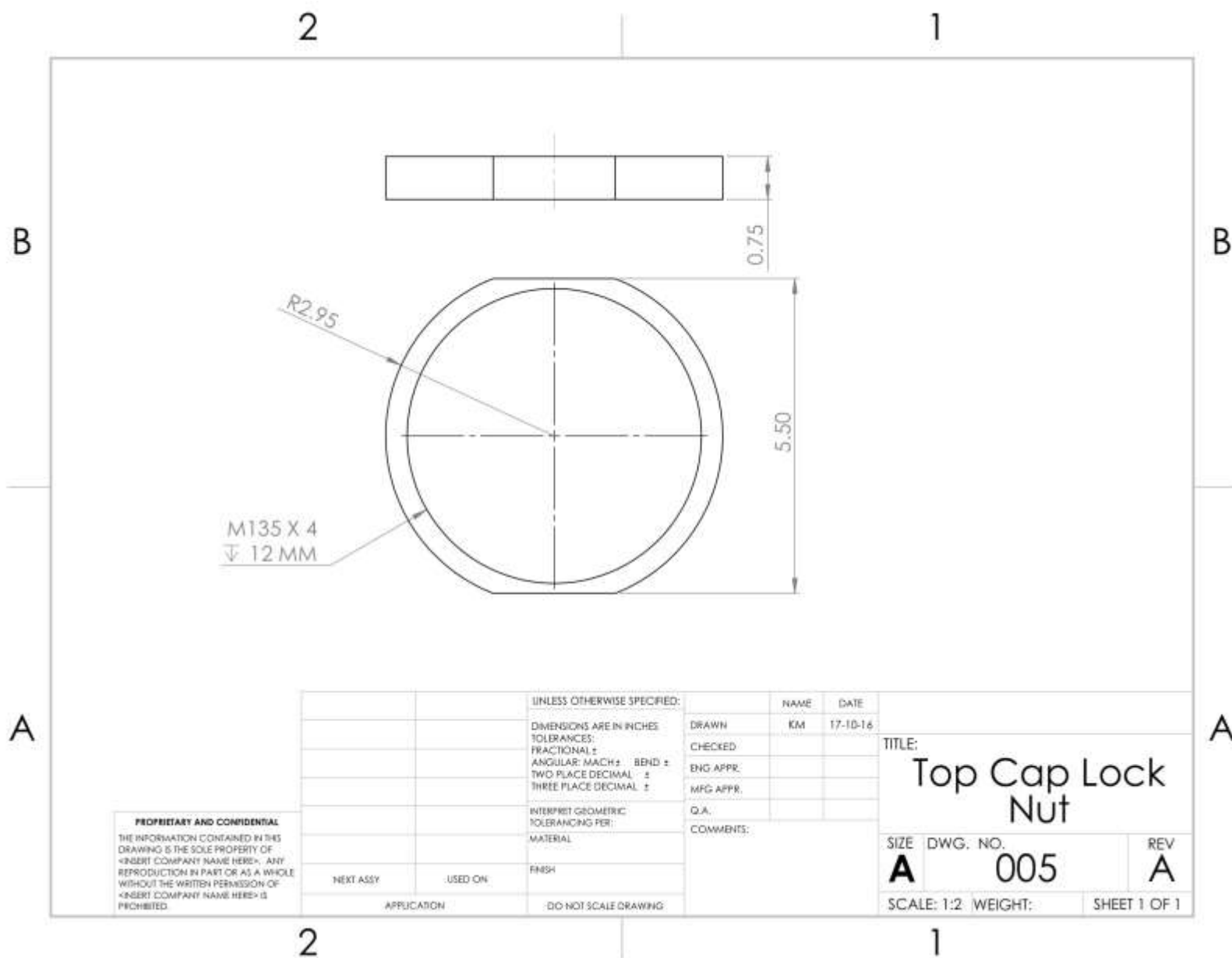
SCALE: 1:2

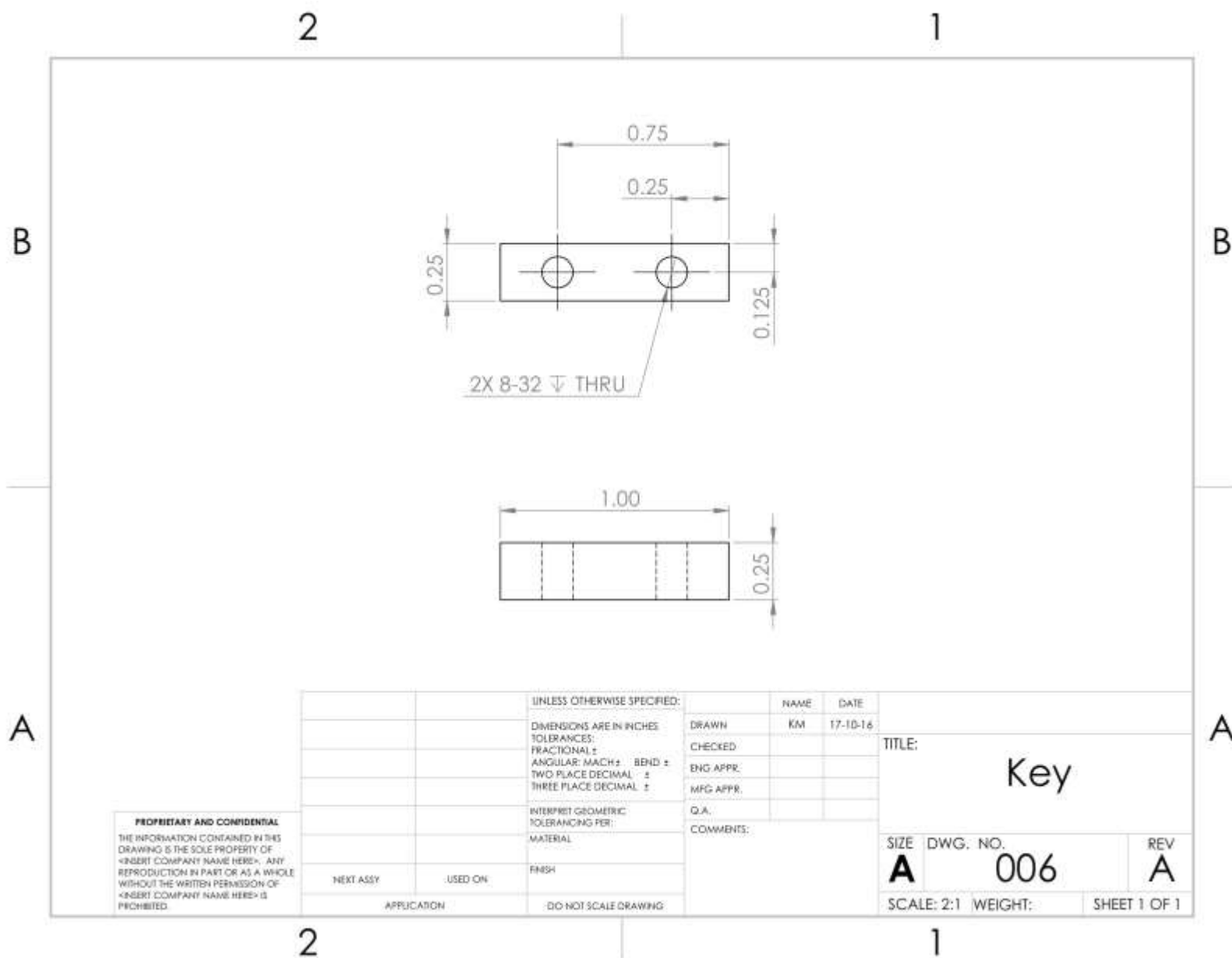
WEIGHT:

SHEET 1 OF 1

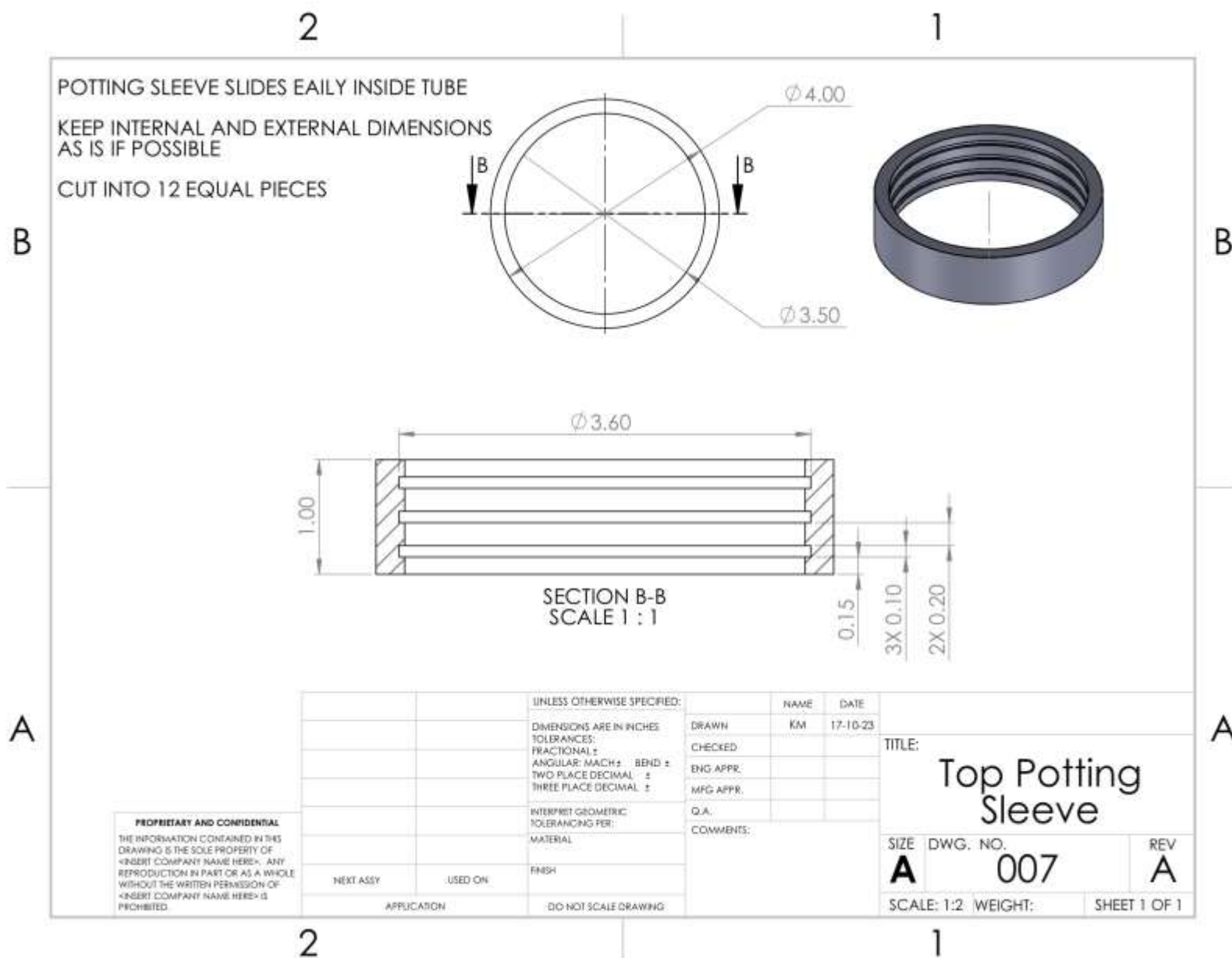
2

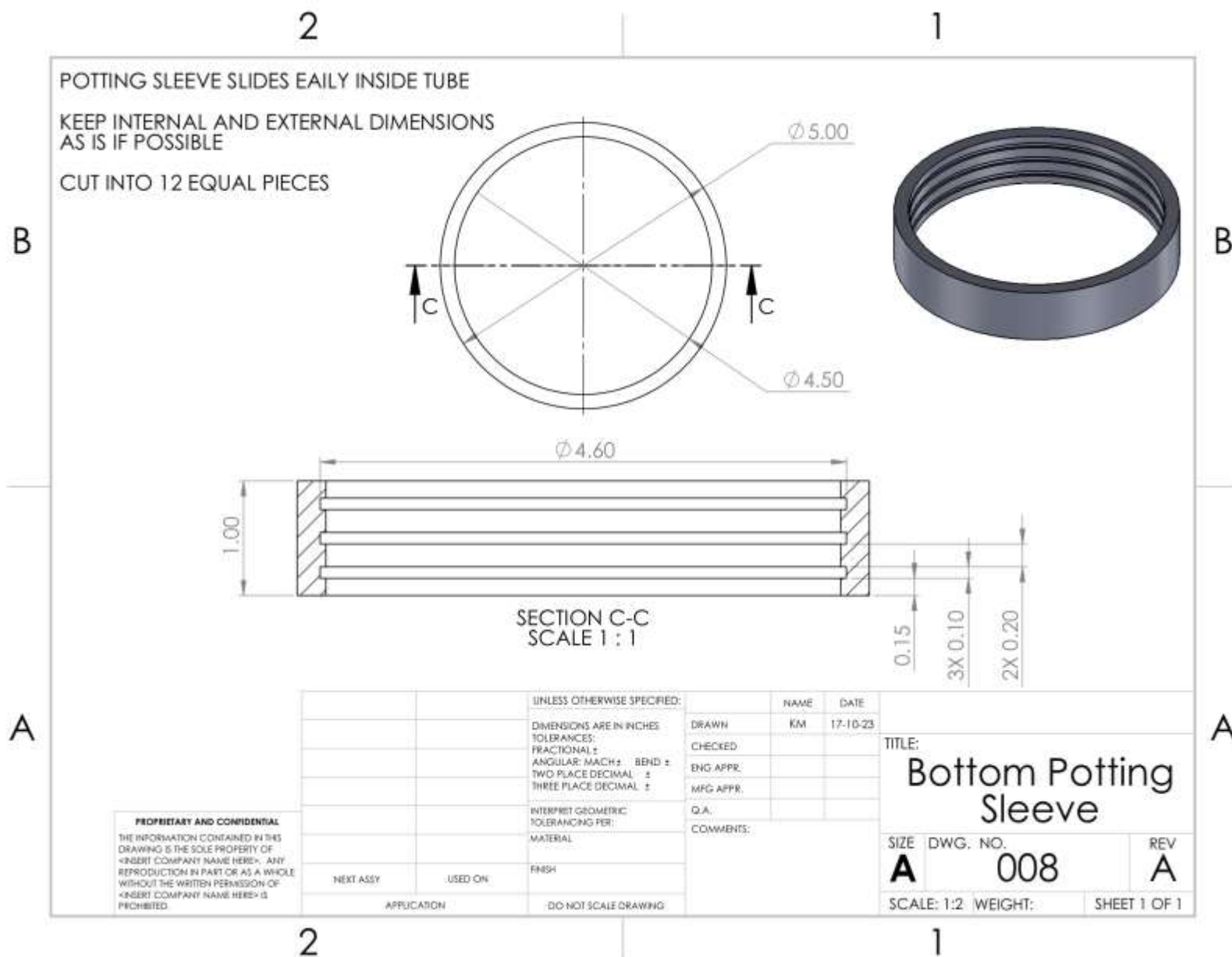
1

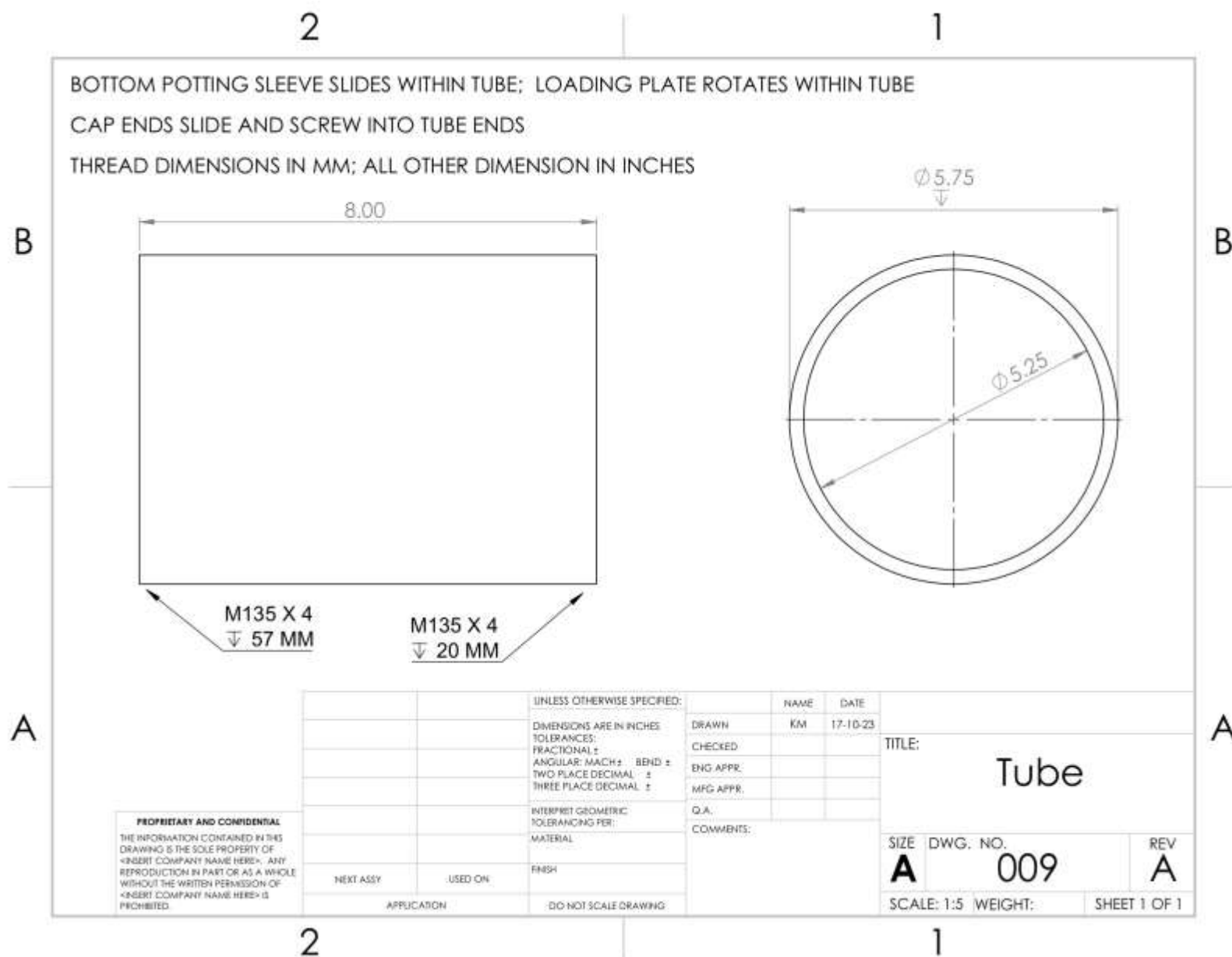


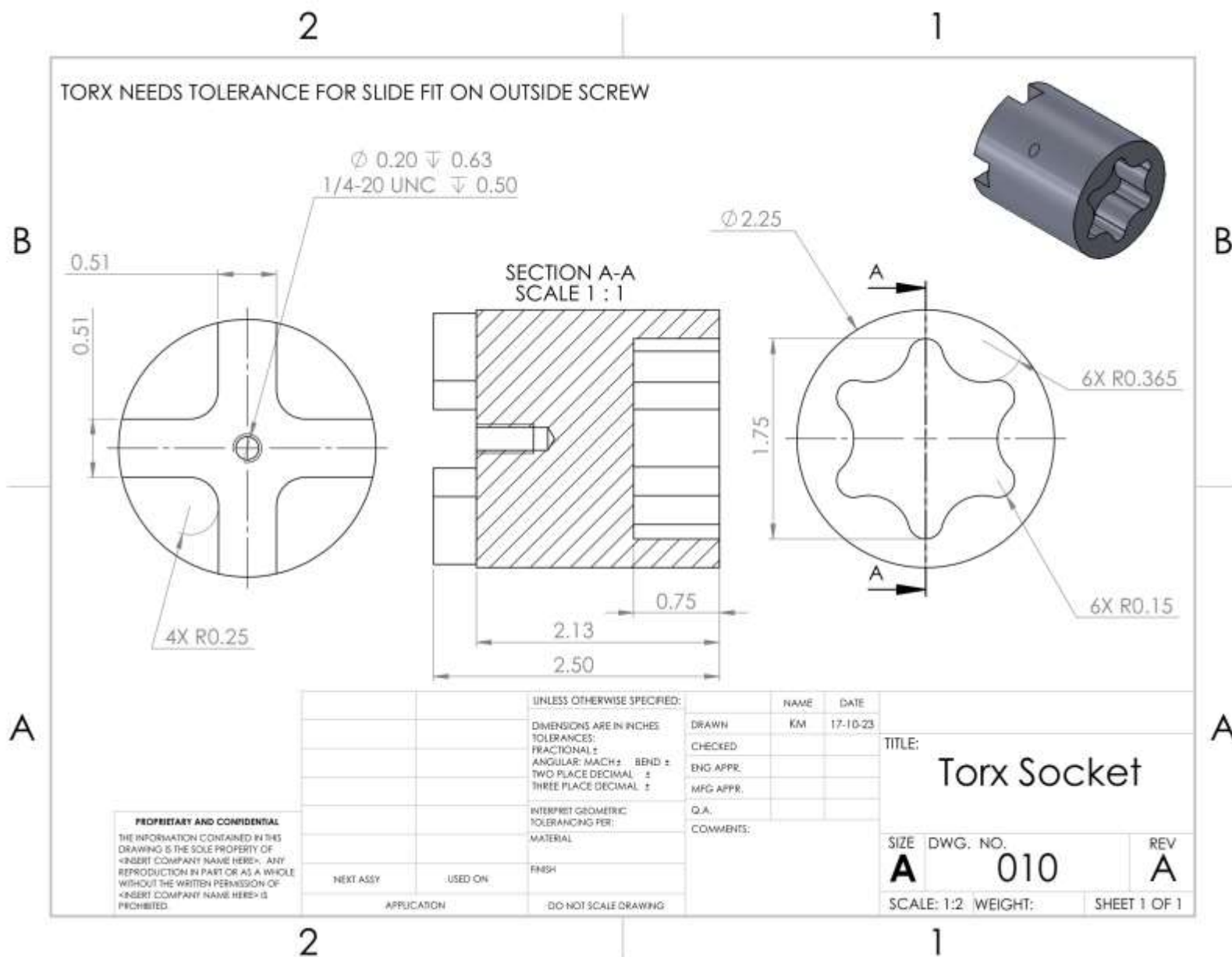


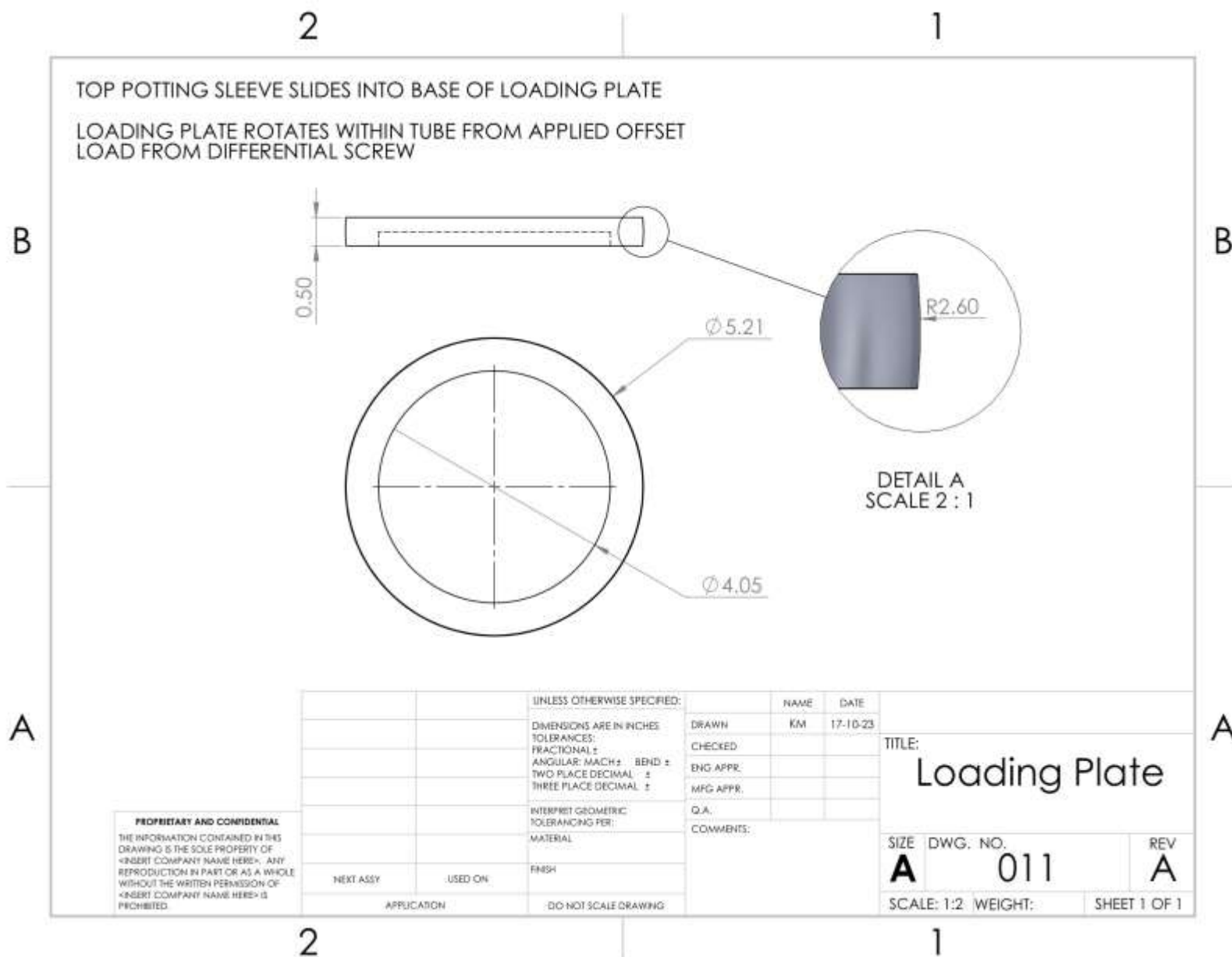


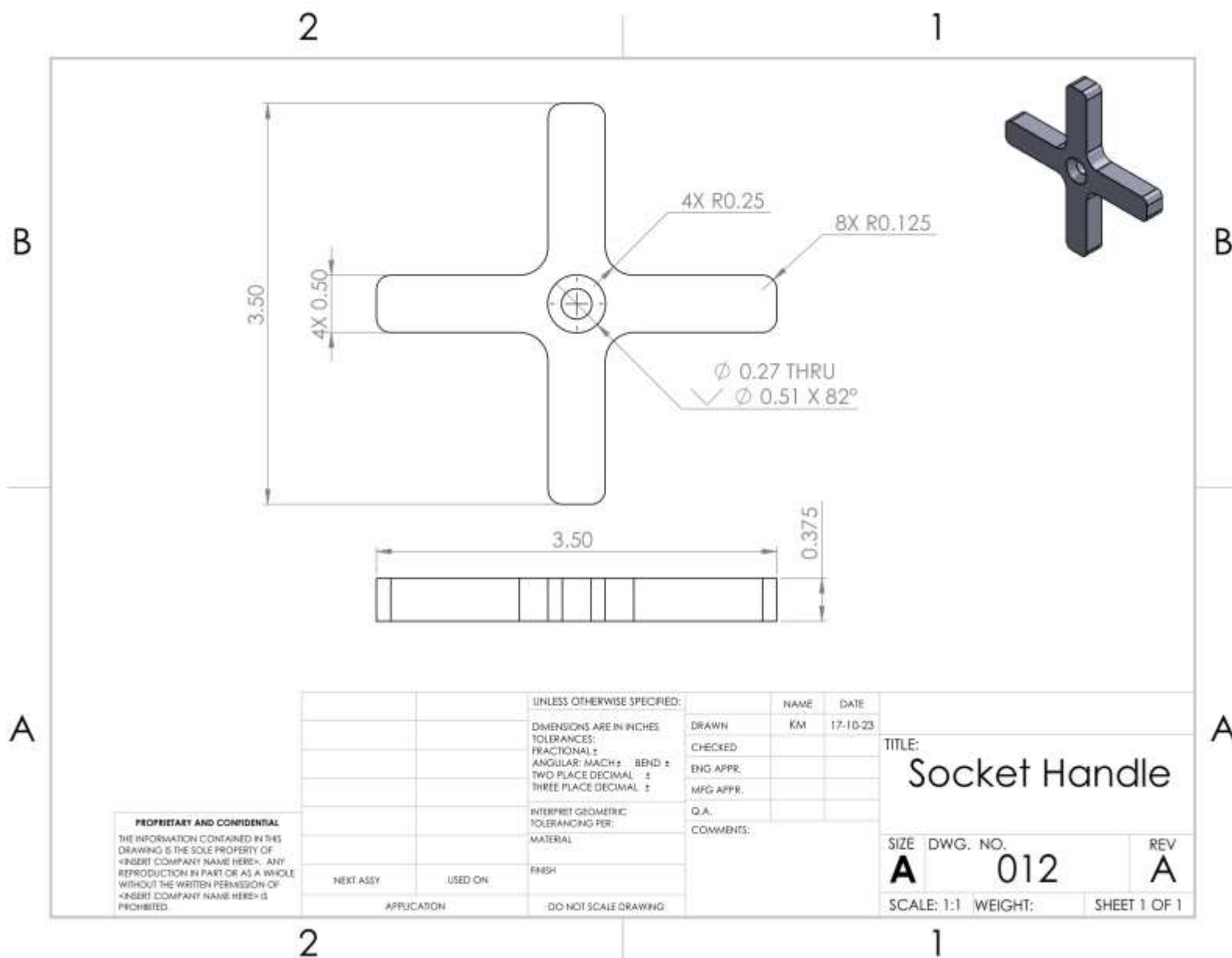








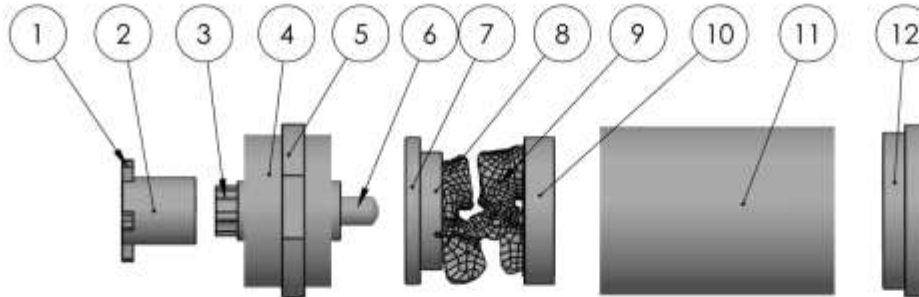




2

1

ITEM NO.	PART NUMBER	MATERIAL	DWG No.	QTY.
1	Socket handle	Delrin Sheet, 0.5" thick	012	1
2	Torx Socket	Delrin Rod, 2.5" Diameter	010	1
3	Outside Screw	Delrin Rod, 2.5" Diameter	002	2
4	Top Cap with 2 Holes	Delrin Rod, 6" Diameter	001	1
5	top cap nut	Delrin Rod, 6" Diameter	005	1
6	Inside Screw	Peek Rod, 1" Diameter	003	2
7	Loading Plate	Delrin Sheet, 0.5" thick	011	1
8	Top Potting Sleeve	Cast Acrylic Tube, 4" OD	007	1
9	Potted Spinal Unit	N/A	N/A	1
10	Bottom Potting Sleeve	Cast Acrylic Tube, 5" OD	008	1
11	Tube	Cast Acrylic Tube, 5.75" OD	009	1
12	Bottom Cap	Delrin Rod, 6" Diameter	013	1
13	inside screw key	Delrin Sheet, 0.5" thick	006	2



**PROPRIETARY AND CONFIDENTIAL**  
 THE INFORMATION CONTAINED IN THIS  
 DRAWING IS THE SOLE PROPERTY OF  
 <INSERT COMPANY NAME HERE>. ANY  
 REPRODUCTION IN PART OR AS A WHOLE  
 WITHOUT THE WRITTEN PERMISSION OF  
 <INSERT COMPANY NAME HERE> IS  
 PROHIBITED.

NEXT ASSY

USED ON

APPLICATION

UNLESS OTHERWISE SPECIFIED:

DIMENSIONS ARE IN INCHES  
 TOLERANCES:  
 FRACTIONAL ±  
 ANGULAR: MACH ± BEND ±  
 TWO PLACE DECIMAL ±  
 THREE PLACE DECIMAL ±

INTERPRET GEOMETRIC  
 TOLERANCING PER:  
 MATERIAL

FINISH

DO NOT SCALE DRAWING

NAME

KM

DATE

17-10-23

DRAWN

CHECKED

ENG APPR.

MFG APPR.

Q.A.

COMMENTS:

TITLE:

Full Rig Assembly

SIZE

A

DWG. NO.

014

REV

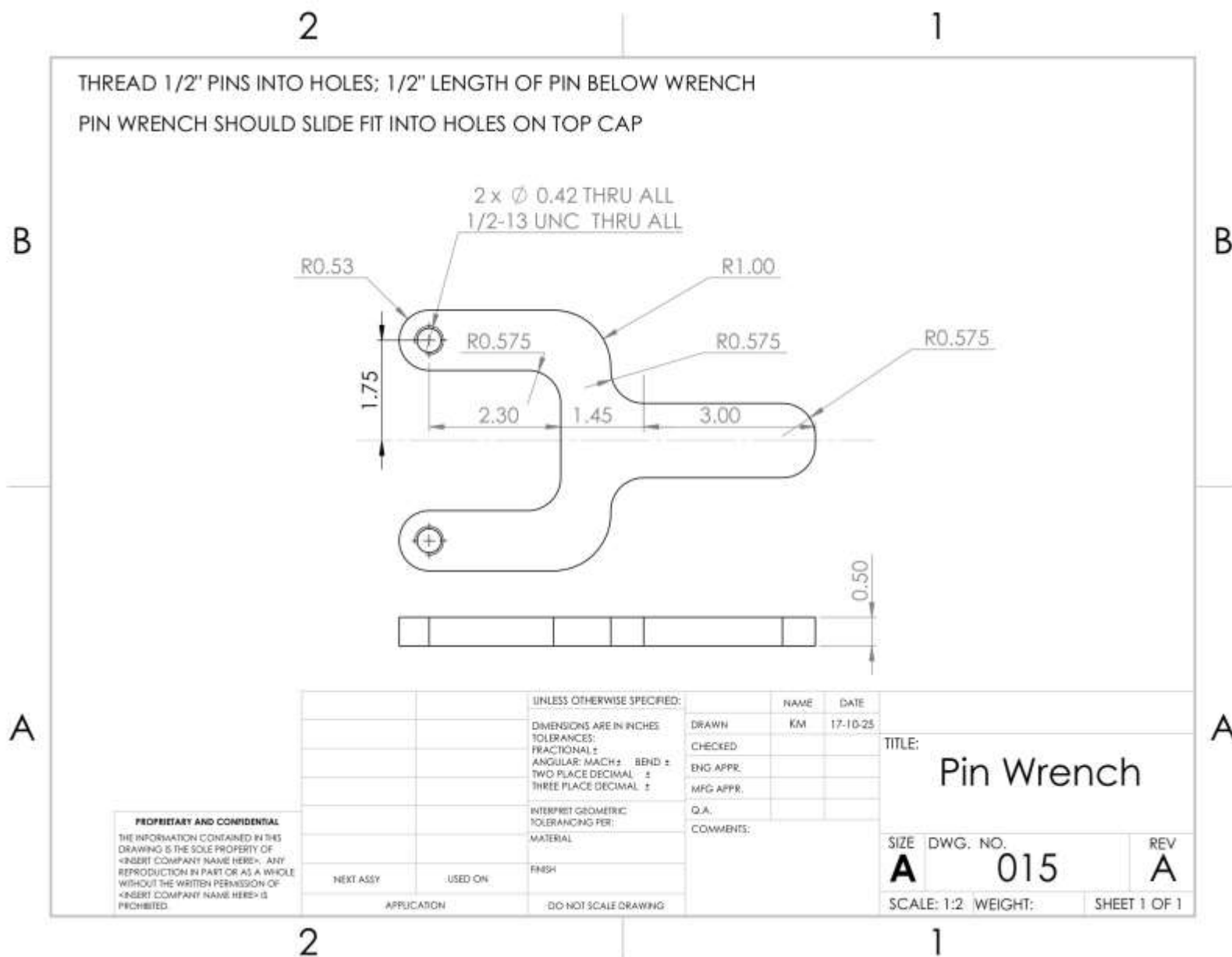
A

SCALE: 1:10 WEIGHT:

SHEET 1 OF 1

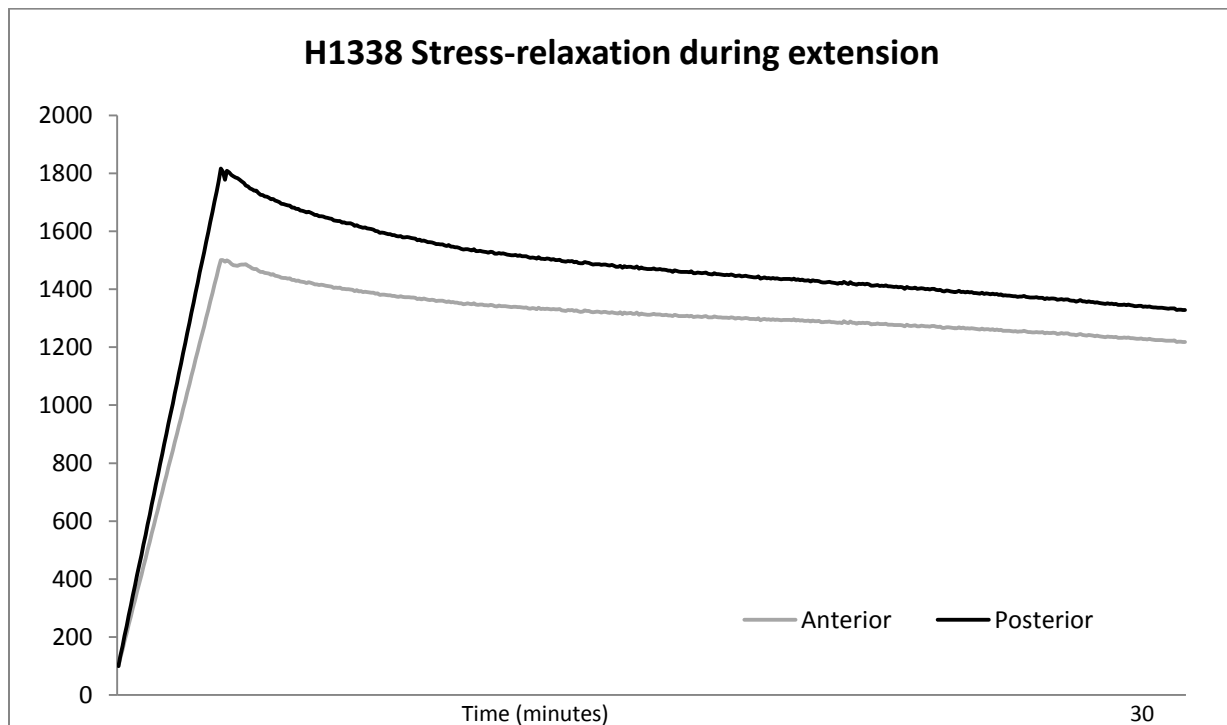
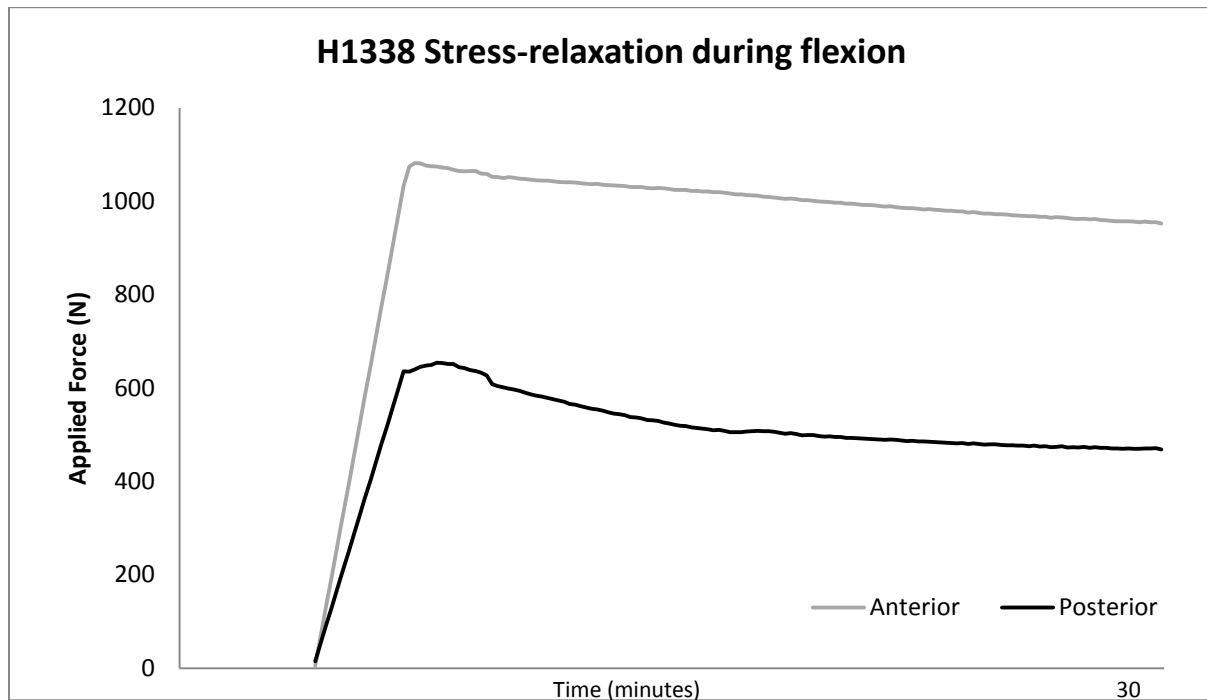
2

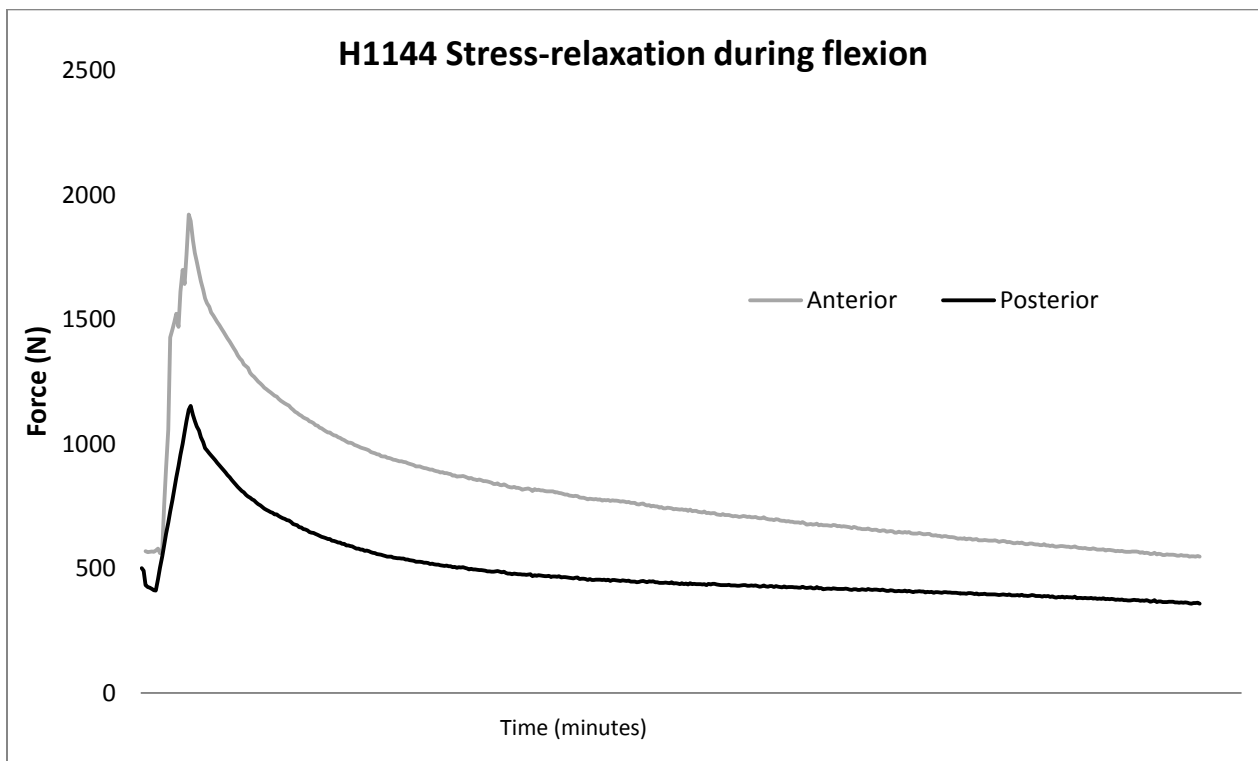
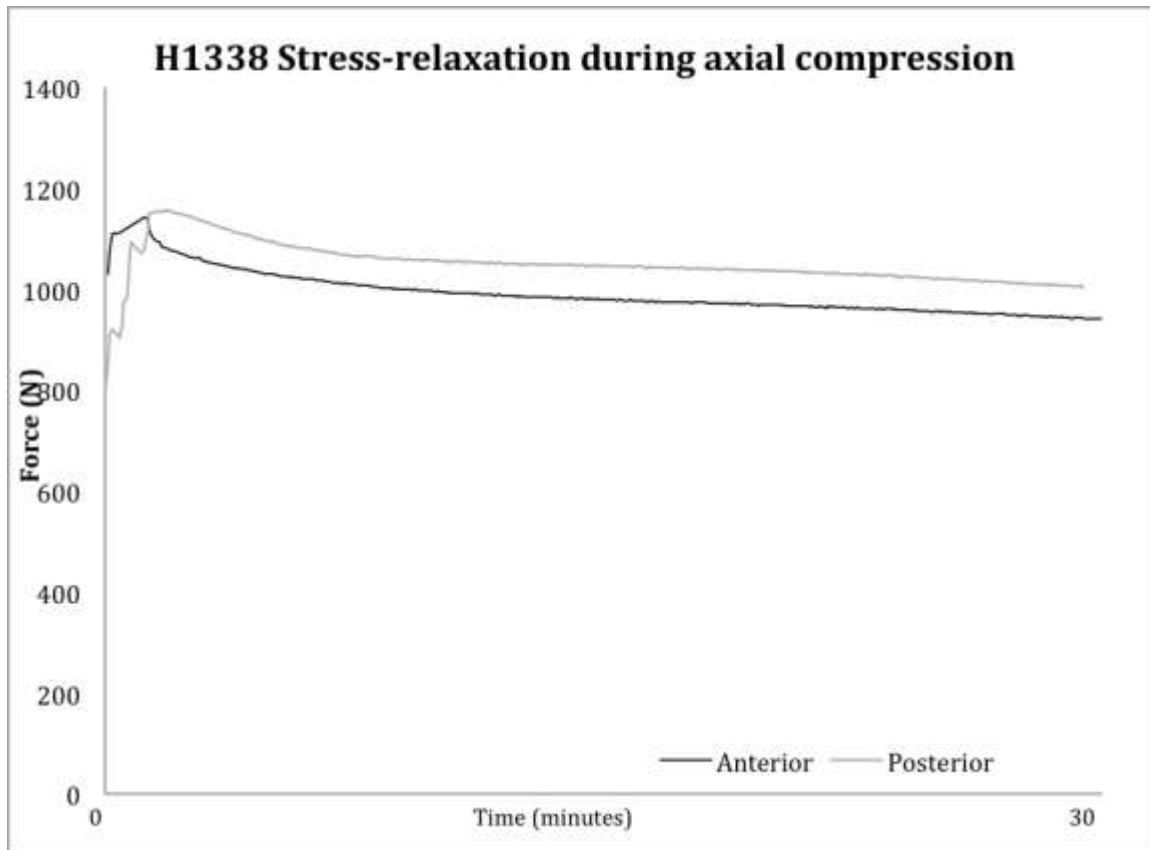
1

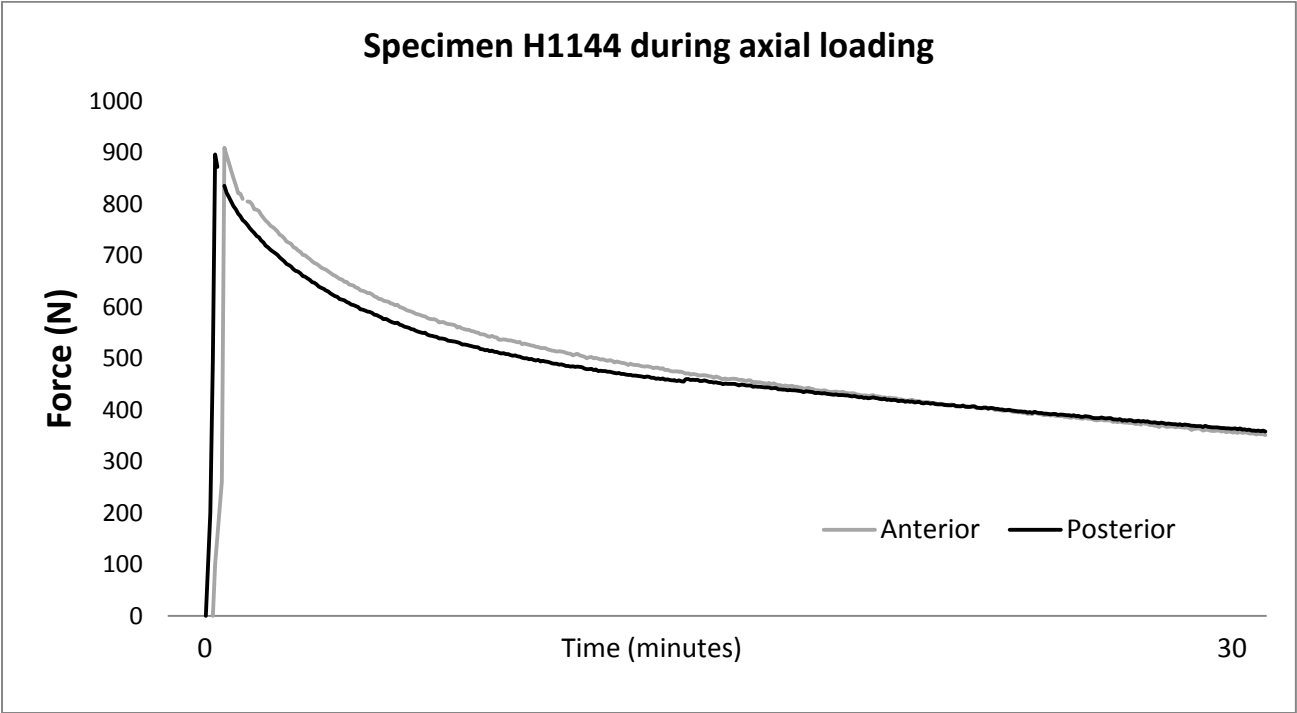
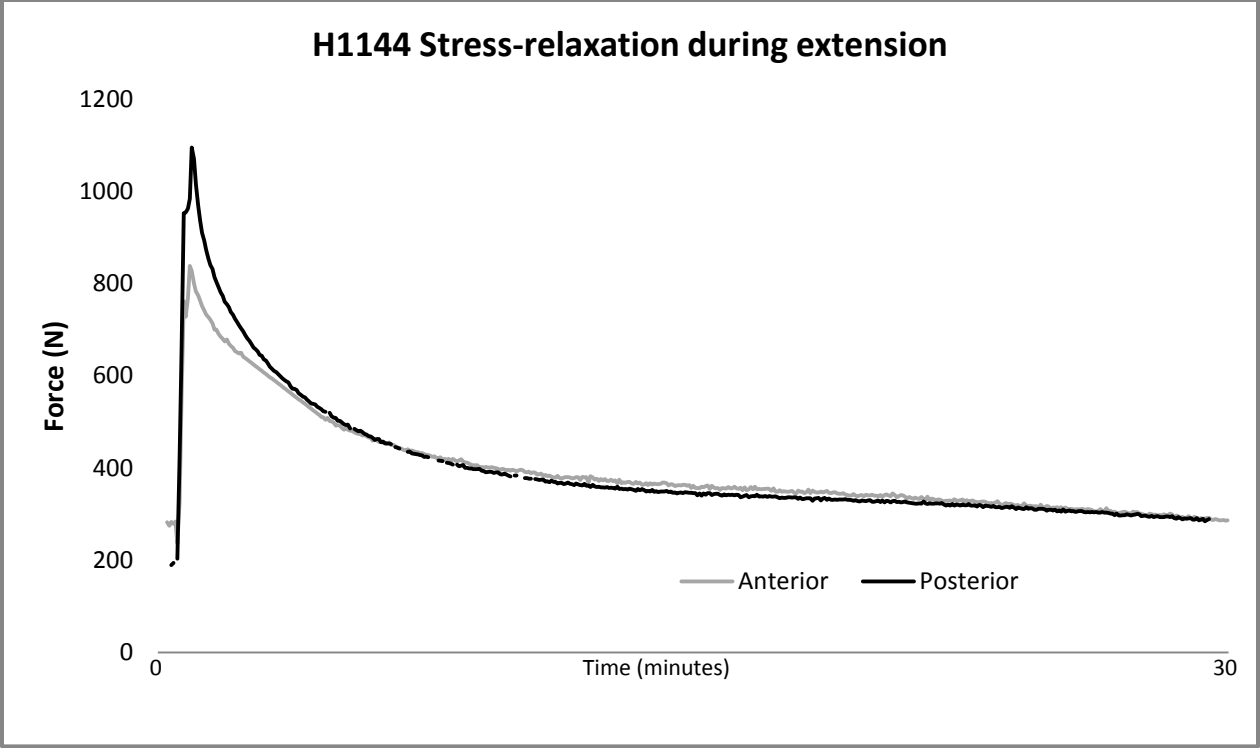


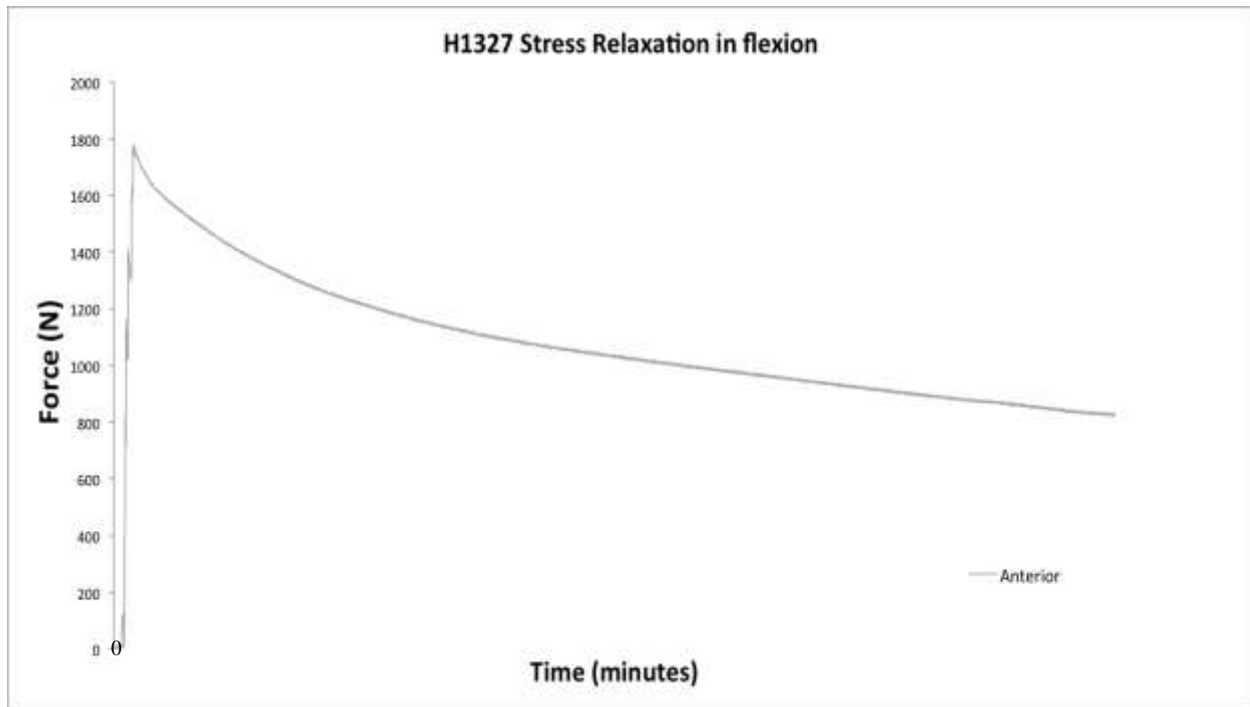


**Appendix D Stress-relaxation plots for loading of the functional spinal units in simulated relevant postures**









\*Note: only anterior data for specimen H1327 was collected; FBG-2 (on posterior side) was damaged during experiment setup and could not be repaired. Signal from FBG-1 cut out during the scans in extension and axial compression loading conditions and so data for these two loading conditions is unavailable. However testing proceeded for all loading conditions regardless of FBG issues in order to collect relevant data regarding ADC measurements and loading conditions to collect as much meaningful data from the prepared cadaveric specimen as possible.

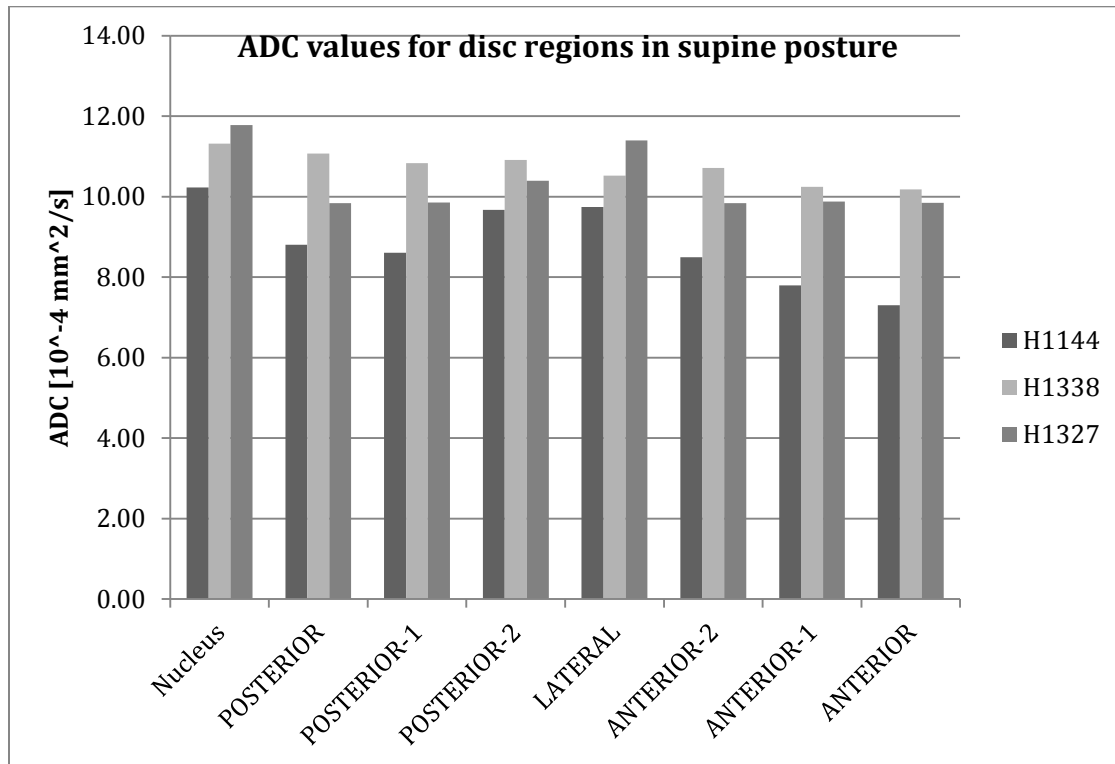
## Appendix E Additional and alternative data plots for loading simulating relevant postures

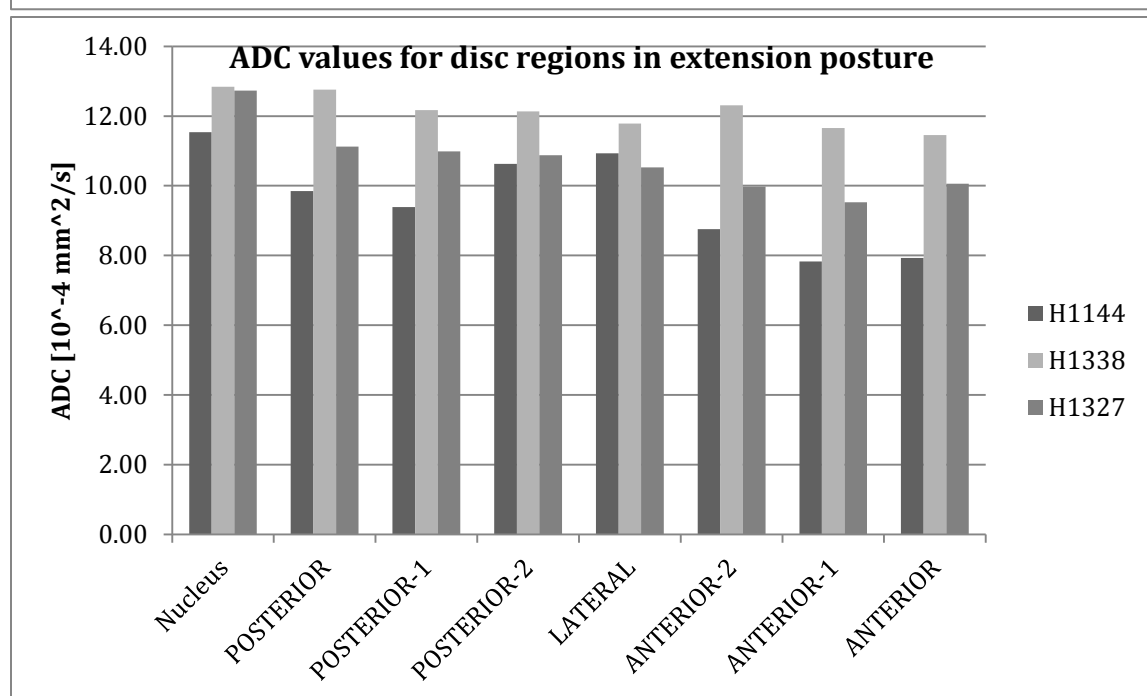
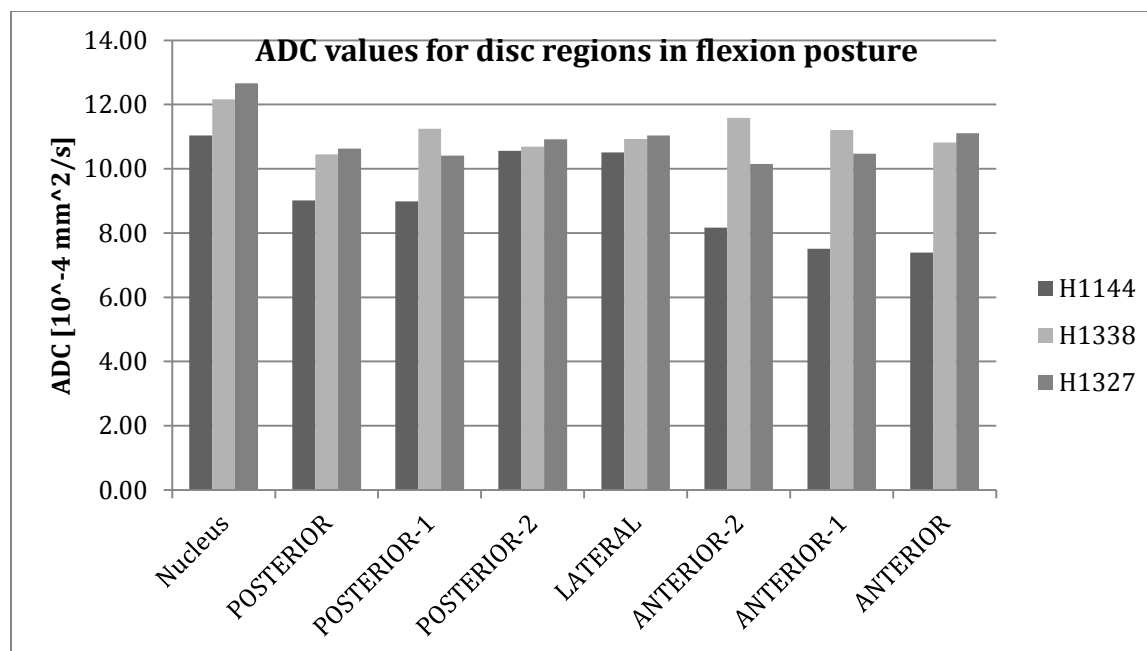
### E.1 Degree of rotation for postural loading

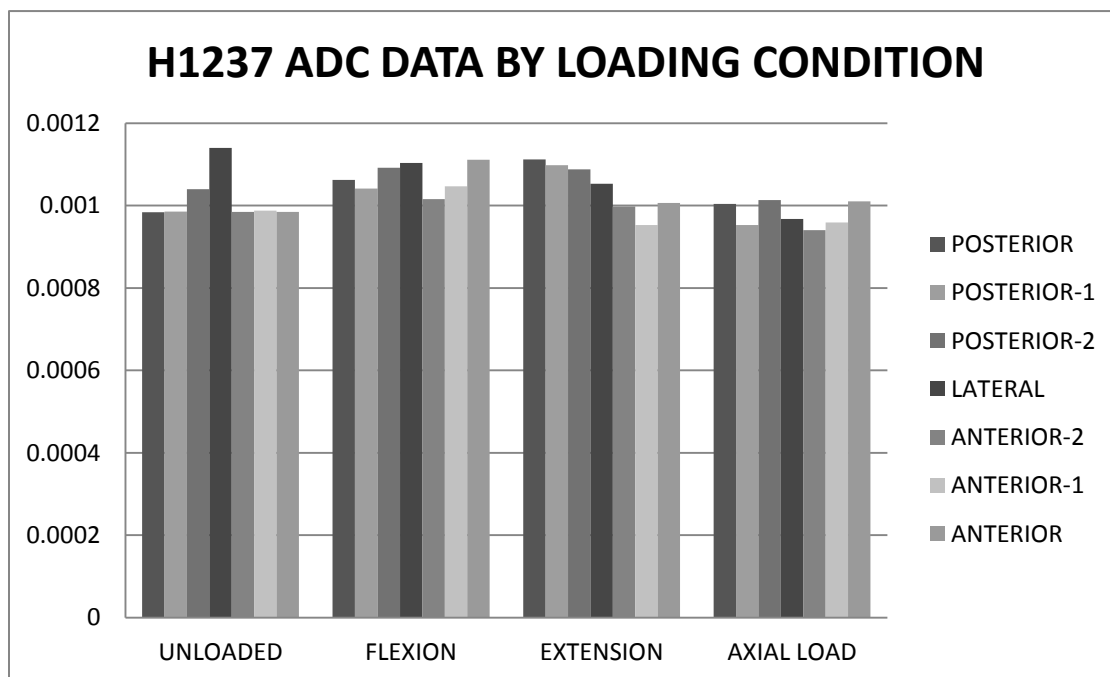
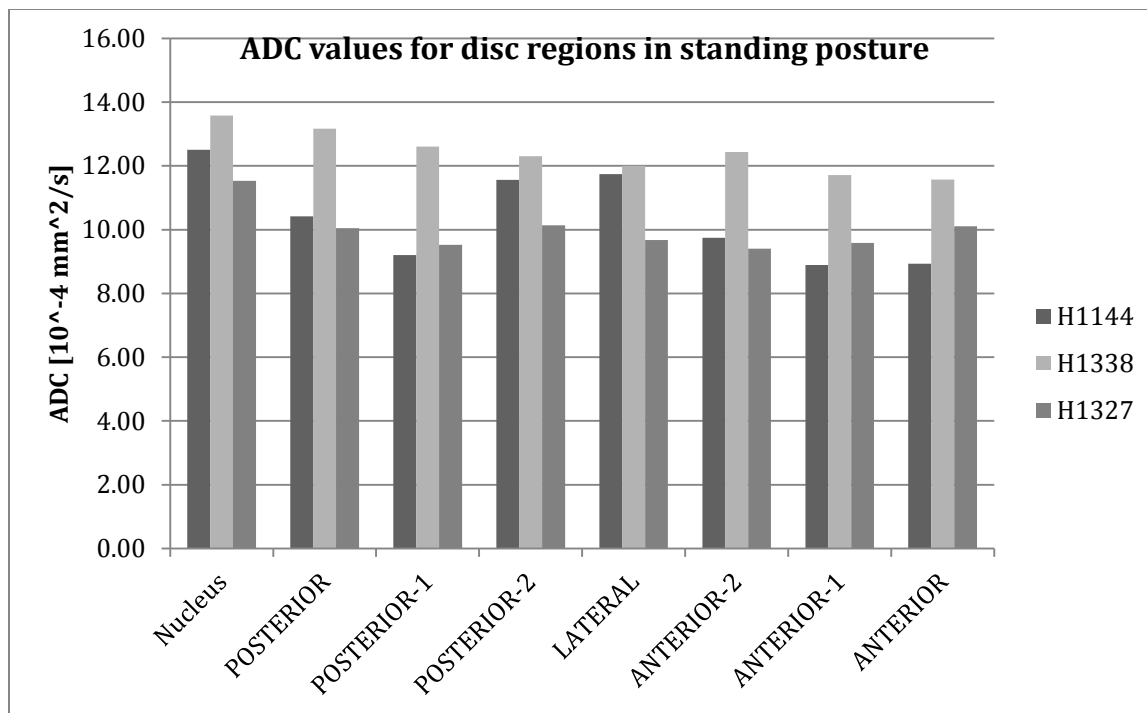
The degrees of rotation of each specimen during testing are shown in the table below.

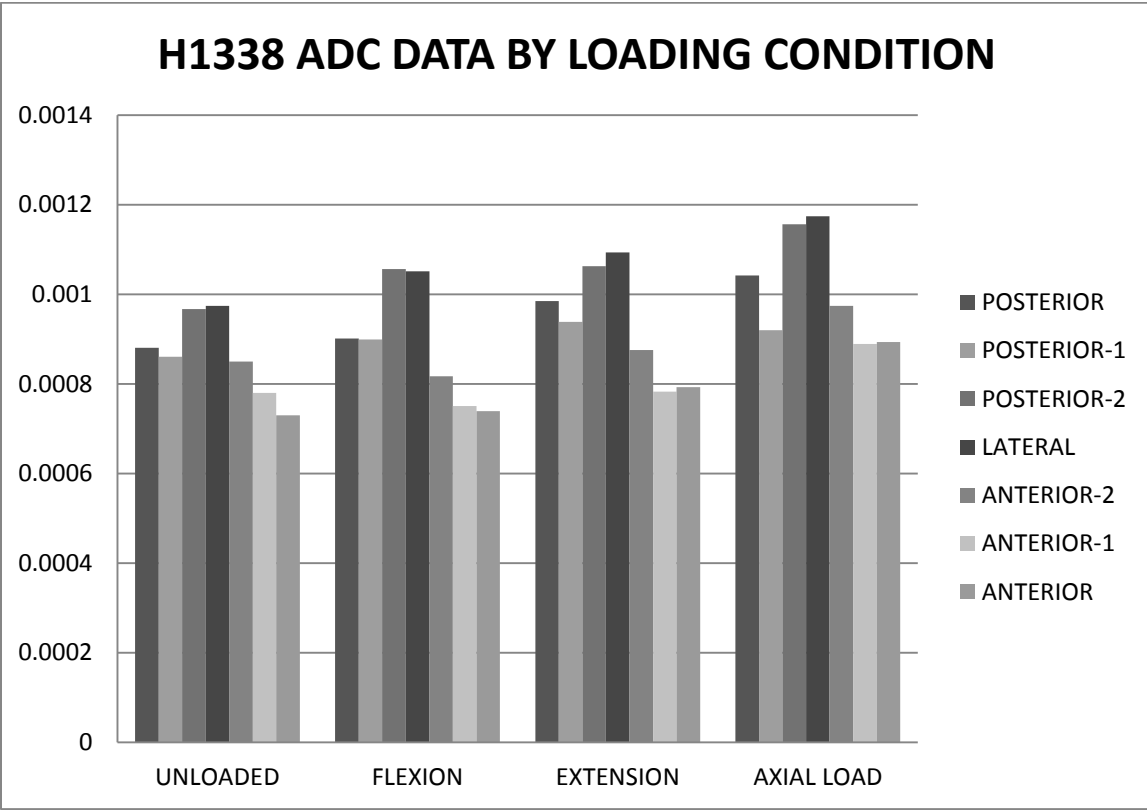
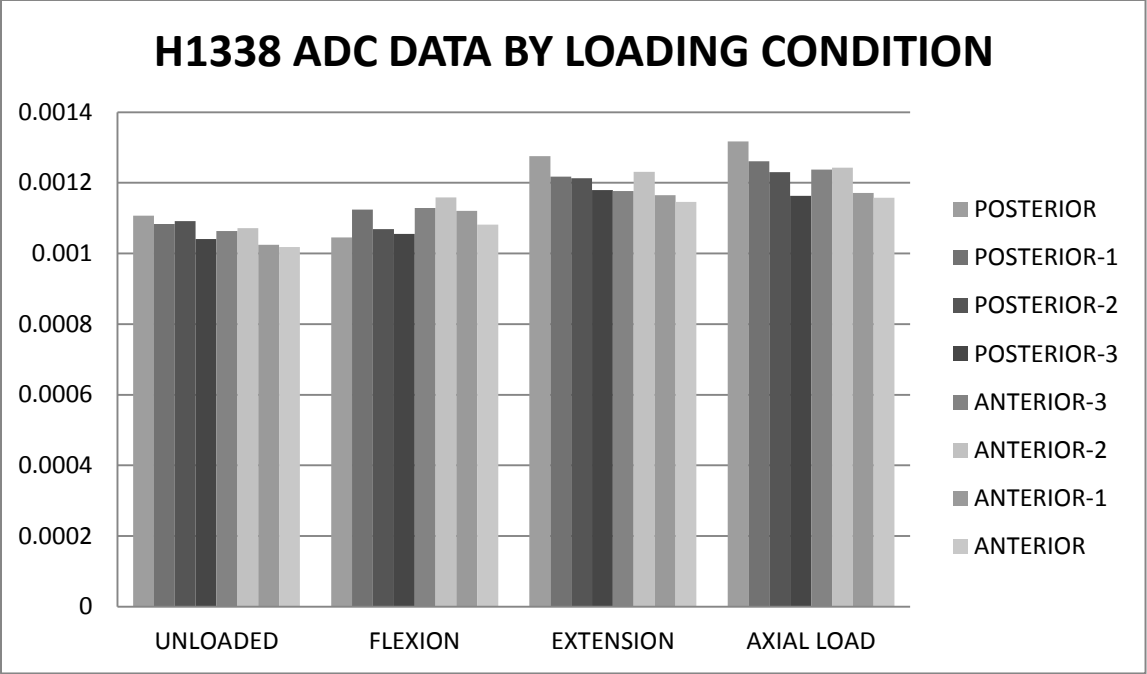
Specimen	Flexion angle (°)	Extension angle (°)
H1144	+9.1	-6.5
H1338	+10.0	-5.7
H1327	+14.36	-5.8

### E.2 Alternative data representation for ADC measurements of postural loading











## Appendix F Tissue loading device specification

### F.1 Main apparatus specification

#### 1. Material specification: PLA



HATCHBOX 3D PLA-1KG1.75-BLK PLA 3D Printer Filament, Dimensional Accuracy +/- 0.05 mm, 1 kg Spool, 1.75 mm, Black

by HATCHBOX

★★★★★ 83 customer reviews

Price: **CDN\$ 56.68 & FREE Shipping**. Details

6 new from **CDN\$ 56.68** 1 used from **CDN\$ 44.98**

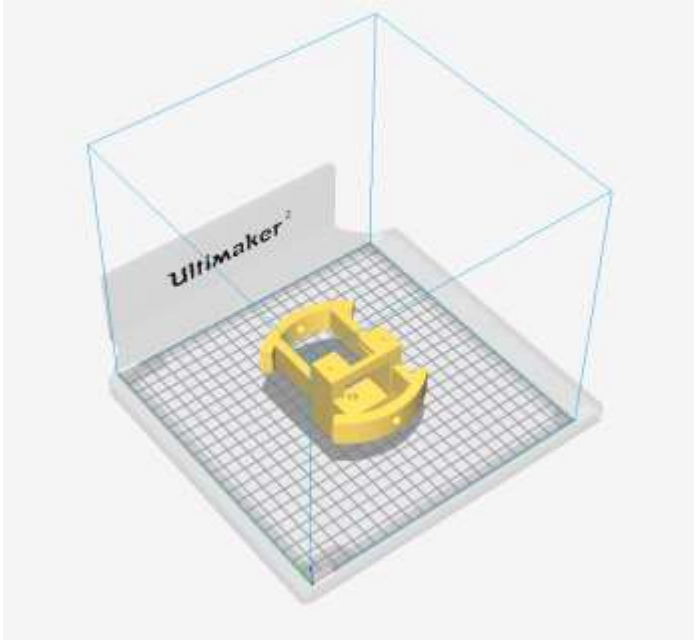
- 1 KG (approximately 2.20 lbs) Spool
- 1.75mm Filament Diameter (Dimensional Accuracy +/- 0.05mm)
- PLA (Polylactic Acid) 3D Printer Filament Vacuum Sealed With Desiccant
- Recommended Extrusion/Nozzle Temperature 180°C - 210°C (356°F - 410°F)
- Spool Diameter: 7.88" - Spool Width: 2.65" - Spool Hub Hole Diameter: 2.20"

#### 2. Printer Specification

##### SPECIFICATIONS

Printing	
Print technology	Fused Filament Fabrication
Build volume	223 mm / 223 mm / 205 mm
Layer resolution	Fast: 200 micron (0.2 mm)
	Normal: 100 micron (0.1 mm)
	High: 60 micron (0.06 mm)
	Ulti: 40 micron (0.04 mm)
	12.5 micron / 12.5 micron / 5 micron
Positioning precision	12.5 micron / 12.5 micron / 5 micron
Filament diameter	2.85 mm
Nozzle diameter	0.4 mm
Print speed	30 mm/s - 300 mm/s
Travel speed	30 mm/s - 350 mm/s
Software	
Supplied software	Cura - Official Ultimaker Software
File types	STL / OBJ / DAE / AMF
Supported OS	Windows / Mac / Linux
Electrical	
AC Input	100 - 240 V
	Approx. 1.4 AMPS
	50 - 60 Hz
	221 Watt max.
Connectivity	Stand-alone SD card printing
Physical dimensions	
Desktop space	357 mm / 342 mm / 388 mm
Shipping dimensions	400 mm / 400 mm / 550 mm
Weight	11.2 kg
Shipping weight	18.0 kg
Temperature	
Ambient operation temperature	15 - 32 °C
Storage temperature	0 - 32 °C
Nozzle operation temperature	180 - 260 °C
Heated bed operation temperature	50 - 100 °C
Sound	
Average operational noise	49 dBA

#### 3. Orientation in the machine



4. Support parameters
  - For holes and syringe flange slot only.
  - Standard supports generated from Cura (Version 3.5.0)
5. Machine build parameters or acceptable ranges
  - Layer height: 0.6
  - Print speed: slow
  - Infill: 20 %
6. Support removal requirements
  - remove all supports by carefully breaking away from true surfaces of the device
  - use a file to remove supports from more areas prone to warping, such as the slot for the 10 cc syringe flange
7. Surface finish
  - Not required; modify as desired
8. Painting/coating
  - Not required; modify as desired
9. Features that require secondary machining
  - tapped holes: 1x M8x1.25 mm on back face of main body; 2x 3/8"-16

## Nylon Socket Head Screw

M8 x 1.25 mm Thread, 35 mm Long



Packs of 10

In stock  
\$10.14 per pack of 10  
93640A123

**ADD TO ORDER**

Thread Size	M8
Thread Pitch	1.25 mm
Length	35 mm
Threading	Fully Threaded
Head Diameter	13 mm
Head Height	8 mm
Drive Size	6 mm
Material	Nylon Plastic
Hardness	Not Rated
Tensile Strength	Not Rated
Thread Type	Metric
Thread Spacing	Coarse
Thread Fit	Not Rated
Thread Direction	Right Hand
Head Type	Socket
Socket Head Profile	Standard

## Nylon Plastic Flat-Tip Set Screws

3/8"-16 Thread, 1/2" Long



Packs of 50

In stock  
\$12.68 per pack of 50  
94564A405

**ADD TO ORDER**

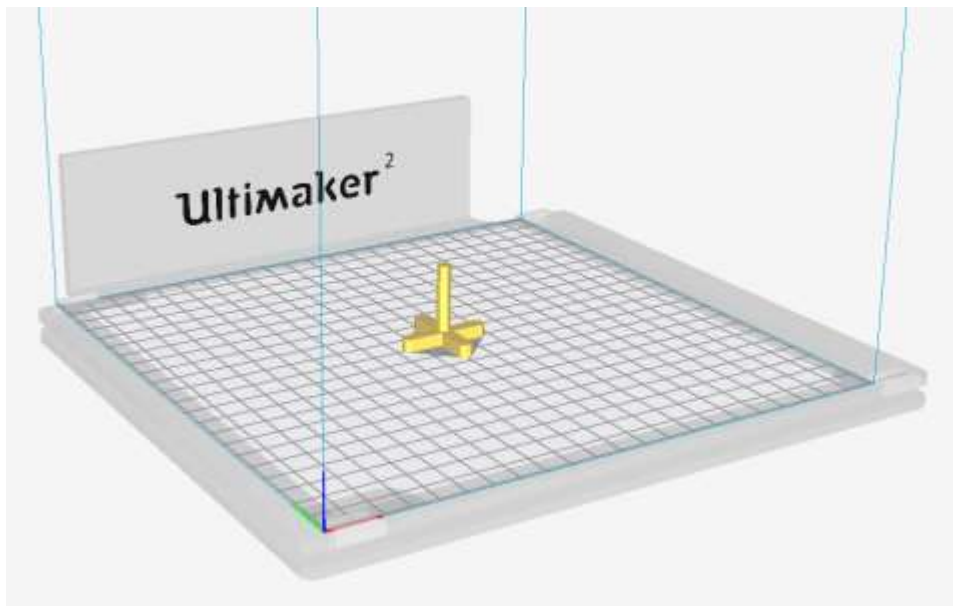
Material	Nylon Plastic
Thread Size	3/8"-16
Length	1/2"
Drive Size	3/16"
Screw Size Decimal Equivalent	0.375"
Temperature Range	-40° to 185° F
Color	Off-White
Hardness	Not Rated
Thread Type	UNC
Thread Spacing	Coarse
Thread Fit	Class 2A
Thread Direction	Right Hand
Drive Style	Hex
Tip Type	Flat
Head Type	Headless

## F.2 Allen key specification

- Hex width
  - Across flats: 0.185"
  - Across corners: 0.215"
- Stem length: 26 mm
- Handle width: 35 mm
- Handle thickness: 5 mm



Required print direction



## Appendix G Repeatability Data for ADC

A test was conducted to establish the repeatability of the ADC measurements for a given tissue sample. For this experiment, four diffusion-weighted imaging sequences (as outlined in *Section 4.2 – Image acquisition*) were executed. Segmentation was performed on each sample separately, following the procedures in *Section 4.2 – image processing*. The Resulting ADC data is shown below, with strong repeatability. Error bars represent the standard deviation of the distribution of ADC values within the voxels of the segmented region.

